sid.inpe.br/mtc-m21c/2020/10.27.17.28-TDI

ON THE REPRESENTATION OF WARM-PHASE MICROPHYSICAL PROCESSES IN NUMERICAL SIMULATIONS OF CUMULUS CLOUDS

Lianet Hernández Pardo

Doctorate Thesis of the Graduate Course in Meteorology, guided by Dr. Luiz Augusto Toledo Machado, approved in November 19, 2020.

URL of the original document:
<http://urlib.net/8JMKD3MGP3W34R/43FSLES>

INPE
São José dos Campos
2020

PUBLISHED BY:

Instituto Nacional de Pesquisas Espaciais - INPE
Gabinete do Diretor (GBDIR)
Serviço de Informação e Documentação (SESID)
CEP 12.227-010
São José dos Campos - SP - Brasil
Tel.:(012) 3208-6923/7348
E-mail: pubtc@inpe.br

sid.inpe.br/mtc-m21c/2020/10.27.17.28-TDI

ON THE REPRESENTATION OF WARM-PHASE MICROPHYSICAL PROCESSES IN NUMERICAL SIMULATIONS OF CUMULUS CLOUDS

Lianet Hernández Pardo

Doctorate Thesis of the Graduate Course in Meteorology, guided by Dr. Luiz Augusto Toledo Machado, approved in November 19, 2020.

URL of the original document:
<http://urlib.net/8JMKD3MGP3W34R/43FSLES>

INPE
São José dos Campos
2020

Cataloging in Publication Data

Hernández Pardo, Lianet.

He43r On the representation of warm-phase microphysical processes in numerical simulations of cumulus clouds / Lianet Hernández Pardo. – São José dos Campos : INPE, 2020.

xxvi + 137 p. ; (sid.inpe.br/mtc-m21c/2020/10.27.17.28-TDI)

Thesis (Doctorate in Meteorology) – Instituto Nacional de Pesquisas Espaciais, São José dos Campos, 2020.

Guiding : Dr. Luiz Augusto Toledo Machado.

1. Cloud microphysical processes. 2. Microphysics parameterizations. 3. Convective clouds. 4. .Aerosol-cloud-precipitation interactions. 5. Droplet size distributions. I.Title.

CDU 551.576

MINISTÉRIO DA CIÊNCIA, TECNOLOGIA E INOVAÇÕES

INSTITUTO NACIONAL DE PESQUISAS ESPACIAIS

Serviço de Pós-Graduação - SEPGR

Pós Graduação em Meteorologia

ATA DE REUNIÃO

DEFESA FINAL DE TESE (Lianet Hernández Pardo)

No dia 19 de novembro de 2020, as 13h, por videoconferência, a aluna mencionada acima defendeu seu trabalho final, intitulado "On the representation of warm-phase microphysical processes in numerical simulations of cumulus clouds" (apresentação oral seguida de arguição) perante uma Banca Examinadora, cujos membros estão listados abaixo. A aluna foi **APROVADA** pela Banca Examinadora, por unanimidade, em cumprimento ao requisito exigido para obtenção do Título de Doutor em Meteorologia.

Eu, Luiz Fernando Sapucci, como Presidente da Banca Examinadora, assino esta ATA em nome de todos os membros.

Membros da Banca

Dr. Luiz Fernando Sapucci – Presidente - INPE

Dr. Luiz Augusto Toledo Machado - Orientador(a) - INPE

Dr. Éder Paulo Vendrasco - Membro interno - INPE

Dr. Hugh Morrison - Convidado(a) - UCAR - USA

Dra. Mira Pöhlker - Convidado(a) -MPIC - Alemanha

Att, Luiz Sapucci

Documento assinado eletronicamente por **Luiz Fernando Sapucci**, **Pesquisador**, em 30/11/2020, às 11:02 (horário oficial de Brasília), com fundamento no art. 6º, § 1º, do Decreto nº 8.539, de 8 de outubro de 2015.

A autenticidade deste documento pode ser conferida no site http://sei.mctic.gov.br/verifica.html, informando o código verificador **6140841** e o código CRC **D1FB9F06**.

Referência: Processo nº 01340.008210/2020-18 SEI nº 6140841

A mis padres, ***Isel*** *y* ***Armando***

ACKNOWLEDGEMENTS

I would like to thank the São Paulo Research Foundation (FAPESP, grants 2014/14497-0., 2016/24562-6 and 2019/06988-4) and the Coordination for the Improvement of Higher Education Personnel (CAPES) for the support and funding that allowed the execution of this research work.

I would also like to thank the National Institute for Space Research (INPE) and its Meteorology Graduate Program for hosting my PhD studies. I appreciate the support I received from the National Center for Atmospheric Research (NCAR) before and during my research visit.

I am extremely grateful to my supervisor Dr. Luiz Augusto Toledo Machado for all the help, advice and encouragement during this PhD.

I truly appreciate all the guidance, collaboration and feedback of Dr. Hugh Morrison, who supervised my research visit at NCAR.

I thank the ACRIDICON-CHUVA team for their effort to produce the observational data employed in this research.

I would like to express gratitude to Dr. Micael Amore Cecchini, Dr. Madeleine Sánchez Gácita, Dr. Thiago Souza Biscaro, Dr. Jean-François Ribaud, Dr. Eder Vendrasco, Dr. Zachary J. Lebo and Dr. Jerry Y. Harrington for the scientific collaboration.

I greatly appreciate the comments made by Dr. Henrique Barbosa on an earlier version of this thesis.

For my partner Tiago, thanks for all your love, good humor and empathy.

Many thanks to my family for unconditionally having my back.

ABSTRACT

This research analyzes the role of microphysical processes in the evolution of convective clouds, with emphasis on their representation in atmospheric models, taking advantage of in-situ measurements obtained as part of the ACRIDICON-CHUVA field campaign near the Amazon basin. Firstly, cloud sensitivities to changes in aerosol properties, such as total number concentration (N_a), size distribution and composition, are explored. This analysis focuses on the droplet number concentration and effective diameter at the top of a shallow cumulus simulated with a bin-microphysics single-column model, for initial conditions typical of the Amazonian region. The impact of considering bin versus bulk aerosol size distributions is evaluated, in order to investigate the influence of entrainment and activation scavenging on the derived sensitivities. It is shown that the evolution of cloud-top droplet size distributions (DSDs) is generally very sensitive to changes in aerosol parameters, but the sign and absolute value of this sensitivity depends on the position within the multidimensional aerosol parameter space considered, as well as on the treatment of entrainment and aerosol scavenging. Following, idealized two- and three-dimensional Weather Research and Forecasting model simulations of an isolated warm cumulus cloud were performed to assess the role of DSD broadening mechanisms in bin microphysics parameterizations. As expected, collision-coalescence is a key process broadening the modeled DSDs. In-cloud droplet activation also contributes substantially to DSD broadening, whereas evaporation has only a minor effect and sedimentation has little effect. Cloud dilution (mixing of cloud-free and cloudy air) also broadens the DSDs considerably, whether or not it is accompanied by evaporation. Artificial broadening from vertical numerical diffusion appears to be relatively unimportant overall for these cumulus simulations. Finally, the spatial distribution of DSD relative dispersion (ϵ) within observed and modeled convective clouds is analyzed, taking into account changes in N_a. The spatial distribution of DSD shape in aircraft measurements of growing cumuli near the Amazon basin shows distinctive patterns depending on the aerosol loading. In cleaner clouds ($N_a < 900$ cm^{-3}), ϵ varies between ~ 0.1 and ~ 0.6, overall being inversely related to the ratio of the cloud water content (q_c) and the adiabatic water content (q_a). In polluted clouds ($N_a > 2000$ cm^{-3}), ϵ generally has values in the range $0.25 - 0.45$, with no evident dependence on either height above cloud base or q_c/q_a. Bin-microphysics numerical simulations confirm that these contrasting behaviors are associated with the predominance of collision-coalescence in cleaner clouds, and in-cloud droplet activation in polluted ones. These findings can be useful for parameterizations of the shape parameter (μ) of droplet gamma size distributions in bulk-microphysics cloud-resolving models. It is shown that emulating the observed $\mu - q_c/q_a$ relationship improves the estimation of the collision-coalescence rate in bulk microphysics simulations.

Keywords: cloud microphysical processes. microphysics parameterizations. convective clouds. aerosol-cloud-precipitation interactions. droplet size distributions.

ANÁLISE DA REPRESENTAÇÃO DOS PROCESSOS DE MICROFÍSICA DE NUVENS CORRESPONDENTES À FASE QUENTE EM SIMULAÇÕES NUMÉRICAS DE NUVENS CUMULUS

RESUMO

Esta pesquisa analisa o papel dos processos de microfísica na evolução das nuvens convectivas, com ênfase na sua representação em modelos atmosféricos, usando observações do experimento ACRIDICON-CHUVA na Amazônia. Em primeiro lugar, é explorada a sensibilidade das nuvens a mudanças nas propriedades dos aerossóis, como concentração (N_a), distribuição de tamanho e composição. Esta análise está focada na concentração total e o diâmetro efetivo das gotículas no topo de cumulus rasos simulados com um modelo 1D usando um esquema de microfísica *bin*, para condições iniciais tipicas da Amazônia. É avaliado o impacto de considerar enfoques *bin* ou *bulk* para as distribuições de tamanho dos aerossóis, com o objetivo de investigar a influência do entranhamento e a ativação nas sensibilidades obtidas. Mostra-se que a evolução da distribuição de tamanho de gotas (DSD) é geralmente muito sensível a mudanças nos parâmetros dos aerossóis, mas o sinal e o valor absoluto da sensibilidade depende da posição considerada no espaço multidimensional dos parâmetros dos aerossóis, assim como do tratamento do entranhamento e do remoção de aerossóis por ativação. Seguidamente, são utilizadas simulações idealizadas de cumulus rasos em 2D e 3D com o modelo *Weather Research and Forecasting* para estudar o papel dos processos que intervem no alargamento das DSDs em parametrizações de microfísica *bin*. Como esperado, a colisão-coalescência é um processo chave no alargamento das DSDs no modelo. A ativação de gotas no interior das nuvens também contribui significativamente para o alargamento das DSDs, enquanto a evaporação tem um efeito menor e a influência da sedimentação é negligenciável. A diluição da nuvem (mistura com o ar na vizinhança) também alarga as DSDs consideravelmente, independentemente da ocorrência de evaporação. O alargamento artificial das DSDs devido à difusão numérica na direção vertical tem relativamente pouca importância em geral nessas simulações. Finalmente, analisa-se a distribuição espacial da dispersão relativa das DSDs (ϵ) em nuvens convectivas observadas e simuladas, levando em conta mudanças em N_a. A distribuição espacial da forma das DSDs em medições diretas de cumulus em crescimento na Amazônia contém padrões distintivos dependendo do conteúdo de aerossóis. Em nuvens limpas ($N_a < 900$ cm^{-3}), ϵ varia entre ~ 0.1 e ~ 0.6, dependendo principalmente razão entre o conteúdo de água de nuvem (q_c) e conteúdo de água líquida adiabático (q_a). Em nuvens poluídas ($N_a > 2000$ cm^{-3}), ϵ generalmente toma valores no intervalo $0.25 - 0.45$, e é praticamente independente da altura acima da base na nuvem e de q_c/q_a. Simulações com o esquema de microfísica *bin* confirmam que estes comportamentos contrastantes estão associados à predominância de colisão-coalescência em nuvens limpas, e ativação de gotas no interior de nuvens poluídas. Estes resultados podem ser úteis para parametrizar o parâmetro de forma (μ) de distribuições gama de tamanho de gotas em esquemas de microfísica do tipo *bulk* em modelos de nuvem resolvida. É mostrado que a inclusão da relação $\mu - q_c/q_a$ de acordo com as observações melhora a estimativa da colisão-coalescência em simulações de microfísica *bulk*.

Palavras-chave: processos de microfísica de nuvens. parametrizações de microfísica de nuvens. nuvens convectivas. interações aerossóis-nuvens-precipitação. distribuição de tamanho de gotas.

LIST OF FIGURES

Page

LIST OF TABLES

LIST OF ABBREVIATIONS

2D	–	Two dimensions
3D	–	Three dimensions
CCN	–	Cloud Condensation Nuclei
GCCN	–	Giant Cloud Condensation Nuclei
DSD	–	Droplet Size Distribution
PSD	–	Aersol Particle Size Distribution
ACRIDICON-CHUVA	–	Field campaign "Aerosol, Cloud, Precipitation, and Radiation Interactions and Dynamics of Convective Cloud Systems–Cloud Processes of the Main Precipitation Systems in Brazil: A Contribution to Cloud-Resolving Modeling and to the Global Precipitation Measurement"
CCP	–	Cloud Combination Probe
CDP	–	Cloud Droplet Probe
CIPg	–	Cloud Imaging Probe
LES	–	Large-Eddy Simulation
WRF	–	Weather and Research Forecasting model
TAU	–	Tel Aviv University size-bin-resolved microphysics scheme
M09	–	Two-moment bulk microphysics scheme of Morrison et al. (2009)
RMSE	–	Root-Mean-Square Error
CCrate	–	Total number concentration of droplets collected per
	–	second
CCrate_c	–	Total number concentration of droplets smaller than 50 μm collected per second
ACTrate	–	Ratio of the number concentration of droplets activated per second to the initial aerosol number concentration
CONDrate	–	Rate of change of the mean droplet size due to diffusion of water vapor to/from cloud droplets

LIST OF SYMBOLS

t	–	time
z	–	altitude
h	–	height above cloud base
w	–	vertical velocity
θ	–	potential temperature
θ_e	–	equivalent potential temperature
ρ_w	–	density of liquid water
q_v	–	water vapor mixing ratio
q_l	–	liquid water mixing ratio
q_a	–	adiabatic liquid water content (mass concentration)
R	–	radius of the convective plume
r	–	aerosol radius
N_a	–	aerosol total number concentration
$\bar{r}_a$	–	median radius of the aerosol log-normal size distribution
σ_a	–	aerosol geometric standard deviation
κ	–	aerosol hygroscopicity parameter
r_c	–	aerosol critical radius for activation
D	–	droplet diameter
q_c	–	cloud droplet water content (mass concentration)
N_c	–	total number concentration of cloud droplets
N_d	–	total number mixing ratio of cloud droplets
$N(D)$	–	number concentration of droplets with diameter D
D_{eff}	–	droplet effective diameter
D_m	–	mean diameter of the droplet size distribution
σ	–	standard deviation of the droplet size distribution
ϵ	–	relative dispersion of the droplet size distribution
μ	–	shape parameter of gamma size distributions for cloud droplets
ΔD_{99}	–	difference between the diameters of the 99^{th} and 50^{th} percentiles of the droplet size distribution
$\bar{N}_c$	–	time average of N_c at cloud-top
$\bar{D}_{eff}$	–	time average of D_{eff} at cloud-top
$S_Y(X_i)$	–	relative change in Y for a relative change in X_i
μ_4	–	linear function that relates μ and q_c/q_a considering differences in N_a, fitted from observations

CONTENTS

1 INTRODUCTION

Accurate numerical weather predictions require a representation of sub-grid physical processes in terms of the model resolved variables, i.e., physical parameterizations. Without parameterizations of the main sub-grid scale processes, simulations become unrealistic "from a day or two for large-scale flow, to less than an hour for storm-scale simulations" (KALNAY, 2002). Today's increasing availability of computing power allows to obtain high resolution numerical forecasts that are able to resolve convection explicitly. In these models, it is essential to parameterize cloud microphysical processes, i.e., water phase transitions, interactions among hidrometeors and their sedimentation. Microphysical processes driving the formation and evolution of clouds and precipitation determine vertical exchanges of energy and mass in the troposphere and the lower stratosphere, and have a large impact on the global radiative balance.

The realism of cloud microphysics parameterizations have been improved over the last decades, with current schemes covering a wide spectrum of complexities (KHAIN et al., 2004; GILMORE et al., 2004; KHAIN et al., 2010; MANSELL et al., 2010; LIM; HONG, 2010; LOFTUS et al., 2014; THOMPSON; EIDHAMMER, 2014). Bin and Lagrangian microphysics approaches are considered to be more accurate and flexible (BERRY; REINHARDT, 1974; ENUKASHVILY, 1980; TZIVION et al., 1987; SHIMA et al., 2009; GRABOWSKI et al., 2018; SEIFERT et al., 2019), but their computational cost is usually too high for operational applications or large scale simulations. In such cases, bulk schemes (LIN et al., 1983; FERRIER, 1994; THOMPSON et al., 2008; MORRISON et al., 2009) are employed. While Bin and Lagrangian approaches predict the evolution of hydrometeor size distributions, bulk microphysics parameterizations compute conversion rates among several hydrometeor categories in terms of integral properties of their size distributions (typically, mass and number). Consequently, hydrometeors size distributions are usually assumed to follow predefined functional relationships, such as the gamma function:

$$N(D) = N_0 D^{\mu} e^{-\Lambda D} \tag{1.1}$$

where N_0, μ and Λ are the intercept, shape and slope parameters, respectively, and $N(D)$ is the number of droplets in a diameter interval $D + dD$ in a unit volume of air. The assumption of a predefined function for hydrometeor size distributions constitutes an intrinsic limitation of most bulk microphysics parameterizations. Local droplet size distributions (DSDs) can present specific features, such as

bi-modalities, that significantly deviate from the average gamma-like shape (KHAIN et al., 2015). Moreover, bulk schemes must predict at least three moments to evolve the three gamma-size-distribution's parameters independently, and schemes predicting fewer moments must introduce additional closure assumptions. In the case of double-moment schemes that assume gamma size distributions, empirical methods are generally employed in order to determine the shape parameter μ.

Bin (size-resolved) microphysics is often used as a benchmark for evaluating and improving bulk microphysics schemes. However, bin schemes suffer from critical limitations, especially related to their numerical implementation in Eulerian dynamical models. A key issue is artificial DSD broadening during condensational growth/evaporation that occurs because of numerical diffusion in physical space, even using accurate, state-of-the-art methods for condensational growth. These errors lead to considerable uncertainty in the ability of bin schemes in Eulerian dynamical models to realistically simulate DSD evolution and precipitation generation in warm clouds (MORRISON et al., 2018), therefore hindering the ability to explore the real (physical) causes for DSD widening.

Besides numerical limitations, all microphysics parameterizations involve large uncertainties related to unknowns in the description of particle-level physical processes. Many gaps remain in the description of ice and mixed-phase processes, associated with the complex structure of ice particles and the variety of particle shapes and densities (KHAIN; PINSKY, 2018). Nonetheless, several aspects of warm-clouds, such as the mechanisms responsible for the formation of rain drops, also remain an open questions for the cloud physics community. Adiabatic diffusional growth of droplets in non-turbulent air leads to narrowing of DSDs, which inhibits collision-coalescence (PRUPPACHER; KLETT, 2012). In contrast, observed DSDs are often much wider than DSDs obtained from adiabatic calculations of condensational growth above cloud base (JENSEN et al., 1985). For decades, many explanations have been proposed for bridging this gap between the classical effects of the diffusional and collision-coalescence growth processes, but this controversial topic continues to be the focus of many modeling and observational studies.

A crucial aspect in cloud simulations is the treatment of the aerosols. Because of their role as cloud condensation nuclei (CCN) and ice nucleating particles, aerosols can affect cloud optical properties, determine the onset of precipitation and ice formation, and also impact the thermodynamics of the clouds (TWOMEY, 1974; ALBRECHT, 1989; ANDREAE et al., 2004; KHAIN et al., 2005; FAN et al., 2007; LEE et

al., 2008; ROSENFELD et al., 2008; KOREN et al., 2010; LI et al., 2011; GONÇALVES et al., 2015; HEIBLUM et al., 2016; BRAGA et al., 2017). However, these effects can be offset by microphysics and macrophysics interactions, determining a cloud-regime dependency for the net impact of aerosols (STEVENS; FEINGOLD, 2009). Deficiencies in the representation of clouds in models preclude the obtention of reliable assessments of the effects of aerosols on Earth's radiative budget (SEINFELD et al., 2016). Despite decades of research, global estimations of changes in Earth's radiative forcing, induced by changes in clouds' properties as a consequence of increasing aerosol anthropogenic emissions, are highly uncertain (BOUCHER et al., 2013).

With ample water vapor supply, high temperatures and a wide spectrum of aerosol conditions, the troposphere over the Amazon constitutes an ideal natural scenario to study aerosol-cloud-precipitation interactions. The characteristics of clouds forming in the Amazon are well correlated with changes in aerosol loading (REID et al., 1999; ANDREAE et al., 2004; CECCHINI et al., 2016; BRAGA et al., 2017; CECCHINI et al., 2017). Moreover, recent experimental campaigns in the Amazon have revealed that clouds control both the removal and production of atmospheric particles, adding an extra layer of complexity in the study of aerosol-cloud interactions. According to Andreae et al. (2018), the production of new aerosol particles from biogenic volatile organic compounds brought up by deep convection to the upper troposphere, is the dominant process supplying secondary aerosol particles in pristine conditions over the Amazon. Those particles can be transported from the free troposphere into the boundary layer by strong convective downdrafts or even weaker downward motions in the trailing stratiform region of convective systems (WANG et al., 2016). During the transition or dry seasons, frequent biomass burning events change the aerosol population characteristics as a whole, along with the aerosol number concentration (N_a) (ANDREAE et al., 2004; PÖHLKER et al., 2016; PÖHLKER et al., 2018).

This research focuses on the role of warm microphysical processes in the evolution of convective clouds, with emphasis on their representation in atmospheric models, taking advantage of in-situ measurements obtained as part of the field campaign "Aerosol, Cloud, Precipitation, and Radiation Interactions and Dynamics of Convective Cloud Systems–Cloud Processes of the Main Precipitation Systems in Brazil: A Contribution to Cloud-Resolving Modeling and to the Global Precipitation Measurement" (ACRIDICON-CHUVA) near the Amazon basin. Firstly, DSD sensitivities to changes in aerosol properties at cloud top were explored, using single-column bin-microphysics simulations of a warm cloud. The impact of considering bin versus bulk approaches for the aerosols was evaluated, in order to investigate the influence of

entrainment and activation, as source and sink of aerosols particles, respectively, on the derived sensitivities. Next, idealized two-dimensional (2D) and three-dimensional (3D) simulations of an isolated warm cumulus cloud were performed to assess the role of DSD broadening mechanisms in Eulerian bin-microphysics simulations (here by "Eulerian", we mean using an Eulerian grid discretization both in physical space and mass spectrum space for the microphysical variables). This way, the contributions of various processes to DSD broadening and evolution were identified, including evaporation, in-cloud droplet activation, collision-coalescence, turbulent mixing, and cloud dilution from entrainment and mixing with cloud-free air. The effects of artificial DSD broadening from the combination of condensational growth and vertical numerical diffusion, as described by Morrison et al. (2018), were also examined. Finally, the spatial distribution of DSD width within observed and modeled convective clouds was analyzed, taking into account changes in N_a. Based on this study, the potential of different diagnostic relationships for representing the variability of droplet spectral dispersion in bulk microphysics parameterizations was investigated.

Chapter 2 contains a brief literature review about the main subjects investigated here: quantification of cloud sensitivity to aerosol properties, droplet size distribution broadening mechanisms, and treatment of the shape parameter of droplet size distributions in bulk microphysics parameterizations. Chapter 3 presents the model and observations employed for this research. Results are described in Chapters 4, 5 and 6, and the general conclusions are outlined in Chapter 7.

1.1 Objectives

The main goal of this research is to improve the existing knowledge on the performance of microphysics parameterizations for representing warm-phase cloud processes, including aerosol-cloud interactions, in convective clouds.

The specific objectives of this study are:

i) to characterize the sensitivity of cloud-top DSDs to changes in the aerosol size distribution and hygroscopicity in single-column simulations with bin microphysics,

ii) to evaluate the impact of considering temporal and spatial variations in the aerosol size distribution, due to entrainment and activation, on the sensitivity of modeled DSDs to changing aerosol properties,

iii) to identify the role of physical mechanisms leading to DSD broadening

in cumulus clouds simulated with 2D and 3D bin-microphysics Eulerian models,

iv) to investigate how grid spacing impacts spurious DSD broadening by comparing DSD evolution using different horizontal and vertical grid spacings using 2D bin microphysics simulations,

v) to determine the main factors affecting the spatial variability of DSD width within observed and simulated cumulus clouds, and

vi) to assess potential diagnostic relationships that improve the representation of the shape parameter of gamma DSDs in bulk microphysics models.

2 LITERATURE REVIEW

In this chapter, results from previous studies relevant for pursuing the objectives stated in Section 1.1 are summarized. Other references motivating individual studies are specified in chapters 4, 5 and 6, respectively.

2.1 Current challenges in the study of DSD sensitivity to aerosol properties

Many studies have been dedicated to quantifying the effect of aerosols on cloud DSDs through sensitivity calculations, using both modeling and observational approaches. The use of remote sensing facilitates global assessments of aerosol-cloud interactions, but results can be subject to errors in retrievals of aerosol and cloud properties, including errors related to miss-identification of cloud areas (TANRé et al., 1997; MARTINS et al., 2002; YANG; GIROLAMO, 2008; JEONG; LI, 2010; WEI et al., 2020).

In general, determining causality from correlations between aerosols and clouds is not straightforward (STEVENS; FEINGOLD, 2009). While cloud properties are affected by the aerosols, the latter is also modified by cloud and precipitation processes (CLARKE et al., 1999; PETTERS et al., 2006; ANDREAE et al., 2018). Moreover, meteorological (large-scale flow) and thermodynamical factors can determine simultaneous changes in the fields of both cloud and aerosol particles (MATSUI et al., 2006; ANDERSON et al., 2009; PAINEMAL; ZUIDEMA, 2010). For instance, Mauger and Norris (2007) found that correlations between both aerosols and cloud fraction with the static stability of the air mass during the previous days explained most of the observed aerosol-cloud correlations in the subtropical northeast Atlantic. Similarly, Engström and Ekman (2010) found significant correlations between the 10-meter wind speed and both aerosol optical depth and cloud fraction in semi-global multiyear satellite observations. They showed that controlling for variations in wind reduced the correlation between aerosol optical depth and cloud fraction, especially when marine stratocumulus prevailed.

Detailed modeling of droplet nucleation implies a high computational cost and knowing the true value of all the parameters that characterize the aerosol population is difficult, if not impossible. Thus, sensitivity studies intend to determine whether the variability of some properties of the aerosol population can be neglected without introducing significant errors in the description of clouds.

A major debate refers to the relative importance of N_a and the aerosol size distribu-

tion against composition (MCFIGGANS et al., 2006). Several studies suggested that accurate measures of aerosol size and number concentration are more important to obtain a relatively accurate description of cloud droplet populations (FEINGOLD, 2003; DUSEK et al., 2006; ERVENS et al., 2007; GUNTHE et al., 2009; ROSE et al., 2010; REUTTER et al., 2009). However, other observations/simulations showed that, under certain circumstances, neglecting the variability of the aerosol composition prevent realistic estimations of the aerosol effect on clouds (HUDSON, 2007; QUINN et al., 2008; CUBISON et al., 2008; ROESLER; PENNER, 2010; CHEN et al., 2016; GÁCITA et al., 2017). For instance, Karydis et al. (2012) found that the cloud droplet number concentration (N_c) is generally less sensitive to changes in the hygroscopicity parameter than in N_a, but there are regions and times where their impact have comparable magnitudes, especially for Artic and remote oceanic areas. This circumstantial sensitivity is commonly found in the literature, associated with the buffering effect of microphysical and macrophysical processes (STEVENS; FEINGOLD, 2009).

Feingold (2003) showed that the influence of aerosol parameters on the droplet effective radius varies as a function of aerosol loading: under clean conditions, the droplet effective radius is mostly determined by the liquid water content and N_a, with decreasing dependence on the aerosol size distribution (PSD), aerosol composition and vertical velocity (w); however, under polluted conditions, all of these factors contribute significantly to changes in the droplet effective radius. Reutter et al. (2009) argued that the variability of N_c in convective clouds is mostly driven by the variability of w and N_a, with two well defined (aerosol-limited and updraft-limited) regimes. They found that the role of the hygroscopicity parameter is important only at very low supersaturations in the updraft-limited regime. In turn, Ward et al. (2010) examined the sensitivity of cloud DSDs to the hygroscopicity parameter for several values of the log-normal median aerosol radius ($\bar{r}_a$) under conditions typical of the aerosol-limited and updraft-limited regimes. They showed that the ratio w/N_a, or supersaturation-based regimes, cannot fully predict the dependence of CCN activity on chemical composition, since it also depends on $\bar{r}_a$, especially for $\bar{r}_a < 0.06$ μm.

While adiabatic parcel models can capture the response of cloud-base DSDs to aerosols through droplet nucleation and activation, it precludes analyses of DSDs' responses higher in the clouds, where complex multi-scale interactions may play a more important role (FLOSSMANN; WOBROCK, 2010). On the other hand, representing 3D realistic clouds often comes at a price of neglecting details in the representation of microphysical processes and/or testing a much lower number of

settings, compared to parcel models (PENNER et al., 2006). Chapter 4 presents an investigation of the aerosol-cloud interaction using a column model, where the relevance of considering the entrainment in calculations of cloud sensitivity to aerosols is explored.

2.2 DSD broadening mechanisms

Many modeling and observational studies have intended to bridge the gap between the classical effects of the diffusional and collision-coalescence growth processes (PRUPPACHER; KLETT, 2012). These mechanisms usually center on physical processes that broaden DSDs relative to what would occur from only diffusional growth (we refer to this as DSD "broadening" here).

Despite being typically neglected in the calculation of droplet growth by condensation in models, the solute and curvature effects can induce Ostwald ripening processes, which are a potential source of DSD broadening through irreversible condensation/evaporation events, amplified by activation/deactivation in vertically oscillating motions (KOROLEV, 1995; YANG et al., 2018). Jensen and Nugent (2017) showed that relatively undilute droplets formed on giant cloud condensation nuclei (GCCN) can grow fast through water vapor condensation, even in cloud downdrafts. Thus, cloud drops nucleated on GCCN enhance the development of a tail in the DSD that significantly accelerates collision-coalescence processes, especially in continental clouds with high concentrations of small aerosols (YIN et al., 2000b). Specifically at cloud top, including the long wave radiative cooling in the condensation calculations can also lead to significant DSD broadening in simulated stratocumulus, as discussed by Hartman and Harrington (2005a), Hartman and Harrington (2005b) and Lebo et al. (2008).

Furthermore, several broadening mechanisms can be attributed to the effects of turbulence in clouds (DEVENISH et al., 2012; GRABOWSKI; WANG, 2013). For instance, larger-scale inhomogeneities of N_c and supersaturation can be produced by turbulent fluctuations (BAKER et al., 1984; GRABOWSKI; ABADE, 2017; DODSON; GRISWOLD, 2019). Subsequent mixing of droplets that have experienced different trajectories, and, therefore, different condensational growth histories in the clouds, has been considered as a key process generating broadening of DSDs in natural clouds (COOPER, 1989; LASHER-TRAPP et al., 2005; GRABOWSKI; ABADE, 2017; ABADE et al., 2018); this has been referred to as "eddy hopping" (GRABOWSKI; ABADE, 2017). Small eddies are important for this mechanisms, since they act to transfer droplets between the larger eddies inside clouds. It has been argued that local perturbations in the

supersaturation field, caused by the inertial droplet clustering associated with small-scale eddies, modulate the rate of in-cloud activation and droplet growth by vapor diffusion, thus contributing to DSD broadening (SHAW et al., 1998; GRABOWSKI; VAILLANCOURT, 1999; KOSTINSKI; SHAW, 2001). However, according to Chaumat and Brenguier (2001), the lifetime of the heterogeneities would need to reach unrealistic values to significantly contribute to the observed broadening. Vaillancourt et al. (2002) showed that such broadening of DSDs from small-scale turbulence is increasingly negligible as the turbulence intensity increases, due to the shorter time the droplets are exposed to supersaturation perturbations, with the effects averaging out with time.

Turbulence can enhance the droplet collision rate, for instance, by inducing multiscale inhomogeneities in N_c (AYALA et al., 2008a; LU et al., 2010). Moreover, turbulent transport can lead to horizontal velocity differences in a droplet population (FRANKLIN et al., 2005; PINSKY et al., 2006) and enhance fall velocity differences (DÁVILA; HUNT, 2001; AYALA et al., 2008b), resulting in a larger collision rate. Turbulence also enhances the collision efficiency partly due to a reduction in the effect of the aerodynamic interactions between droplets (PINSKY et al., 2007; WANG et al., 2008; CHEN et al., 2018a). Chen et al. (2018b) stated that these effects of the condensational and collisional growth in turbulent flows should be analyzed simultaneously. Through direct numerical simulations of small-scale turbulent eddies in the inertial and dissipation range, they found that, contrary to the case of still air, in a turbulent flow, condensational growth can enhance droplet collisions. Chen et al. (2018b) argued that condensation can enhance the rate of collision-coalescence by creating medium-size (10-20 μm) droplets that are more likely to be collected by larger ones, and also by providing a large number of similar-sized droplets for which the turbulent enhancement of collisions is relatively more efficient.

The entrainment of dry air and aerosols has also been considered as a source of DSD broadening in clouds. Inhomogeneous mixing of entrained air, where the microphysical response is fast compared to the mixing timescale (in contrast to homogeneous mixing, where the opposite occurs), decreases N_c (LATHAM; REED, 1977; BAKER; LATHAM, 1979; BAKER et al., 1980; PINSKY et al., 2016), favoring the diffusional growth of the remaining droplets when the diluted air ascends. Burnet and Brenguier (2007) found that DSDs in diluted cloud volumes show features intermediate between the extremely inhomogeneous and homogenous mixing scenarios. The activation of new droplets from entrained aerosols also broadens the DSDs toward the smaller sizes, which can even result in bimodality (BAKER et al., 1980; BLYTH, 1993;

BRENGUIER; GRABOWSKI, 1993; LASHER-TRAPP et al., 2005; COOPER et al., 2013; HOFFMANN et al., 2015). However, there is no consensus regarding the role of these processes in the development of observed DSDs (KHAIN et al., 2000).

Khain et al. (2013) suggested that adiabatic processes play a dominant role in the formation of precipitation in deep convective clouds, given observational and modeling evidence showing that the formation of the first raindrops occurs in undilute or mostly undilute cloud cores. In this case, DSDs can be broadened through, for example, in-cloud activation of aerosols in parcels ascending adiabatically from cloud base, provided that the supersaturation above cloud-base is higher than the cloud-base supersaturation and there is a sufficient reservoir of potential CCN (PINSKY; KHAIN, 2002). Turbulence-enhanced collision-coalescence can also broaden DSDs in adiabatic (or nearly adiabatic) cloud cores. Hoffmann et al. (2017) found that, in the shallow maritime cumulus they modeled, raindrops were produced within a realistic time when turbulence-induced collision enhancement was considered, regardless of any other DSD broadening mechanisms. On the other hand, the simulations of Cooper et al. (2013) showed that the formation of the first raindrops from entrainment-broadened DSDs depends on the immersion of larger cloud drops (embryo raindrops) in regions with sufficiently high cloud water content, such as the nearly adiabatic cores assumed by Khain et al. (2013).

DSD broadening, rain generation and aerosol-cloud interactions are usually investigated using bin microphysics parameterizations. The suitability of this type of schemes for representating physically consistent DSD broadening mechanisms is explored in Chapter 5.

2.3 Parameterizations for the shape parameter of gamma DSDs

In bulk models that assume gamma DSDs, the shape parameter determines how spread droplet sizes are with respect to the mean diameter, i.e., $\mu = \frac{1}{\epsilon^2} - 1$, where ϵ is the relative dispersion (the ratio of the DSD standard deviation σ to its mean diameter D_m). Defining μ in terms of the model resolved quantities is uncertain, especially considering the high variability of observed μ values (MILES et al., 2000). In turn, these uncertainties impact the calculation of microphysical processes rates and therefore the evolution of clouds in the simulations. For instance, Igel and Heever (2017) found that differences in the value of μ accounted for most of the differences in the predicted condensation rate between bin and bulk approaches. For a cumulus cloud simulated with bulk microphysics using a kinematic framework, Morrison and Grabowski (2007) obtained a $\sim$ 75% increase in cloud water path when μ varied

from ~ 4.95 to ~ 12.72, considering $N_c \sim 300$ cm^{-3}.

Consequently, the description of μ is especially relevant for studies assessing the effects of aerosols on clouds. Several observational and modeling studies suggested that the effects of aerosol loading on ϵ (MARTIN et al., 1994; LIU; DAUM, 2002; PAWLOWSKA et al., 2006; LU et al., 2007), partially offset or enhance the aerosol second indirect effect, depending on the sign of the induced change in ϵ. Chen et al. (2016) showed that the classical theory of condensational growth in an adiabatic parcel predicts spectral broadening and spectral narrowing with increasing N_a in the aerosol-limited and the updraft-limited regimes, respectively. However, this does not explain the behavior above cloud base, where microphysical processes other than condensation play a key role. For instance, the experimental studies of Chandrakar et al. (2016), Chandrakar et al. (2018) showed that stochastic condensation in a turbulent environment leads to DSD narrowing as N_a increases, due to the reduction in supersaturation fluctuations associated with a fast microphysics response.

Several methods have been suggested for diagnosing μ in bulk schemes. In previous studies, μ was commonly assumed to be correlated with N_c, either positively (GRABOWSKI, 1998) or negatively (ROTSTAYN; LIU, 2003; PENG; LOHMANN, 2003; MORRISON; GRABOWSKI, 2007; THOMPSON et al., 2008). To account for factors that explain those two opposite correlations between ϵ (μ) and N_a found in observations, Liu et al. (2006) derived a diagnostic expression that predicts DSD narrowing with increasing w, based on classical condensational growth theory under adiabatic conditions. Later, Liu et al. (2008) obtained an empirical relationship that describes the variations of DSD shape as a function of the mean droplet mass based on observations. The expression for μ developed by Khvorostyanov and Curry (1999) and Khvorostyanov and Curry (2008) from analytical solutions of the kinetic equation of stochastic condensation attempts to reproduce the variability in DSD shape observed inside different clouds. It predicts both an increase and a decrease in μ with height depending on the balance among the effects of height above cloud base, dynamics (updraft strength and turbulence) and adiabaticity, thus implicitly depending on N_a. However, among many simplifications, Khvorostyanov and Curry (1999) and Khvorostyanov and Curry (2008) assumed that the variation of $N(D)$ with height does not depend on D, which might be a good approximation for thin clouds only. Evaluating their expression using observations is subject to a large uncertainty related to estimating the eddy diffusivity coefficient, and its implementation in models requires accurate estimations of the subgrid vertical velocity.

In Chapter 6, the main factors determining the spatial variability of ϵ (and μ) in observed and modeled convective clouds are analyzed, discussing the adequacy of μ parameterizations in bulk microphysics schemes.

3 METHODS

The main tools employed in the three parts of this study (Chapters 4, 5 and 6) are described here. Details that are specific of each study are described in the corresponding chapter.

3.1 Models

In the first part of this study (Chapter 4), a single-column model was employed to estimate the sensitivity of cloud-top DSDs to changes in the aerosol size distribution properties. In the second- and third-part studies (Chapters 5 and 6), 2D and 3D simulations were performed using the Weather and Research Forecasting model to study the distribution of DSD shape in convective clouds.

3.1.1 Single-column model

The single-column model employed here is based on the Kinematic Driver model (SHIPWAY; HILL, 2012), but instead of prescribing w, it is calculated at each time t and altitude z from the simplified equation:

$$\frac{dw}{dt} = \frac{g}{1+\gamma}\left(\frac{\theta - \theta'}{\theta'} - q_l\right) - \frac{\mu_E}{1+\gamma}w^2 \tag{3.1}$$

where $\gamma \approx 0.5$, g is the gravity acceleration; θ and θ' are the potential temperature in the model column and in the environment (assumed to be equal to the initial profile of θ), respectively; and q_l is the liquid water mixing ratio. The entrainment rate $\mu_E = \frac{C_E}{R}$ represents the lateral mass flux along the axis of a vertical plume of radius $R(t, z)$, where $C_E \approx 0.2$ is the entrainment parameter (PRUPPACHER; KLETT, 2012). The equation for the radius of the plume is:

$$\frac{d\ln R}{dt} = \frac{1}{2}\left(\mu_E w - \frac{d\ln\rho}{dt} - \frac{d\ln w}{dt}\right) \tag{3.2}$$

where ρ represents the density of the air.

The contribution of the entrainment in the equations for the evolution of θ, the water vapor mixing ratio (q_v) and N_a is expressed as $\mu_E(X - X')w$, where X and X' represent the in-cloud and environment values for each one of the mentioned magnitudes, respectively.

3.1.2 Weather and Research Forecasting model

The second and third parts of this study focused on the evolution of DSDs in an idealized warm cumulus cloud simulated by the Weather and Research Forecasting (WRF) model (SKAMAROCK et al., 2008).

In this model, a spheroid-shaped (4-km horizontal- and 1.5-km vertical-axis length) warm bubble is applied to force convective initiation. The θ perturbation is +3 K at the center of the bubble and decreases according to a cosine function toward its edges. Subgrid-scale turbulent mixing is included by evaluating the diffusion terms in physical space using a 1.5-order closure for the turbulent kinetic energy equation (SKAMAROCK et al., 2008). Additionally, to enhance resolved turbulent motions, small random perturbations ($\pm$ 0.05 K) are applied to the initial θ field. This configuration rapidly (within the first $\sim$ 5 min) produces turbulent-like motion and a $-5/3$ slope of the kinetic energy spectrum (PETERS et al., 2019).

3.1.3 Microphysics parameterizations

Most analyses in the three parts of this study were based in simulations with the Tel Aviv University (TAU) size-bin-resolved microphysics scheme. Additionally, some tests in third part of this study employed the two-moment bulk microphysics scheme of Morrison et al. (2009) (M09 hereinafter).

3.1.3.1 Bin microphysics

The TAU scheme that was first developed by Tzivion et al. (1987), Tzivion et al. (1989) and Feingold et al. (1988) with later applications and development documented in Stevens et al. (1996a), Reisin et al. (1998), Yin et al. (2000a), Yin et al. (2000b) and Rotach and Zardi (2007). TAU differs from other bin microphysical codes because it solves for two moments of the drop size distribution in each of the bins rather than solving the equations for only one moment, which allows for an accurate transfer of mass between bins and limits numerical diffusion across bins from growth processes (TZIVION et al., 1987; STEVENS et al., 1996a).

In the first (second and third) part(s) of this study, the cloud drop size distribution is divided into 34 (35) mass-doubling bins with radii ranging between 1.56 μm and 3200 μm (5080 μm), approximately. The method of moments is used to compute mass and number mixing ratios in each size bin resulting from collision-coalescence (TZIVION et al., 1987; FEINGOLD et al., 1988). Turbulent enhancement of collisions is not considered in the calculations of collision-coalescence here. In the first part of this

study, the method of Tzivion et al. (1989) is used to calculate the diffusional growth and evaporation of droplets. In the second and third parts, the top-hat method of moments from Stevens et al. (1996a) is employed. Solute and curvature effects on cloud droplet growth are neglected.

3.1.3.2 Bulk microphysics

The scheme of M09 is based on Morrison et al. (2005). It predicts mass and number mixing ratios of five hydrometeor species: cloud water, rain, cloud ice, snow and graupel/hail. Rain, ice, snow and graupel are assumed to follow exponential size distributions, and a gamma size distribution is assumed for cloud water. Microphysical processes acting as sinks and sources of hydrometeors are droplet activation/ice nucleation, condensation/deposition (evaporation/sublimation), autoconversion, self-collection, collection between hydrometeor species, melting/freezing, and ice multiplication.

In both bulk and bin microphysics schemes, aerosols with radii larger than a critical radius (r_c), for a given temperature and supersaturation (S), are instantaneously activated. According to Köhler theory:

$$r_c = \sqrt[3]{\frac{4A^3}{27S^2\kappa}} \qquad \text{with} \qquad A = \frac{2\sigma_s M_w}{\bar{R}T\rho_w}, \tag{3.3}$$

where σ_s is the surface tension of the solution/air interface, M_w is the molecular weight of water, $\bar{R}$ is the universal gas constant, ρ_w is the density of liquid water and κ is the hygroscopicity of the aerosols [1] (PRUPPACHER; KLETT, 2012). In the first part of this study, the initial size of activated droplets was determined following the approach of Ivanova (1977), which accounts for the slower growth rate of larger aerosols. In the second and third parts of this study, newly activated droplets were assumed to acquire a radius of $\sim 1.5\mu$m.

3.2 Observations

During September-October 2014, the end of the local dry season, the High Altitude and Long Range Research Aircraft (HALO) performed a series of research flights over the Amazon, as part of the ACRIDICON-CHUVA campaign (WENDISCH et al., 2016; MACHADO et al., 2014). The flight strategies with HALO during ACRIDICON-

[1] The hygroscopicity parameter here corresponds to the B parameter in Hudson and Da (1996), which is a particular case of the κ parameter in Petters and Kreidenweis (2007).

CHUVA included sampling the air below clouds for aerosol characterization and measurements of DSDs near the base and the top of growing convective cumuli in maritime, remote forest and deforested regions within or nearby the Amazon basin. To capture early stages of cumulus lifetime, the flights started close to local noon, when convection typically begins in the region.

This research uses data from six flights that sampled clouds in locations with contrasting aerosol conditions: the Arc of deforestation, where biomass burning and anthropogenic sources generated relatively high aerosol concentrations below cloud base ($\sim$ 2000 cm^{-3} to $\sim$ 4000 cm^{-3}), remote locations over the unperturbed rainforest, with highly homogeneous surface conditions and $N_a \approx 800$ cm^{-3} below cloud base, and the Atlantic ocean, near the mouth of the Amazon river, where N_a below cloud base was ≈ 500 cm^{-3}.

The Cloud Combination Probe (CCP) carried by HALO provided measurements of 1Hz particle size distributions during the flights. CCP employs a forward-scattering spectrometer, the Cloud Droplet Probe (CDP) (LANCE et al., 2010), which measures particles with diameter between 3 μm and 50 μm, and a gray-scale optimal array probe (CIPg, Cloud Imaging Probe Baumgardner et al. (2001), Molleker et al. (2014)), for particles with 50 μm $< D <$ 960 μm.

4 QUANTIFYING THE AEROSOL EFFECT ON DROPLET SIZE DISTRIBUTION AT CLOUD TOP

Given that the impact of aerosols on clouds and precipitation is modulated by physical processes at different scales, sensitivity studies should consider the *combined* effect of diverse factors. A first step should be to characterize cloud responses over the multidimensional space corresponding to the aerosol properties, i.e., number, size distribution shape and composition. As discussed in Section 2.1, most previous studies quantifying clouds' sensitivity over *multiple* combinations (of the order of hundreds or more) of values of the aerosol properties refer to cloud-base conditions. However, droplet activation can also occur at higher levels in convective clouds (SLAWINSKA et al., 2012; HOFFMANN et al., 2015). Observational studies have found evidence for the occurrence of significant secondary activation in Amazonian clouds (YEOM et al., 2019). Moreover, droplet advection propagates the impact of aerosols on cloud-base DSDs to higher levels, influencing growth processes and thus cloud evolution. Therefore, understanding the effect of aerosols requires an assessment of the evolution of DSDs throughout the clouds.

Using ACRIDICON-CHUVA measurements at the top of growing convective clouds near the Amazon basin, Cecchini et al. (2017) showed that the average aerosol effect on DSD shape inverts in sign with altitude, favoring broader droplet distributions close to cloud base but narrower DSDs higher in the clouds. Microphysical processes determining this contrasting behavior in ACRIDICON-CHUVA cloud-top observations are discussed in Chapter 6.

A relatively common approach in cloud physics modeling studies, especially when using large-scale models, is to treat the aerosol specie as a single-moment bulk variable, i.e. considering only one bin for the aerosols, and assuming particle sizes are log-normally distributed ("bulk PSD" hereinafter). This way, the growth of wet aerosols is not resolved, and aerosols with dry sizes larger than the critical size defined by the Köhler equation are immediately added to the first bin of the DSD. By fixing the shape of the PSD, those models guarantee a continuous supply of larger aerosols for activation, i.e., although N_a decreases according to the amount of activated droplets, the assumed log-normal shape implies the continuous presence of particles in the right tail of the PSD. Also, by always assigning the activated droplets to the smallest bin of the DSD, a very narrow shape is induced, spending a longer time to grow by diffusion until the collision-coalescence rate increases.

Here, cloud sensitivities to several aerosol properties were explored, for conditions

typical of Amazonian clouds. This analysis focused on the information from cloud-top, during the warm stages of cloud life-cycle. For estimating the sensitivities, an approach similar to Ward et al. (2010) was applied. But, besides analyzing DSDs' sensitivities to the aerosol hygroscopicity, the discussion was extended to include the impact of the aerosol-size-distribution's median size, standard deviation and number concentration on both droplet size and number concentration. Three different model configurations were employed here, in order to investigate the importance of representing entrainment and mixing, as well as the evolution of the PSD, in modelling studies related to the aerosol effect.

The results presented in this chapter were published in Hernández Pardo et al. (2019).

4.1 Modelling approach

The simulations performed here employed variations of the TAU bin microphysics parameterization (FEINGOLD et al., 1988; TZIVION et al., 1987; TZIVION et al., 1989) coupled to a single-column Eulerian framework (Section 3.1.1). In these simulations, a 1 s time step was used for both dynamics and microphysics algorithms during an integration time of 1800 s (30 min). For the vertical domain, a 120-level grid was defined with a 50-m grid spacing from 0 m to 6000 m of altitude.

Figure 4.1 - Vertical profiles of potential temperature (θ) and water vapor mixing ratio (q_v) employed as initial conditions in the simulations

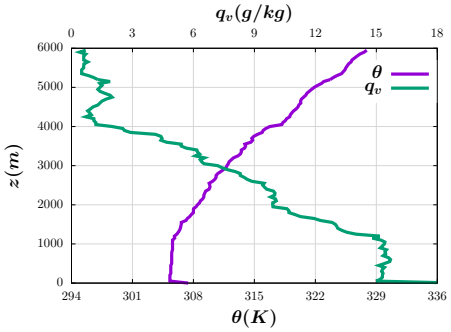

As initial conditions, vertical profiles of θ and q_v from an atmospheric sounding corresponding to 1730Z on September 11, 2014, from Manacapuru, Brazil (Figure 4.1) were provided. A constant temperature perturbation of 2.5 K was introduced at surface to force the convection.

4.1.1 Microphysics representation

The simulations performed in this work used the TAU size-bin-resolved microphysics scheme (Section 3.1.3.1). To account for changes in the PSD, a set of 19 bins for dry aerosols was introduced ("bin PSD" hereinafter), with radii (r) between 0.0076 μm and 7.6 μm, according to Kogan (1991). Aerosols were assumed to follow a log-normal size distribution in each grid point at the beginning of the simulation, and varied by advection, entrainment, activation and regeneration after droplet evaporation.

At a given temperature and supersaturation, the critical dry size (r_c, Equation 3.3) for droplet activation was computed from the Köhler equation. The initial bin for newly nucleated droplets was assigned according to its equilibrium size at 100% relative humidity, if $r < 0.09w^{-0.16}$. For larger aerosols, the initial radius of the droplet exceeded r by a factor of $K = 5.8w^{-0.12}r^{-0.214}$, due to the time these particles should normally take to reach its equilibrium size (IVANOVA, 1977). The consumption of water vapor by unactivated aerosols was not considered in the model. It was assumed that aerosols smaller than the activation size did not represent a significant sink of water vapor, given the great availability of humidity over the Amazon.

The aerosol regeneration was included here following the approach of Kogan et al. (1995) and Hill et al. (2008). It considers that large CCN particles grow to large cloud drops, which evaporates less efficiently than small droplets. Thus, small CCN will be released before large ones. As a result, the regenerated CCN are replenished to the aerosol bins starting by the smallest activated size, until the original number concentration in each bin is attained. If the number concentration of regenerated CCN is larger than the number concentration of "missing" aerosols (considering the initial PSD), which can happen by advection of droplets to levels different than those where they were nucleated, the "excess" of CCN will be log-normally distributed according to the initially defined median radius and geometric standard deviation. Conservation of the domain-averaged PSD is constrained in this method.

This scheme provides a reasonable way to parameterize the aerosol regeneration without using a 2D probability density function to track the aerosols. It does not consider the processing of the aerosols inside the cloud, therefore, it could induce errors in the activation rate in situations where the collision-coalescence process is a significant sink of small aerosols and a source of larger aerosols (LEBO; SEINFELD, 2011). However, this assumption was justified by the occurrence of low evaporation rates in the simulations performed here.

4.2 Sensitivity analysis

Here, the sensitivity of cloud-top values of N_c and the effective diameter of the DSD (D_{eff}) to variations in N_a, $\bar{r}_a$, the geometric standard deviation (σ_a) of the PSD and κ is analyzed, using ranges normally found in the Amazon atmosphere (GUNTHE et al., 2009; MARTIN et al., 2010; PÖHLKER et al., 2016) (Table 4.1). Two different sets of parameters were considered for the tests employing bins PSDs (Set 1) and the tests with bulk PSDs (Set 2).

The intervals of values for the aerosol properties were chosen in a way that allowed to explore the largest subset of realizable values of the parameters, while keeping a reasonable computation time. For certain combinations of the size distribution parameters, the PSD will be very narrow, with a very small concentration of aerosols larger than the activation threshold. This configuration, along with a small N_a, generated clouds with very low water content and unrealistically high supersaturations, when bin PSDs were used. To prevent this kind of situations, ranges were chosen as to produce averaged N_c at cloud top > 10 cm^{-3}. In order to test the response to $\bar{r}_a = 0.05$ μm, for instance, values of N_a larger than 800 cm^{-3}, and values of σ_a larger than 1.6 were used. Simulations with lower N_a, such as ~ 200 cm^{-3} generated realistic outputs only for larger $\bar{r}_a$ and σ_a. The choice of the intervals for the tested parameters was made as to guarantee a fully applicable parameter-space.

When bulk PSDs were used, assuming a fixed PSD affects the representation of the activation scavenging. This acts like a spurious source of aerosols with suitable sizes for activation, inducing unrealistically high values of N_c. Therefore, the values of the aerosol parameters tested had to be smaller in simulations with bulk PSDs than in simulations with bin PSDs.

Table 4.1 - Aerosol parameters considered for the sensitivity tests using bin and bulk PSDs: intervals for values and steps between them.

	Set 1: bin PSDs		Set 2: bulk PSDs	
Parameter	Interval	Step	Interval	Step
N_a (cm^{-3})	$800 - 3600$	400	$200 - 900$	100
$\bar{r}_a$ (μm)	$0.05 - 0.11$	0.01	$0.02 - 0.08$	0.01
σ_a (-)	$1.6 - 2.2$	0.1	$1.1 - 1.9$	0.2
κ (-)	$0.1 - 0.5$	0.1	$0.1 - 0.5$	0.1

The sensitivities were calculated as the slope of the linear fit between Y and X_i in logarithmic scale for normalization:

$$S_Y(X_i) = \left.\frac{\partial \ln Y}{\partial \ln X_i}\right|_{X_k} \tag{4.1}$$

where Y represents either N_c or D_{eff}, and X_i is the aerosol property affecting Y (i.e., N_a, $\bar{r}_a$, σ_a or κ). This way, $S_Y(X_i)$ represents the relative change in Y for a relative change in X_i (FEINGOLD, 2003; REUTTER et al., 2009; WARD et al., 2010). X_k represents the aerosol parameters that are held constant while calculating the sensitivity to X_i. A specific value of $S_Y(X_i)$ is obtained for each value of X_k.

The latter differentiates this approach from previous studies. For example, Feingold (2003) calculated a single linear regression between $\ln Y$ and $\ln X_i$ for all combinations of the aerosol parameters (other than X_i) tested, considering only two different subsets of N_a values. Similarly, Reutter et al. (2009) analyzed the sensitivities to $\bar{r}_a$, σ_a and κ for only three combinations of N_a and w. This analysis was then expanded by Ward et al. (2010), who calculated $S_{N_c}(\kappa)$ for several values of $\bar{r}_a$ and σ_a. Here, a more general approach is used by considering the responses of both N_c and D_{eff} to changes in each aerosol parameter, as a function of the other aerosol parameters.

4.3 Results

In the control simulation, initialized with $N_a = 800$ cm^{-3}, $\bar{r}_a = 0.08$ μm, $\sigma_a = 1.9$, and $\kappa = 0.1$, the cloud grew to a depth of 4000 m in about 30 min (Figure 4.2). Droplet growth by condensation and collision-coalescence during ascension led to larger D_{eff} at higher levels (Figure 4.2c). On the other hand, N_c was maximum at cloud-top for most times (Figure 4.2b). This can be associated with a combination of numerical dispersion in advection calculations and enhanced droplet activation. Droplet activation at cloud-top can be related to spurious high supersaturations induced from separately advecting temperature and water vapor (STEVENS et al., 1996b; GRABOWSKI; MORRISON, 2008), as well as to the increase in supersaturation produced due to the decrease in N_c through dilution (Section 5.3.3). Here it is assumed that the numerical errors influencing cloud-top characteristics in the simulations are systematic (therefore not affecting sensitivity calculations) and a detailed assessment of the effect of numerical artifacts in these simulations is left for future work.

Figure 4.2 - Evolution of the vertical velocity (w), the cloud droplet number concentration (N_c) and the droplet effective diameter (D_{eff}) in the control simulation.

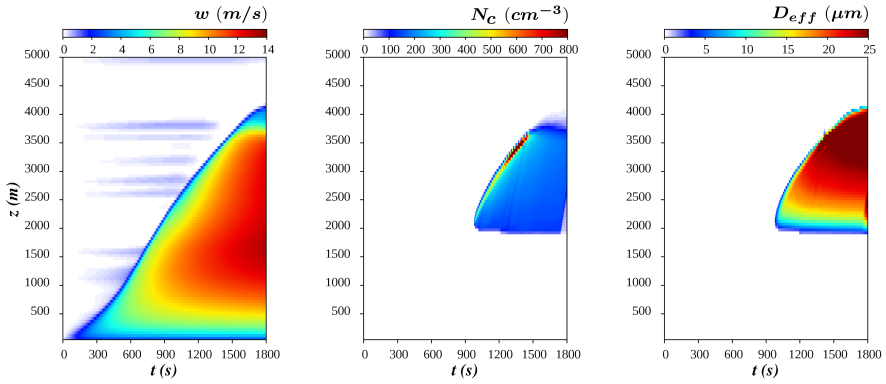

(a) (b) (c)

The cloud-top here was defined as the last model level, from surface to top, where $N_c > 1$ cm^{-3}. Following the cloud-top (Figure 4.3), two local maximums of N_c were found. The first one corresponded to small D_{eff} (< 5 μm) and was related to high activation rates at the initial stage of cloud development. The second one, which is also the global maximum, was more likely influenced by advection errors (note that the maximum values of N_c at cloud-top exceeded the initial value of N_a). Regardless of the fluctuations in N_c, the cloud-top values of D_{eff} increased monotonically with altitude, except at the end of the simulations, i.e., upper portions of the cloud-top trajectories in Figure 4.3, where the updraft decelerated.

Figure 4.3a shows the evolution of cloud-top DSDs for different values of N_a, and control values of $\bar{r}_a$, σ_a, and κ. As expected, increasing N_a led to higher N_c and smaller D_{eff}. Decreasing the supersaturation with increasing N_c, due to shorter phase relaxation timescale, slowed down the condensational growth. This is evidenced by the decrease in the slopes of the trajectories for $D_{eff} < 10$ μm, as N_a increases (note that at this stage condensation was the predominant droplet growth mechanism).

The initial fraction of activated droplets (N_c/N_a) was similar in all simulations in Figure 4.3a (close to one third), as a consequence of all other aerosol PSD parameters being kept constant. In reality, increased pollution in the Amazon is usually accompanied by changes in PSD shape and hygroscopicity, given the different nature of background and biomass-burning or urban particles (PÖHLKER et al., 2016; PÖHLKER et al., 2018). Therefore, it is important to analyze the effects of all aerosol

parameters to fully understand the pollution effect in Amazonian clouds.

Figure 4.3 - Cloud-top droplet number concentration (N_c) and effective diameter (D_{eff}) for different values of (a) the aerosol number concentration (N_a), (b) the median radius of the PSD ($\bar{r}_a$), (c) the geometric standard deviation of the PSD (σ_a), and (d) the aerosol hygroscopicity (κ), assuming control values of the aerosol parameters that are constant in each case. The markers represent averaged DSDs for time steps the top of the cloud stayed in the same model level. The aerosol parameter varied in each case is specified at the top of the corresponding graph. The control simulation is represented by black markers.

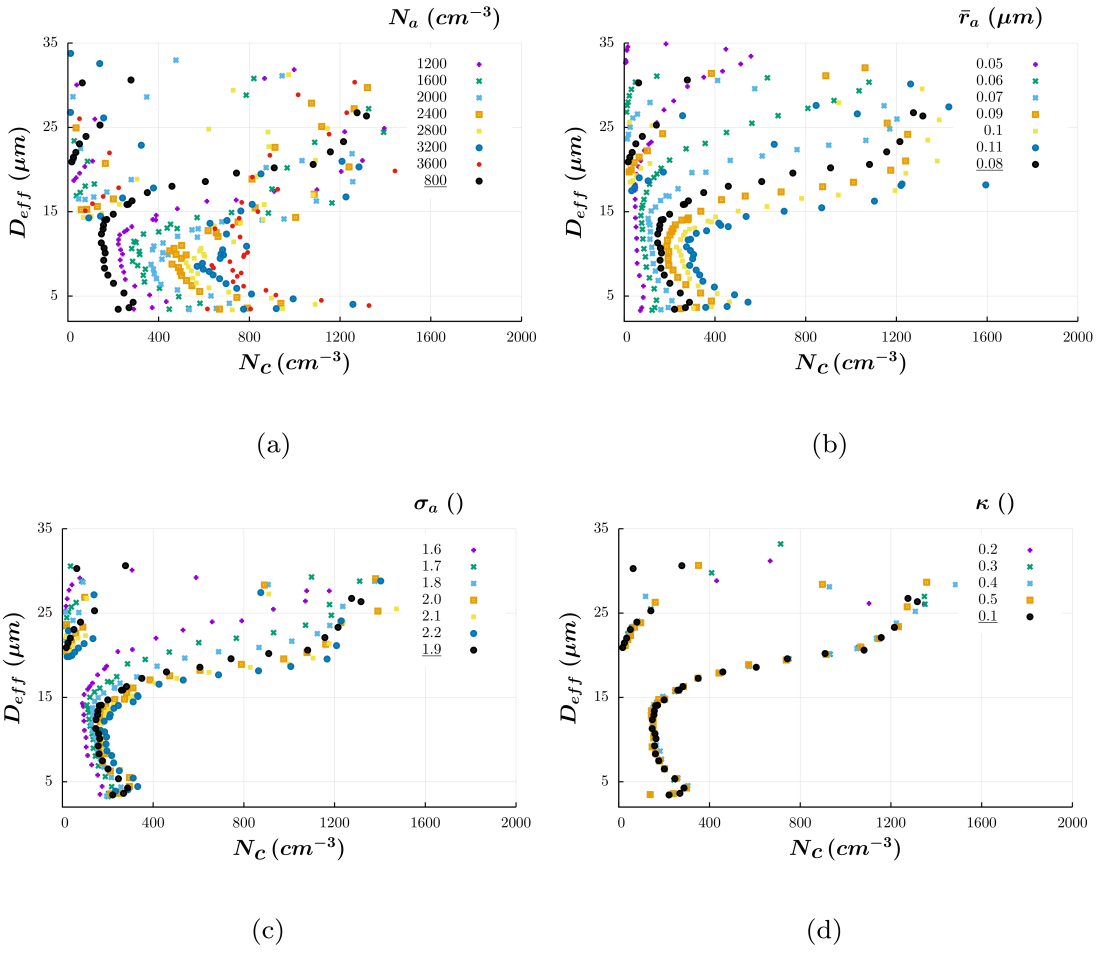

Figure 4.3b and 4.3c show the bulk properties of cloud-top DSDs for different values of $\bar{r}_a$ and σ_a, respectively, while keeping the other parameters at their control standards. The effects of increasing aerosol size and standard deviation were similar to the consequences of increasing N_a. By increasing $\bar{r}_a$ or σ_a, more droplets were

activated because of the larger availability of aerosols with sizes above the activation threshold. Thus, droplet activation increased, whereas condensational growth decreased.

The tests in Figure 4.3 evidence that the sensitivity decreased as N_a, $\bar{r}_a$ and σ_a increased. This behavior can be explained through the evolution of the supersaturation. The parcel supersaturation depends on the phase relaxation timescale (which is inversely proportional to the product of N_c and r_m) and on the vertical velocity. At large N_a, $\bar{r}_a$ and σ_a, the phase relaxation timescale tends to decrease, indicating a fast consumption of the water vapor "excess", which results in low supersaturations. In this situation, the sensitivity to N_a, $\bar{r}_a$ and σ_a decreases and changes in N_c (and D_{eff}) are mostly determined by changes in w. The extreme case would be the "updraft-limited" regime described by Reutter et al. (2009).

Figure 4.3d shows that the effect of varying κ in the range $0.1 - 0.5$ was very small. Nevertheless, Figure 4.3d corresponds to a single combination of N_a, $\bar{r}_a$ and σ_a, i.e., their control values. According to Ward et al. (2010), the sensitivity to κ can vary as a function of N_a and $\bar{r}_a$. Hence, to characterize the sensitivity of DSDs to aerosol properties, the multi-parameter space composed by combinations of realizable values of the parameters should be explored.

To illustrate how the sensitivity to each aerosol parameter varies as a function of the others, $S_{\bar{N}_c}(X_i)$ and $S_{\bar{D}_{eff}}(X_i)$ were calculated, with X_i being N_a, $\bar{r}_a$, σ_a or κ. $\bar{N}_c$ and $\bar{D}_{eff}$ are the time averages of N_c and D_{eff} at cloud-top for each simulation, respectively. From Equation 4.1, $S_{\bar{N}_c}(N_a)$, for example, is the slope of the linear fit between the values of $\bar{N}_c$ and N_a in logarithmic scale, for a given combination of $\bar{r}_a$, σ_a and κ. The sensitivity to one aerosol parameter can then be calculated a number of times equivalent to all possible combinations of the discrete values of the other parameters in Table 4.1.

Figures 4.4, 4.5, 4.6 and 4.7 show $S_{\bar{N}_c}(X_i)$ and $S_{\bar{D}_{eff}}(X_i)$ as a function of all values of N_a, $\bar{r}_a$, σ_a and κ considered. Generally, $\bar{N}_c$ can be almost three times more sensitive to changes in the aerosol parameters than $\bar{D}_{eff}$, which stems from the mathematical definition of these physical magnitudes (CECCHINI et al., 2017). For each value of the parameters represented in the x axes of Figures 4.4, 4.5, 4.6 and 4.7, there are several combinations of the remaining parameters.

Figure 4.4 - Sensitivities of the droplet number concentration and effective diameter to the aerosol number concentration ($S_{\bar{N}_c}(N_a)$ and $S_{\bar{D}_{eff}}(N_a)$, respectively) as a function of (a) the median radius of the PSD ($\bar{r}_a$), (b) the geometric standard deviation of the PSD (σ_a) and (c) the aerosol hygroscopicity (κ).

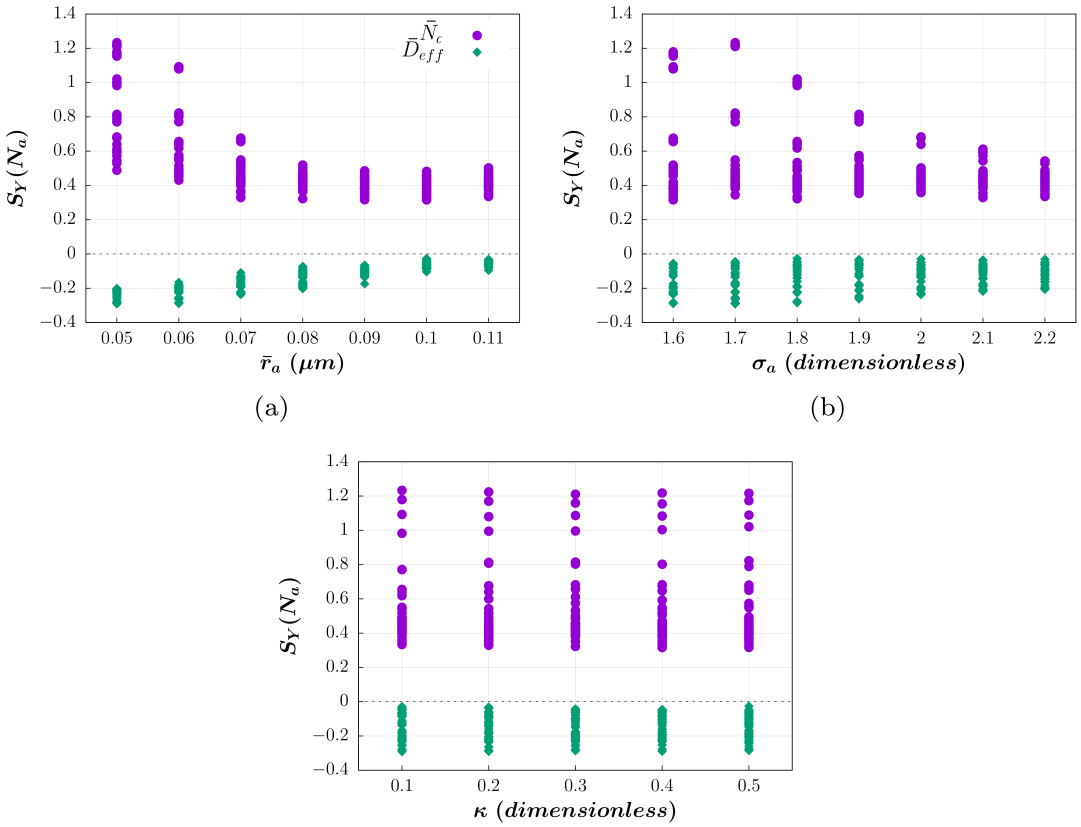

The impact of N_a on cloud droplets depended on the values of $\bar{r}_a$ and σ_a, but did not vary significantly with κ, as can be seen in Figure 4.4. Overall, the dispersion and maximum absolute value of $S_Y(N_a)$ increased as $\bar{r}_a$ and σ_a decreased, indicating that the relative importance of the aerosol properties for smaller aerosols can be very different from that for larger sizes.

Figure 4.5a shows that the sensitivity of the DSDs to the median radius of the aerosol population decreased for higher values of N_a and σ_a as well. Likewise, the minimum dispersion of the values of $S_Y(\bar{r}_a)$ coincided with the minimum of $|S_Y(\bar{r}_a)|$, on average. Conversely, the impact of κ on the sensitivity of cloud-top DSDs to $\bar{r}_a$ was negligible (Figure 4.5c).

Figure 4.5 - Sensitivities of the droplet number concentration and effective diameter to the median radius of the PSD ($S_{\bar{N}_c}(\bar{r}_a)$ and $S_{\bar{D}_{eff}}(\bar{r}_a)$, respectively) as a function of (a) the aerosol number concentration (N_a), (b) the geometric standard deviation of the PSD (σ_a) and (c) the aerosol hygroscopicity (κ).

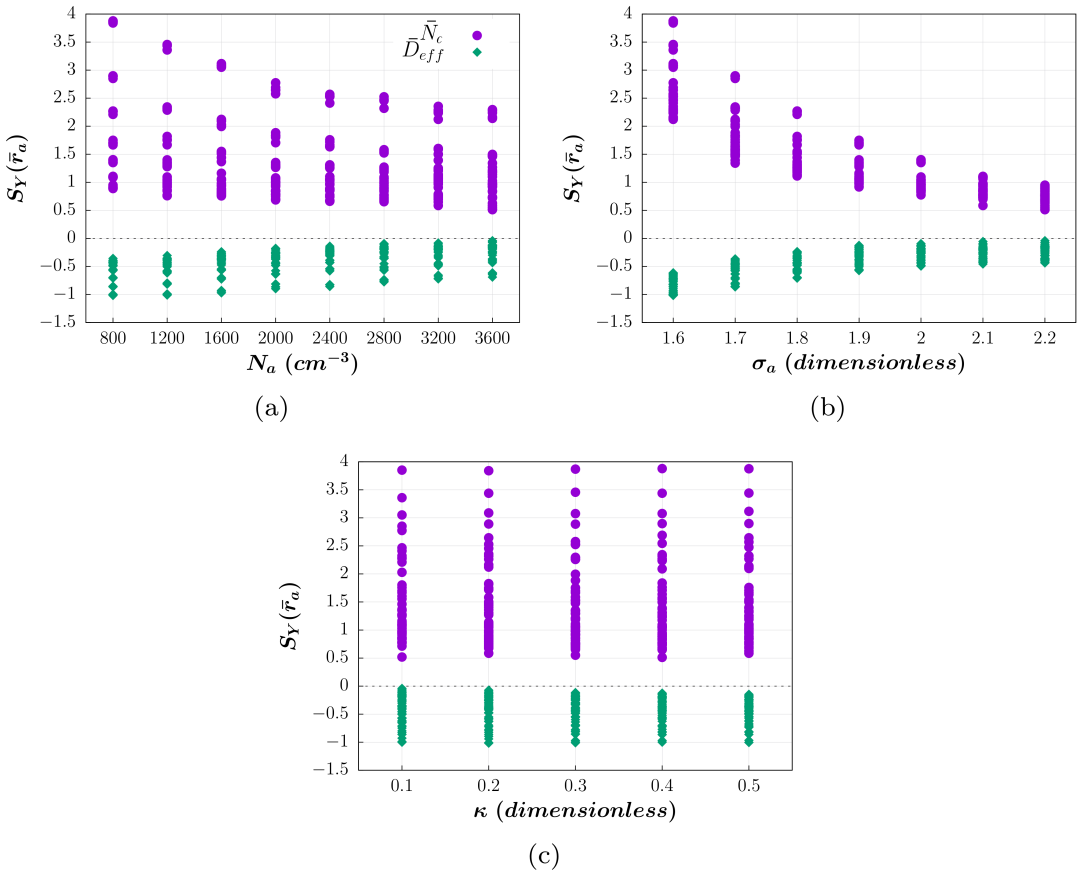

The sensitivity of cloud-top DSDs to σ_a ($S_Y(\sigma_a)$, Figure 4.6) behaved similarly to $S_Y(\bar{r}_a)$, substituting σ_a by $\bar{r}_a$ as the independent variable in Figure 4.6b. The absolute values of $S_Y(\sigma_a)$ were the highest among the sensitivities analyzed here. Nevertheless, it should be considered that the net effect of varying a parameter is determined by its range of realizable values. For example, assuming that the maximum and minimum values specified in Table 4.1 determine the variation of the parameters in a given situation, it follows that an increase of 0.6 in σ_a (a factor of 1.38) could increase $\bar{N}_c$ 10.6 times, while an increase of 0.06 μm in $\bar{r}_a$ (a factor of 2.2) could increase $\bar{N}_c$ 21.6 times, considering the maximum values of $S_{\bar{N}_c}(\sigma_a)$ and $S_{\bar{N}_c}(\bar{r}_a)$, respectively. In turn, an increase of 2800 cm^{-3} in N_a (a factor of 4.5), would only increase $\bar{N}_c$ 6.1 times at most.

Figure 4.6 - Sensitivities of the droplet number concentration and effective diameter to the geometric standard deviation of the PSD ($S_{\bar{N}_c}(\sigma_a)$ and $S_{\bar{D}_{eff}}(\sigma_a)$, respectively) as a function of (a) the aerosol number concentration (N_a), (b) the median radius of the PSD ($\bar{r}_a$) and (c) the aerosol hygroscopicity (κ).

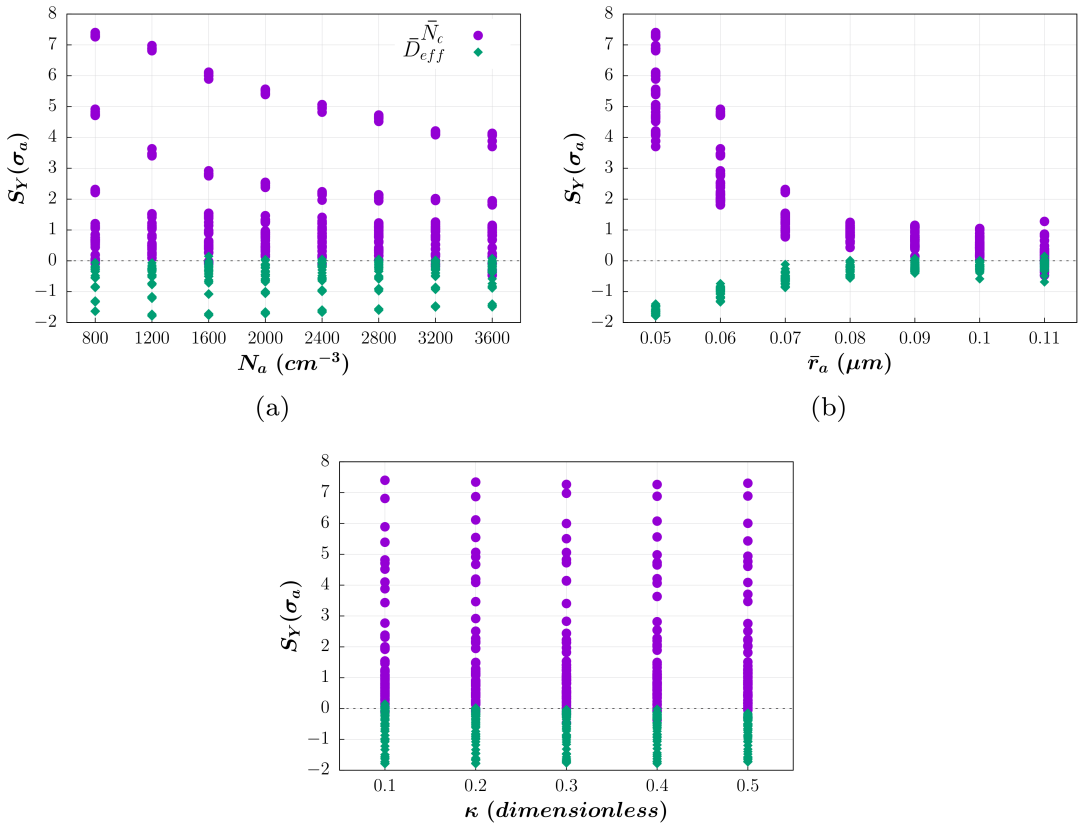

(a) (b)

(c)

Note that the sign of $S_Y(\sigma_a)$ changed as $\bar{r}_a$ increased (Figure 4.6b). This is related to variations in the effect of σ_a depending on the relation $\frac{r_c}{\bar{r}_a}$. Considering a log-normal PSD, the number of aerosols for which $r > r_c$, i.e., the number of activated droplets, is positively correlated with σ_a if $\frac{r_c}{\bar{r}_a} > 1$, and negatively correlated otherwise. If $\frac{r_c}{\bar{r}_a} = 1$, the number of activated droplets does not depend on σ_a. The positive values obtained by Feingold (2003) for the sensitivity of droplet size on σ_a, as well as the negative values reported by Reutter et al. (2009) for the sensitivity of N_c on σ_a may be caused by the inclusion of larger aerosols, favoring the diminution of $\frac{r_c}{\bar{r}_a}$.

Finally, the sensitivity to the aerosol hygroscopicity was the lowest between those analyzed here (Figure 4.7). Note that increasing κ by a factor of 5 increased $\bar{N}_c$ 1.38 times at most. This is consistent with the weak influence of κ on the sensitiv-

ities of cloud-top DSDs to N_a, $\bar{r}_a$ and σ_a, as discussed above. The quasisymmetric distribution of $S_Y(\kappa)$ with respect to the abscissa suggests the predominance of random errors introduced during the calculations, i.e., uncertainties in the algorithm that determines the cloud-top position, in the calculation of $\bar{N}_c$ and $\bar{D}_{eff}$, as well as in the fitting procedure employed to obtain $S_Y(\kappa)$, etc. Although κ had a very weak impact on cloud-top DSDs here, it should be considered that the effects of the aerosol composition can be significantly increased in conditions of weak updrafts (ERVENS et al., 2005; ANTTILA; KERMINEN, 2007; REUTTER et al., 2009). Therefore, simulations of other types of clouds, such as stratocumulus, can differ from these results.

Figure 4.7 - Sensitivities of the droplet number concentration and effective diameter to the aerosol hygroscopicity ($S_{\bar{N}_c}(\kappa)$ and $S_{\bar{D}_{eff}}(\kappa)$, respectively) as a function of (a) the aerosol number concentration (N_a), (b) the median radius of the PSD ($\bar{r}_a$) and (c) the geometric standard deviation of the PSD (σ_a).

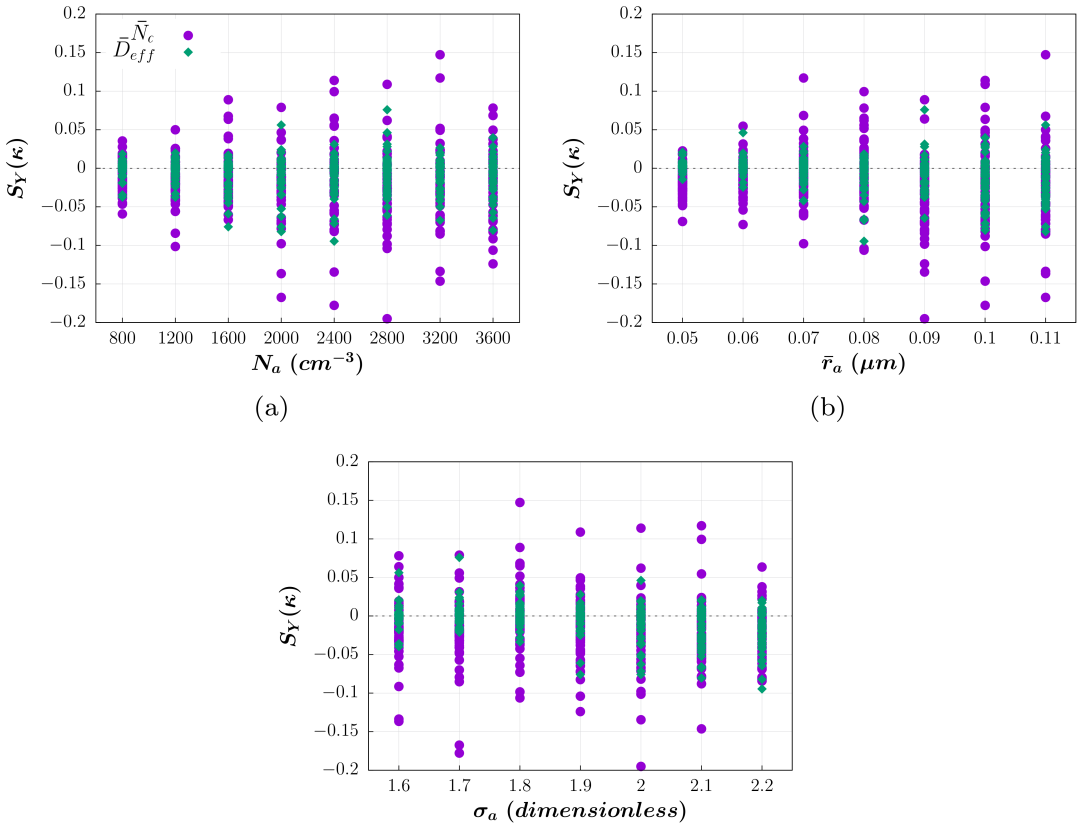

(a) (b) (c)

4.4 Effects of considering the entrainment and the evolution of the PSD

A simplified approach was adopted here in order to consider the mixing of in-cloud and environment air parcels. The model column was assumed to be located in the center of a plume with radius $R(t, z)$ (Equation 3.2), mixing homogeneously with radially entraining air. Entrainment affected the vertical velocity, the temperature, the humidity and the amount of aerosols in the column.

Past studies have assumed that entrainment and mixing in Amazonian clouds is close to the extreme inhomogeneous case, given that D_{eff} remained relatively constant horizontally (FREUD et al., 2011). However, recent studies of Pinsky et al. (2016) and Pinsky and Khain (2018) indicated that homogeneous and inhomogeneous mixing can be indistinguishable for polydisperse DSDs, especially for wide distributions, evidencing the inadequacy of previous in-situ techniques to identify mixing type (i.e., the so-called "mixing diagrams"). The present study considered only the homogeneous case as a first approximation, thus further investigation is needed to assess the effects of inhomogeneous mixing on aerosol-cloud interactions. In Chapter 5, the effect of mixing on DSD broadening is discussed using 2D cumulus simulations.

The results of the simulations with and without the parameterization of lateral entrainment are presented here as a proxy for the effect of the dilution caused by mixing with the air in the neighbourhood of the clouds. Nevertheless, since cloud-top mixing is likely affected by numerical diffusion and dispersion in advection calculations, future works investigating the impact of different advection schemes on cloud-top DSDs in cumulus simulations are highly recommended.

A bin representation of the aerosols allows the PSD to evolve freely. This way, after activation, the tail of the PSD can only be re-filled through advection, entrainment or evaporation. Also, by allowing newly activated droplets to occupy several bins of the DSD, collision-coalescence is accelerated. This method has been extensively employed (YIN et al., 2000b; YIN et al., 2000a; YIN et al., 2005; ALTARATZ et al., 2008; HILL et al., 2008; MECHEM; KOGAN, 2008) to substitute explicit calculation of aerosol diffusional growth, which demands more computational resources. Leroy et al. (2007) found reasonable consistency between both approaches, even at low bin resolutions. Figure 4.8 and 4.9 illustrate the sensitivity of cloud-top DSDs to the aerosol parameters using three different model configurations. The first column corresponds to the simulations described in the previous section, i.e., including bin PSDs and the parameterization of entrainment, the results without the parameterization of entrainment (but with bin PSDs) are shown in the second column, and the simula-

tions using bulk PSDs (with the parameterization of entrainment) are represented in the third column. In the first three rows in Figures 4.8 and 4.9, $\kappa = 0.1$. The last rows in these figures show $S_Y(\kappa)$ at $\sigma_a = 1.9$ and $\sigma_a = 1.5$, for the cases with bin and bulk PSDs, respectively. The effect of σ_a on $S_Y(\kappa)$ was similar to the effect of $\bar{r}_a$, which is represented in the y axes of the figures.

Figure 4.8 - Sensitivity of $\bar{N}_c$ to N_a (a,b,c), $\bar{r}_a$ (d,e,f), σ_a (g,h,i) and κ (j,k,l) in three different configurations of the model: with entrainment and bins for the aerosols (a,d,g,j), without entrainment (b,e,h,k) and without bins for the aerosols (c,f,i,l)

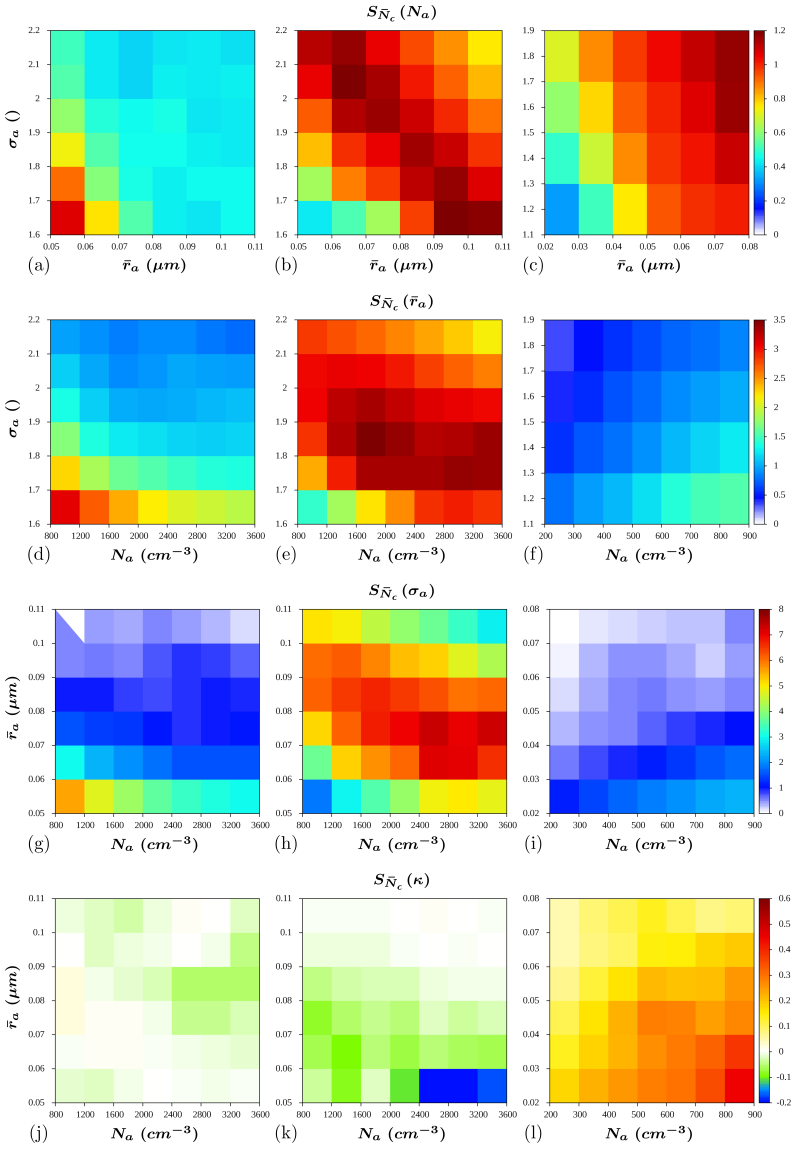

The values of the aerosol parameters in the tests with bulk PSDs (third column in Figures 4.8 and 4.9) were generally smaller than those in the tests with bin PSDs. The reason is that larger values of the aerosol parameters in tests with bulk PSDs induced high droplet activation rates that led to unrealistic values of N_c. Note that assuming a fixed PSD is equivalent to redistributing the aerosols remaining after activation as to cover the original size interval, replenishing the tail of the PSD artificially.

Figure 4.9 - Sensitivity of $\bar{D}_{eff}$ to N_a (a,b,c), $\bar{r}_a$ (d,e,f), σ_a (g,h,i) and κ (j,k,l) in three different configurations of the model: with entrainment and bins for the aerosols (a,d,g,j), without entrainment (b,e,h,k) and without bins for the aerosols (c,f,i,l)

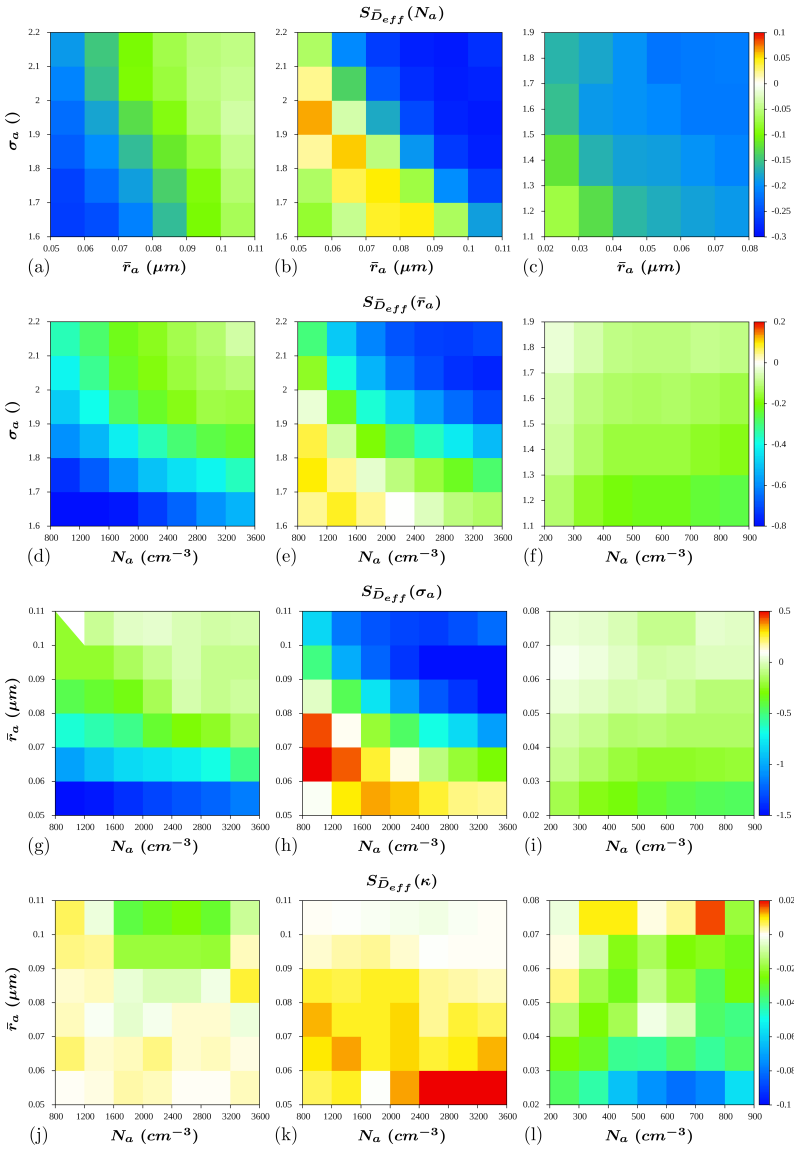

Figure 4.8b,e,h,k show that, without entrainment, $S_{\bar{N}_c}(X_i)$ was lower for low values of N_a, $\bar{r}_a$ and σ_a, consistent with faster depletion of aerosol particles with suitable sizes for activation as N_a, $\bar{r}_a$ and σ_a decreased. Another local minimum of $S_{\bar{N}_c}(X_i)$ was found at large N_a, $\bar{r}_a$ and σ_a, likely associated with lower supersaturations in clouds with higher N_c. This is in contrast to the case with parameterized entrainment, where the addition of aerosols from the environment combined with the dilution of cloud properties enhanced the supersaturation depletion and inhibited the aerosol depletion effects.

When the entrainment was not considered, $S_{\bar{D}_{eff}}(N_a)$, $S_{\bar{D}_{eff}}(\bar{r}_a)$ and $S_{\bar{D}_{eff}}(\sigma_a)$ tended to be positive for an intermediate interval of N_a, $\bar{r}_a$ and σ_a, and negative otherwise (Figure 4.9b,e,h). A plausible explanation for positive values of $S_{\bar{D}_{eff}}(X_i)$ in this case is the existence of high supersaturations in intense updrafts when entrainment is neglected. Since the corresponding $S_{\bar{N}_c}(N_a)$, $S_{\bar{N}_c}(\bar{r}_a)$ and $S_{\bar{N}_c}(\sigma_a)$ are positive (Figure 4.8b,e,h), N_c increases with increasing N_a, $\bar{r}_a$ and/or σ_a. But, if this increment in N_c is not as intense as needed to cause a notable supersaturation depletion, the condensational growth may not be significantly affected. Also note that proportional increments in N_c throughout the size domain may lead to higher D_{eff} simply because higher moments of the DSD give more weight to larger droplets (D_{eff} is the ratio of the third to the second DSD-moments).

In Figures 4.8c and 4.9c it can be seen that, when bulk PSDs were used, the absolute values of $S_Y(N_a)$ increased monotonically as $\bar{r}_a$ and σ_a increased. In this case, the sensitivities were not evidently affected by the supersaturation depletion at higher $\bar{r}_a$ and σ_a discussed above, because assuming a fixed PSD implied that there was always a certain amount of aerosols with $r > r_c$.

In simulations with bulk PSDs, the absolute value of $S_Y(\bar{r}_a)$ ($S_Y(\sigma_a)$) in Figures 4.8f (4.8i) and 4.9f (4.9i) increased with decreasing σ_a ($\bar{r}_a$) and increasing N_a, consistent with the results of Feingold (2003) and Rissman et al. (2004). Overall, the maximum absolute values of $S_Y(\bar{r}_a)$ and $S_Y(\sigma_a)$ were smaller than those in simulations with bin PSDs.

In turn, Figures 4.8l and 4.9l show that, in simulations with bulk PSDs, $S_Y(\kappa)$ increased in absolute value for higher N_a and smaller $\bar{r}_a$, in agreement with the results of Ward et al. (2010). $\bar{N}_c$ and $\bar{D}_{eff}$ were generally more sensitive to κ in simulations with bulk PSDs, where $S_Y(\kappa) \sim 0.5 S_Y(N_a)$, than in simulations with bin PSDs. One of the most relevant differences between simulations with bulk and bin PSDs was the change in the sign of $S_Y(\kappa)$. In the tests with bin PSDs, negative

(positive) values of $S_{\bar{N}_c}(\kappa)$ ($S_{\bar{D}_{eff}}(\kappa)$) may be associated with a reduction in the droplet activation rate, due to a faster depletion of the larger aerosols as κ increased. Not representing this effect can explain the obtention of positive (negative) values of $S_{\bar{N}_c}(\kappa)$ ($S_{\bar{D}_{eff}}(\kappa)$) in the simulations with bulk PSDs.

Overall, these analyses show that increases in N_a, $\bar{r}_a$ and σ_a produced higher $\bar{N}_c$ (positive sensitivity) and smaller $\bar{D}_{eff}$ (negative sensitivity) when both entrainment and aerosol bins were included in the simulations. This is consistent with the results of Cecchini et al. (2017), who found cloud-top averages of $S_{\bar{N}_c}(N_a)$ and $S_{\bar{D}_{eff}}(N_a)$ of 0.84 and -0.25, respectively, from aircraft measurements over the Amazon forest.

The sensitivities reported by Feingold (2003), Reutter et al. (2009), Ward et al. (2010) are included within the range of sensitivities presented here. However, since this study focused on cloud-top DSDs, instead of cloud base, comparing these results and previous studies is not straightforward. For example, the rate of aerosol and water vapor depletion at cloud-base determines the rate of droplet activation at higher levels. This way, high cloud-base supersaturations can lead to intense activation initially, but lower activation rates higher in the clouds, due to the decrease in the phase relaxation timescale and/or the scavenging of aerosols related to cloud-base activation. The response of the cloud to changes in the aerosol properties in this case may be different from that with a moderate and more uniformly distributed activation rate, or from that at a single level, such as the base of the cloud. In simulations with bulk PSDs, the decrease in the number of aerosols with suitable sizes for activation is slower than in simulations with bin PSDs. This explains the similarity between the sensitivities derived from simulations with bulk PSDs here and previous studies.

Results evidenced that $\bar{r}_a$ had a large impact on the sensitivity of the cloud to the other aerosol parameters analyzed. To further illustrate this, Figure 4.10 shows the mean and standard deviation of $\bar{N}_c$ and $\bar{D}_{eff}$ for each value of N_a in simulations: with entrainment and bin for aerosols (a-b), without entrainment (c-d), and without bins for aerosols (e-f). The length of the bars represents the standard deviation associated with different values of $\bar{r}_a$, σ_a and κ.

With the first model configuration (including a parameterization of entrainment and bin PSDs), the characteristics of the DSDs at the top of the cloud were not sufficiently determined by N_a, especially for smaller aerosol radii (Figure 4.10b). For instance, increasing N_a by a factor of 3 in Figure 4.10b, i.e., from 800 cm^{-3} to 2400 cm^{-3}, there is significant overlap of the corresponding standard deviation

bars in the phase-space. These results highlight the importance of considering the characteristics of the PSDs in aerosol-cloud interaction studies, especially when $\bar{r}_a \leq 0.08$ μm. The impact of changing $\bar{r}_a$ and σ_a can be comparable to that caused by changes in N_a.

Figure 4.10 - Mean and standard deviation of $\bar{N}_c$ and $\bar{D}_{eff}$ at cloud top for $\bar{r}_a > 0.08$ μm (a,c,e) and $\bar{r}_a < 0.08$ μm (b,d,f) in simulations with entrainment and bins for the aerosols (a,b), without entrainment (c,d) and without bins for the aerosols (e,f).

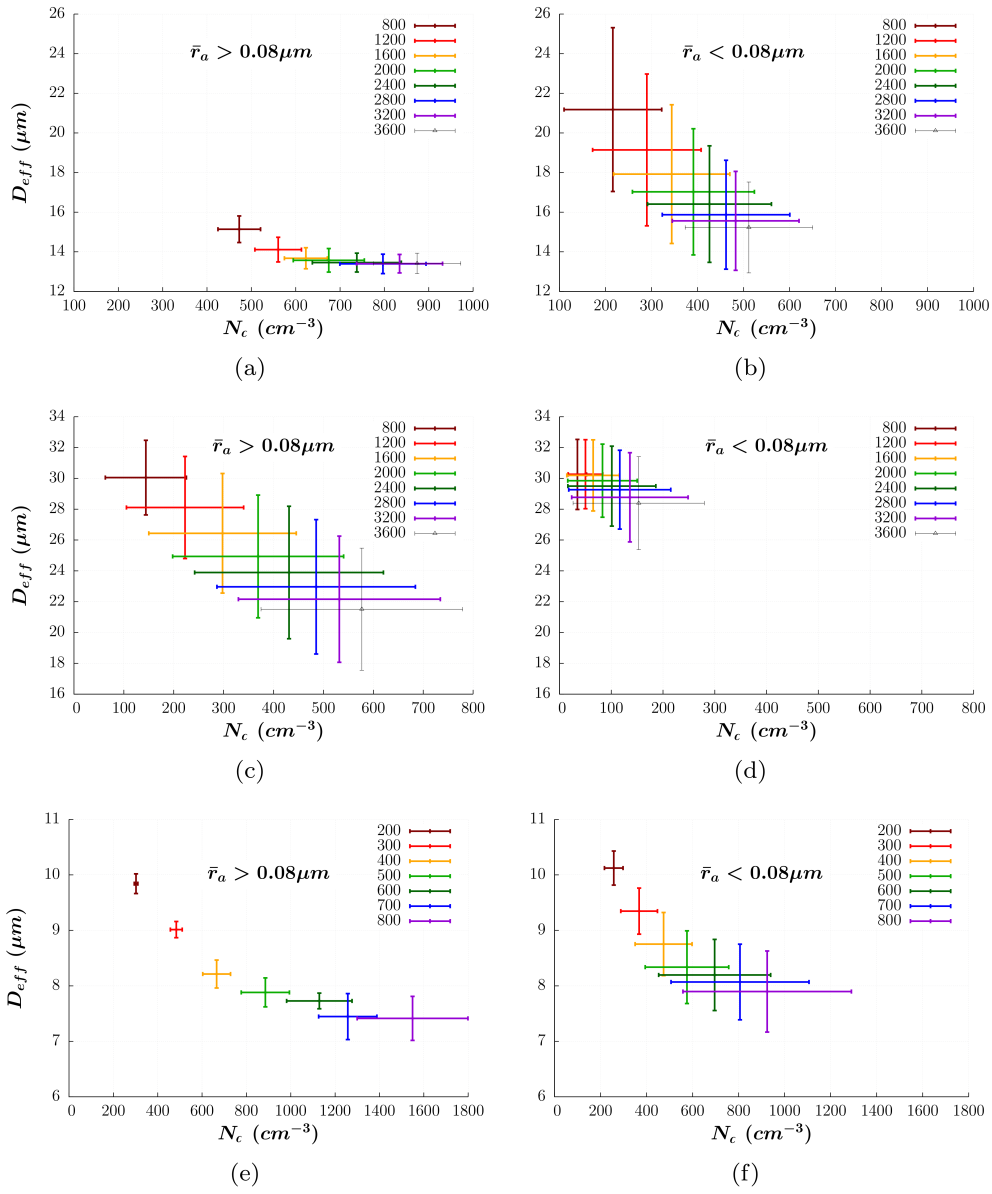

In turn, Figure 4.10c-d shows that, in simulations neglecting the entrainment, there was a high variability of $\bar{N}_c$ and $\bar{D}_{eff}$ for both small and large aerosols. In this case, the standard deviation of a point was primarily a function of its location in the $N_c - D_{eff}$ phase-space. For instance, points located at the left upper corner in Figure 4.10c had approximately the same standard deviation than points at the same location in Figure 4.10d. Therefore, the difference between simulations with small and large aerosols resided on the position of the points: for smaller aerosols (Figure 4.10d), $\bar{N}_c$ was lower and $\bar{D}_{eff}$ was larger than for larger aerosols (Figure 4.10c).

On the other hand, results indicate that the role of N_a may be overestimated, with respect to the role of other aerosol parameters, when bulk PSDs are employed. In that case (Figure 4.10e-f), there was a reduction of the overlapping between the standard deviation bars, especially for larger aerosols.

4.5 Remarks

In this study, the influence of N_a, $\bar{r}_a$, σ_a and κ on N_c and D_{eff} at the top of an idealized warm cumulus was illustrated, for conditions typical of Amazonian clouds. Results showed that the responses of cloud-top DSDs to changes in the aerosol parameters have a pronounced dependency on the model assumptions regarding the entrainment and the evolution of the aerosol size distribution, which modulate the aerosol and supersaturation depletion effects, in agreement with Reutter et al. (2009). Furthermore, these sensitivities were found to be remarkably affected by the position within the multidimensional space defined by all the aerosol parameters analyzed, especially by the value of $\bar{r}_a$. This expands the results of Ward et al. (2010) by reinforcing that w/N_a, or supersaturation-based regimes (REUTTER et al., 2009), cannot fully predict the dependence of CCN activity on composition *and on PSD shape*.

Overall, when the droplet activation was favored, an increase in N_c was accompanied by a decrease in D_{eff}. Nevertheless, since these sensitivity calculations include the evolution of the *cloud-top* with time and height, the results are not directly comparable with the sensitivities obtained by previous studies at *cloud-base*. In simulations with bin PSDs, the rate of activation at a certain time had a strong impact on the intensity of the activation afterwards, due to a faster depletion of aerosols in the right tail of the PSDs, generating distinctive regimes in the sensitivity of cloud-top DSDs to aerosols. In turn, the assumption of bulk PSDs determined a slower depletion of activable aerosols in the simulations. The responses of cloud-top DSDs to

changes in the aerosol properties in that case were more uniformly distributed in time and space than in simulations with bin PSDs, thus leading to similar results than the cloud-base sensitivities of Feingold (2003), Reutter et al. (2009) and Ward et al. (2010).

The simulations performed here can represent average characteristics of shallow cumulus. However, in real clouds, important processes such as turbulence and mixing can introduce significant differences with respect to these highly idealized simulations. Full dynamical models account for dynamics feedbacks and several sub-grid scale processes that could enhance or reduce the range of sensitivities obtained here. Nevertheless, the qualitative aspects of these results, i.e., the dependency of DSD sensitivities to aerosols on the specific combination of aerosol parameters, is expected to remain valid even in presence of multi-scale buffering mechanisms.

5 DROP SIZE DISTRIBUTION BROADENING MECHANISMS IN A BIN MICROPHYSICS EULERIAN MODEL

The gap between the classical effects of condensational growth and collision-coalescence has been the center of many modeling and observational studies for decades. To this end, modeling studies have usually been based on bin-microphysics numerical simulations. For instance, Khain et al. (2013) employed 2D and 3D Eulerian models with bin microphysics to show that the formation of the first raindrops occurs in undilute or mostly undilute cloud cores. They found that simulations of rain formation using coarser grid spacings (KHAIN et al., 2008) agreed well with their 50 m grid-spacing simulations, yielding similar heights of raindrop formation and similar response of this height to variations in N_a. However, bin microphysics schemes suffer from numerical diffusion in mass/size space, which acts as an artificial source of DSD broadening in modeled clouds. Morrison et al. (2018) showed that the numerical diffusion associated with vertical advection in Eulerian models, combined with growth in radius or mass space in bin microphysics schemes can artificially broaden DSDs due to the numerical mixing of droplets from neighboring vertical levels. Because ascending/descending air parcels undergo adiabatic cooling/warming from expansion/compression, droplets moving up/down in cloudy parcels simultaneously experience condensation/evaporation. Mixing associated with numerical diffusion from *vertical* advection (hereinafter, vertical numerical diffusion) does not account for the growth/shrinkage of droplets in ascending/descending air and thus constitutes an unphysical DSD broadening mechanism. This is in contrast to *horizontal* advection or mixing of droplets, which is not accompanied by the expansion or compression of air and associated adiabatic cooling or warming. According to Morrison et al. (2018), the effects of unphysical DSD broadening from vertical numerical diffusion are more pronounced at lower vertical resolutions. They suggested this numerical broadening may compensate for underrepresented horizontal variability and mixing of different droplet populations in typical large-eddy simulation (LES) configurations, or the neglect of other physical mechanisms that could broaden DSDs in real clouds. Indeed, Witte et al. (2019) found that the turbulent enhancement of collision-coalescence had a relatively minor impact on the bulk microphysical characteristics of clouds obtained with a LES model using bin microphysics, which may have been modulated by vertical numerical diffusion.

In this chapter, an investigation of the role of physical DSD broadening processes in an Eulerian bin-microphysics model is presented. This was studied using idealized 2D and 3D simulations of an isolated warm (ice-free) cumulus cloud, following

the approach of "mechanism denial" experiments, whereby specific processes are turned off individually or in combination to understand their influence. The contributions of various processes to DSD broadening and evolution were identified with various sensitivity tests, including evaporation, in-cloud droplet activation, collision-coalescence, turbulent mixing, and cloud dilution from entrainment and mixing with cloud-free air. The role of model grid spacing on these contributions was also examined. In this way, possible effects of artificial DSD broadening from vertical numerical diffusion were analyzed, given the strong sensitivity of this broadening to the model vertical resolution.

The results presented in this chapter were published in the *Journal of the Atmospheric Sciences* (HERNÁNDEZ PARDO et al., 2020)©American Meteorological Society. Used with permission.

5.1 Model description

This study focuses on the evolution DSDs within an idealized warm cumulus cloud, simulated by the WRF model (SKAMAROCK et al., 2008) with TAU two-moment bin microphysics scheme (Chapter 3). The initial conditions followed vertical profiles of θ and q_v from an atmospheric sounding launched at 1730Z on 11 September 2014 from Manacapuru, Brazil (HOLDRIDGE et al., 2014) (Figure 5.1), as part of the Observations and Modeling of the Green Ocean Amazon (GoAmazon2014/5) Experiment (MARTIN et al., 2016). This allowed to compare the model output with the in-cloud measurements obtained by the coordinated ACRIDICON-CHUVA Experiment (WENDISCH et al., 2016; MACHADO et al., 2014).

In both 2D and 3D simulation, a 20-km horizontal domain with open lateral boundary conditions was used. The top of the model vertical grid was located at 10 km altitude, with a 3-km damping layer, where the vertical grid-spacing was coarser than at lower levels for a more efficient use of computational resources. Analyses here consider only simulations times before the cloud reached the bottom of the damping layer.

Figure 5.1 - Vertical profiles of potential temperature (θ) and water vapor mixing ratio (q_v) employed as initial conditions in the simulations.

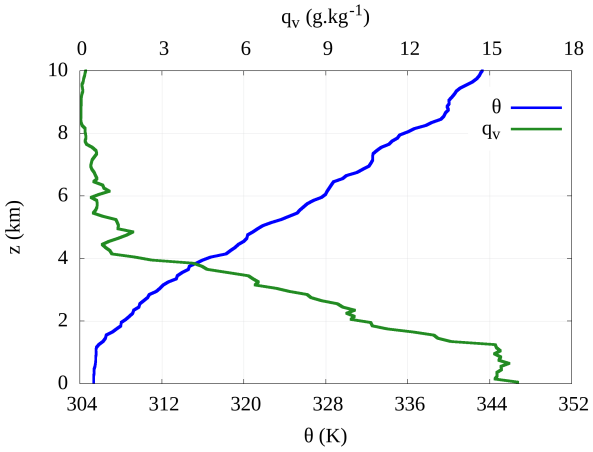

References to the model grid spacing in the text follow a "(vertical grid spacing)×(horizontal grid spacing)" format, where the grid spacings are listed in meters; however, the value of the vertical grid spacing specified in this way represents only an approximate value as the vertical grid spacing slightly decreased with height below the damping layer. Four resolution configurations were employed: 100×100, 30×30, 30×100 and 100×30. A 1-s time step was used for the 100×100 simulations. For the simulations with a grid spacing of 30 m in at least one spatial dimension, the time step was set to 0.25 s.

In this version of the TAU microphysics, the cloud drop size distribution was divided into 35 mass-doubling bins with radii ranging between 1.56 μm and 5080 μm, approximately. Aerosols were represented by a constant $N_a = 200$ cm^{-3} and were assumed to follow a log-normal size distribution, with $\bar{r}_a = 0.08$ μm and $\sigma_a = 1.9$ μm. κ was set as 0.1, based on previous studies of aerosol properties over the Amazon (GUNTHE et al., 2009; MARTIN et al., 2010; PÖHLKER et al., 2016). New droplets were activated whenever the number mixing ratio of activated CCN (N_{act}) exceeded the number mixing ratio of existing cloud droplets (N_d)[1]. Then, the change in N_d due to activation $\left(\frac{dN_d}{dt}\right)_{act}$ is

$$\left(\frac{dN_d}{dt}\right)_{act} = \left\{ \begin{array}{cc} \frac{(N_{act}-N_d)}{\Delta t} & N_{act} \geq N_d \\ 0 & N_{act} < N_d \end{array} \right\}. \tag{5.1}$$

[1]Note that N_d (mg^{-1}) is used here, instead of N_c (cm^{-3})

where Δt is the model time step. N_{act} represents the number mixing ratio of aerosols with radii larger than a critical radius (r_c), following Köhler theory (Equation 3.3). All newly activated droplets were placed in the smallest size bin (droplet mass between 1.6×10^{-11} g and 3.2×10^{-11} g, approximately); thus, the effects of large aerosols and GCCN were not explored.

Note that, by not explicitly representing aerosol scavenging, this method can overestimate the activation rate in the model (Chapter 4) compared to a real cloud with the same background aerosol field. Moreover, this simplified approach can lead to an artificial enhancement of droplet activation when used in combination with N_d sink processes. For instance, if the rate of collision-coalescence reduces N_d below the diagnosed N_{act} then activation occurs, which can broaden the DSDs. A strategy adopted by previous studies to avoid relying on N_d as a proxy for the number of already activated CCN, without actually prognosing aerosols, is to track the number of activated CCN (MORRISON; GRABOWSKI, 2008). This method is useful, especially when collision-coalescence is included, but does not address potential problems related to neglecting aerosol regeneration and scavenging, for example. Here, different idealized configurations are tested to understand the effects of activation on DSD broadening (see tests ACT and CBACT described in Table 5.1).

5.2 Droplets in an Eulerian-model rising thermal

Here, the modeled cloud microphysical evolution is characterized by N_d, D_m, σ, the difference between the diameters of the 99^{th} and 50^{th} percentiles of the DSD (ΔD_{99}), and the collision-coalescence rate (CCrate) computed as the total (summed across bins) number concentration of droplets collected per second. For all subsequent analysis and plots, cloudy points are defined as those with $N_d \geq 1$ mg^{-1} (this threshold defines the "cloud mask"). Figure 5.2 illustrates the distribution of these variables in vertical cross-sections located at the center of the 3D-modeled cloud at different times. For complementing the analysis, Figure 5.3 shows the distributions of supersaturation and the droplet activation and condensation/evaporation rates. The latter indicates the rate of change of the mean droplet size at a given point due to diffusion of water vapor to/from the droplets[2].

[2]The terms "condensation" and "condensational growth" here refer to the growth of activated droplets by water vapor diffusion, whereas the diffusional growth of unactivated droplets is implicit in the so-called "activation" process. The same applies to evaporation.

Figure 5.2 - Vertical cross-sections of a) number mixing ratio (N_d), b) mean diameter (D_m), c) DSD standard deviation (σ), d) difference between the diameters of the 99^{th} and 50^{th} percentiles of the DSD (ΔD_{99}), and e) rate of collision-coalescence (CCrate) for different times in the 3D simulation. Each row represents a different simulation time, labeled to the right of the plots.

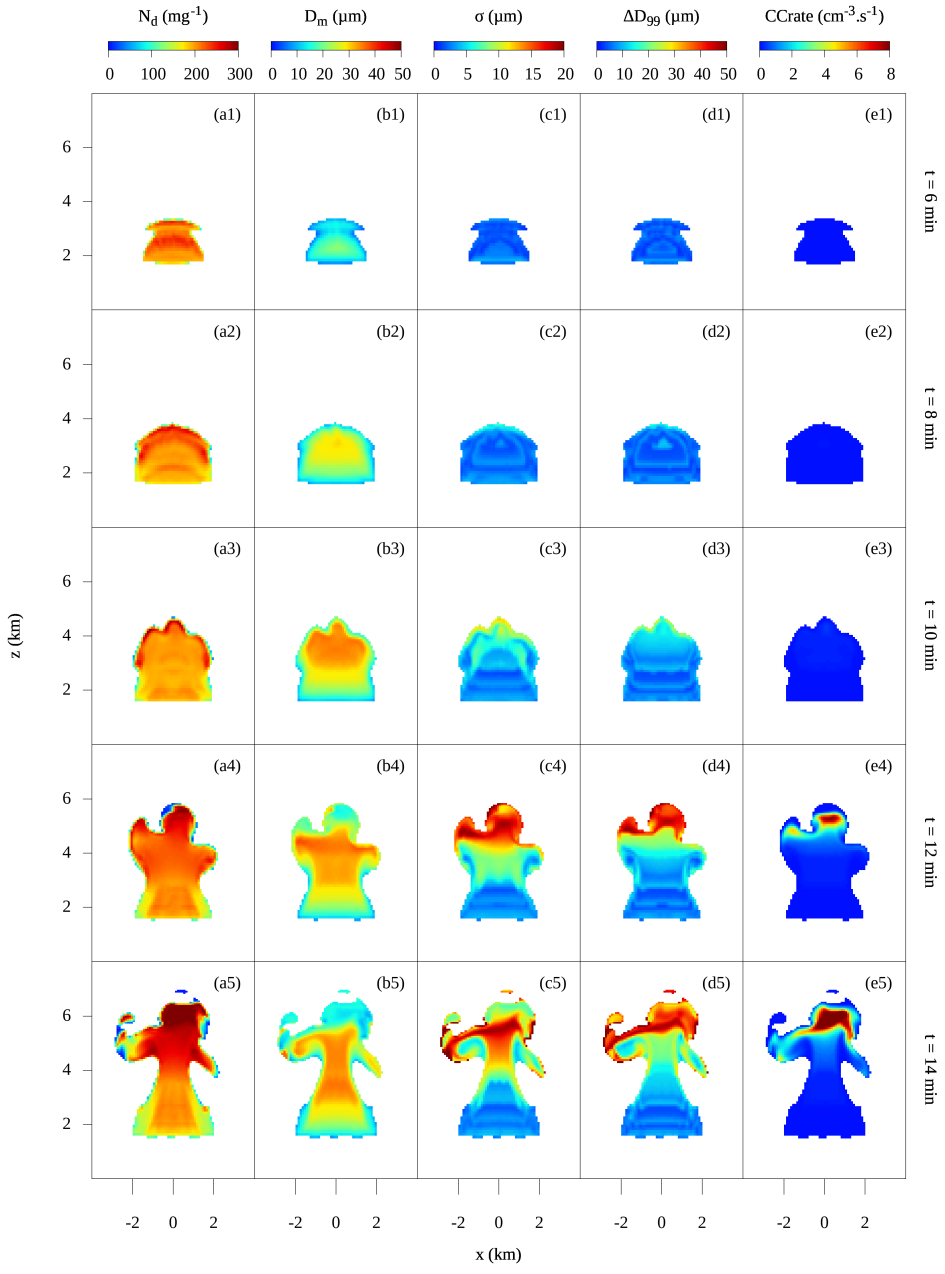

Overall, the values of N_d ($\sim 200 - 250$ mg^{-1}) and D_m ($\sim 10 - 30$ μm) (Figure 5.2) were reasonably consistent with the observations of clouds over the Amazon forest obtained during the same day of the sounding employed to initialize the model

(CECCHINI et al., 2017). However, relatively large values of N_d (> 250 mg^{-1}) as well as small values of D_m (< 20 μm) were found near the top of the modeled cloud, a feature that was accentuated at later times. Figure 5.3 shows that the more intense activation events were located near the boundaries of the cloud, especially near its top. Given that the aerosol number mixing-ratio represents an effective upper limit to N_d, the fact that cloud top values of N_d exceeded the aerosol number mixing-ratio are suggestive of numerical errors[3]; monotonicity is not preserved for integral quantities of the DSD when bin variables are advected individually even when using a monotonicity-preserving advection scheme (OVTCHINNIKOV; EASTER, 2009).

Figure 5.3 also shows that the activation rate increased in the upper part of the cloud core, especially after 10 min, coinciding with the onset of collision-coalescence (Figure 5.2). This occurred because collision-coalescence reduced N_d, which increased the phase relaxation timescale, resulting in an increase in the supersaturation particularly in the updraft core where there was strong vertical motion, consistent with Hall (1980). The decrease of N_d and consequent increase in supersaturation from collision-coalescence, such that N_d fell below the diagnosed number of activated CCN, led to activation of new droplets. This effect caused a strong reduction of D_m near cloud top. It also manifested in the maxima of σ and ΔD_{99} in the upper part of the cloud seen in Figure 5.2c,d; the DSDs were broadened toward smaller and larger sizes from activation and collision-coalescence, respectively. Large supersaturations in these regions of collision-coalescence and strong upward motion also led to large condensation growth rates (Figure 5.3c).

Figure 5.4 illustrates the cloud water mixing ratio and wind field for vertical cross-sections of the 3D simulation, as well as the analogous 2D simulation. The thermal-like structure of the updraft (LEVINE, 1959; TURNER, 1963) is seen in both the 3D and 2D simulations. A primary spherical vortex-like circulation ("toroidal circulation" hereafter) drove inflow near cloud base and outflow near cloud top, as well as the entrainment of environmental air through the lateral edges of the cloud, most evident at an altitude of approximately one-half the cloud depth (e.g., seen in Figure 5.4a3,b3 at approximately 3-4 km altitude). Secondary toroidal circulations that develop near cloud top (e.g., seen in Figure 5.4a3 at approximately 5.5 km altitude) also favored the intrusion of dry air into the cloud.

[3]Note that, while N_a is constant and equal to 200 cm^{-3} in these simulations, the aerosol number mixing-ratio (kg^{-1}) varies, mainly with height, according to variations in the density of the air.

Figure 5.3 - Vertical cross-sections of a) supersaturation (S), b) droplet activation rate (Act), and c) condensation/evaporation (Cond) growth rate for different times in the 3D simulation. The condensation rate expresses the rate of change of the mean droplet size due to condensation or evaporation. Each row represents a different simulation time, labeled to the right of the plots.

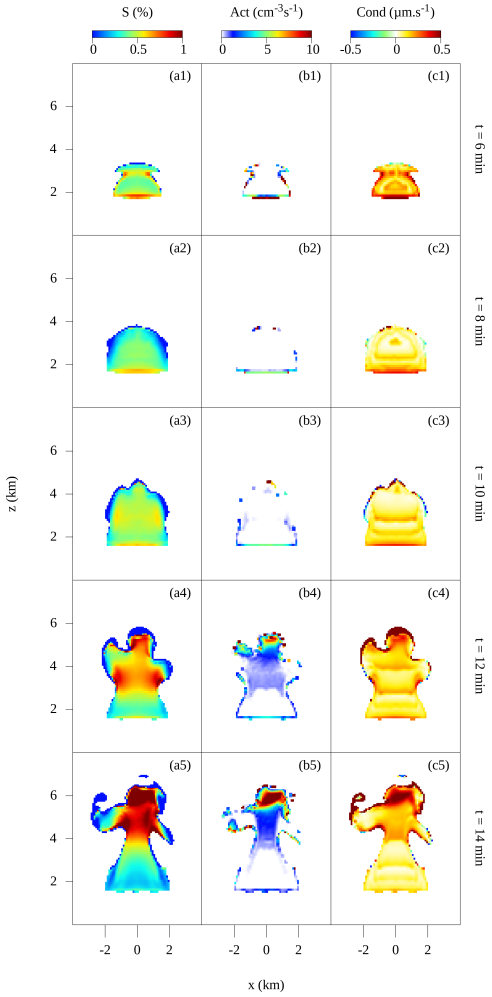

Here a distinction is made between *dilution* and *entrainment*. In this study, entrainment refers to the net flux of air across the cloud boundary into the cloud. This can lead to dilution of cloud properties, depending on the properties of the entrained air. However, because properties in the near-cloud environment are generally heterogeneous, there is usually not a 1 : 1 correspondence between entrainment and dilution (ROMPS, 2010). Moreover, dilution can occur as a diffusive exchange across the cloud boundary. This distinction is mainly a question of scale: organized entrainment is the net flux into the cloud across the cloud boundary over some defined scale (typically the grid spacing in explicit calculations of entrainment from model

simulations, e.g., Romps (2010), Dawe and Austin (2011)), whereas dilution from diffusive mixing is implicitly driven by motions smaller than this scale. In principle, organized detrainment, defined as the net flux of air across the cloud boundary into the environment, could also lead to apparent dilution if the detrained air has properties that are further from the environment that the in-cloud average. No distinction is made between the various mechanisms of dilution here, but it is noted that dilution is enhanced along the lateral cloud edges, especially at mid-cloud heights, from entrainment associated with the inward branch of the main toroidal circulation, and at cloud top from numerical and parameterized mixing.

Figure 5.4 - Vertical cross-sections of liquid water mixing ratio (q_l, color contours) and flow field (vectors). The blue and black continuous contours represent $N_d = 1$ mg^{-1} and $\theta_e = 350$ K, respectively. The left and right columns show results for the base 3D and 2D simulations, respectively. Different times are labeled in the plots.

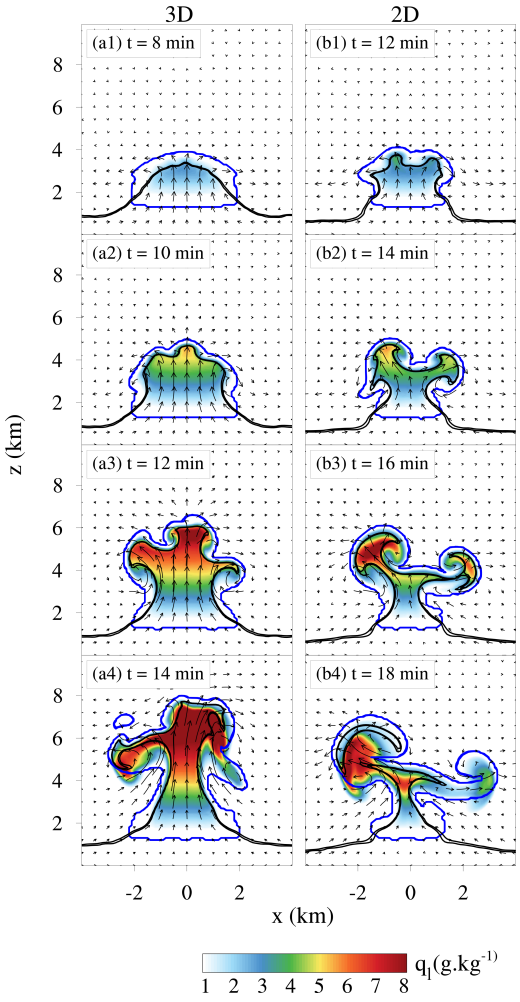

Because the equivalent potential temperature (θ_e) is conserved for moist adiabatic processes, it serves as a proxy for the degree of mixing with environmental air and dilution that cloud air parcels undergo as they rise from cloud base (i.e., smaller θ_e implies greater dilution because mid-tropospheric θ_e is smaller than θ_e at cloud base). The θ_e = 350-K isoline is represented by black contours in Figure 5.4. Note that changes in the area encompassed between the N_d = 1-mg^{-1} and θ_e = 350-K isolines in Figure 5.4 reflect the increase in cloud dilution with time. Dilution is discussed further in the context of an analysis of θ_e in Section 45.3.3.

Changes induced in the model dynamics by reducing the number of spatial dimensions from three to two led to some differences between the simulations. Firstly, as a consequence of its weaker updraft, the cloud developed later in 2D than in 3D. This is consistent with previous studies that compared the updraft strength in 2D and 3D simulations, for the same environmental and initial conditions (WILHELMSON, 1974; TAO et al., 1987; PHILLIPS; DONNER, 2006; ZENG et al., 2008). The studies of Morrison (2016a), Morrison (2016b) showed that differences in vertical velocity between 3D and 2D arise directly from the differences in the continuity equation for each geometry. Figure 5.4 also shows that, from the initial time of the cloud development, the toroidal circulation of the thermal was stronger in the 2D simulation and, consequently, the cloud appeared to entrain more than in 3D, as indicated by the shape of the cloud area encompassed by the θ_e = 350-K isoline. A stronger toroidal circulation in 2D than 3D is consistent with greater vertical pressure gradient forcing (MORRISON, 2016a; MORRISON, 2016b) and regions of divergence near cloud top and convergence near cloud base in 2D.

However, despite the dynamical differences between the 2D and 3D simulations, their cloud microphysical and macrophysical features were similar (Figure 5.5). The largest differences occurred in the position of the eddies and lobes near cloud top, but the DSD characteristics inside these cloud lobes were similar in 2D and 3D. Figure 5.6 shows the DSDs at different altitudes at the center of the domain (x_o) and 1 km to the left ($x_o - 1$ km), from the 2D and 3D simulations. DSD broadening with height is evident, including the development of bimodalities. Overall, the DSD evolution was similar in the 2D and 3D simulations. Note that because of differences in the location of the cloud lobes along the cloud top, the broadest DSDs were located at x_o in the 3D simulation, and in $x_o - 1$ km in the 2D simulation. Similarity between DSDs in the 3D and 2D simulations is further illustrated in Figure 5.7. It shows that the mean profiles of N_d, D_m, σ, ΔD_{99}, and CCrate, analyzed separately for high- and low-dilution cloud regions (separated by the 350-K θ_e isotherm), were similar in

2D and 3D. Differences in the depth of the cloud led to some quantitative differences between the 2D and 3D profiles, mainly toward cloud top, but this does not affect conclusions regarding the vertical distributions of the DSD characteristics.

Figure 5.5 - Similar to Figure 5.2, but for the base 3D simulation at $t = 12$ min (top row) and 2D simulation at $t = 16$ min (bottom row).

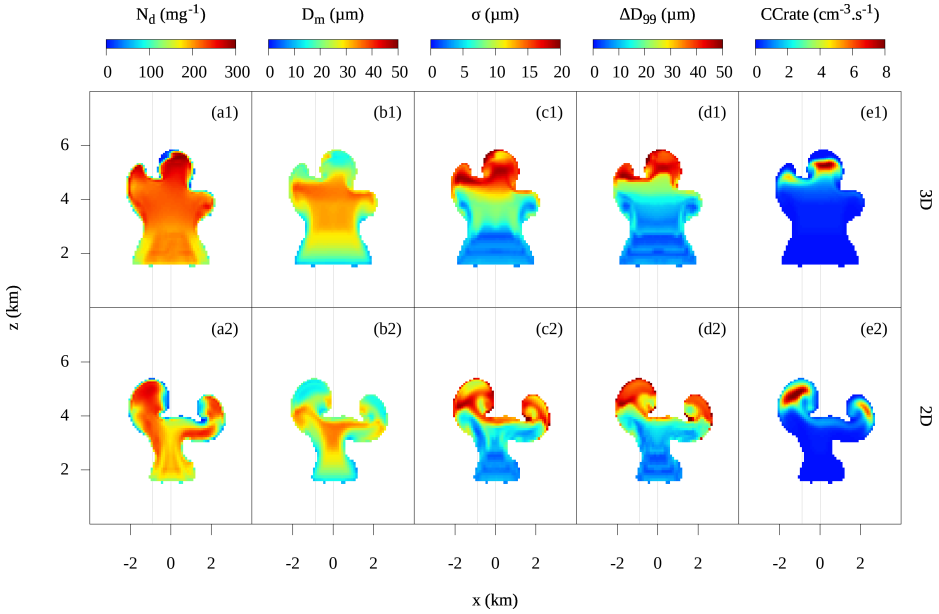

Figure 5.6 - Bin DSDs at different heights (colored lines) in the base 3D simulation at $t = 12$ min (top row) and 2D simulation at $t = 16$ min (bottom row). The left panels show DSDs at the cloud center (x_o, vertical solid lines in Figure 5.5). The right panels show DSDs 1 km to the "left" of center ($x_o - 1$ km, vertical dotted lines in Figure 5.5).

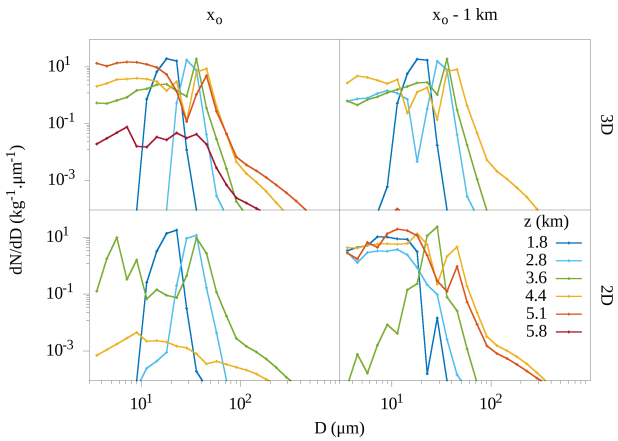

Figure 5.7 - Mean profiles of a) number mixing ratio (N_d), b) mean diameter (D_m), c) DSD standard deviation (σ), d) difference between the diameters of the 99^{th} and 50^{th} percentiles of the DSD (ΔD_{99}), and e) rate of collision-coalescence (CCrate), for $\theta_e > 350$ K (first row) and $\theta_e < 350$ K (second row) at $t = 12$ min in the base 3D simulation (blue lines) and $t = 16$ min in the 2D simulation (red lines).

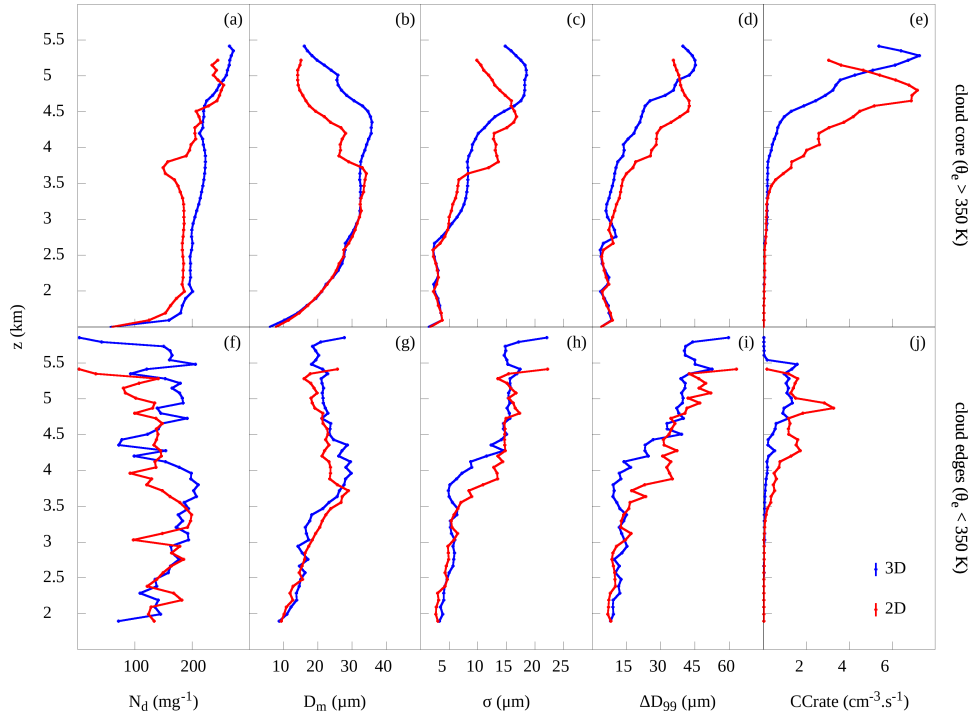

Given the qualitative consistency between the results obtained with the 3D and 2D configurations of the model, specifically those regarding the microphysical characteristics of the cloud, the latter is employed to explore mechanisms of DSD broadening in the WRF-TAU framework here. Being computationally cheaper and easier to analyze and interpret results, the 2D configuration was used to perform numerous sensitivity tests varying the resolution and turning off the representation of various physical processes that affected the DSDs. Having fewer degrees of freedom, 2D simulations can respond differently to a given change in the model configuration or forcing than 3D simulations. For instance, Wang and Sobel (2011) found that precipitation increased more rapidly in 2D than in 3D as sea surface temperature increased. However, the sensitivities are expected to have the correct sign, although their magnitude might be somewhat different in 2D than 3D.

5.3 Role of DSD broadening mechanisms at different model resolutions

In this section, the role of different mechanisms in broadening the DSDs at two different grid resolutions in the 2D version of the model is analyzed. There are several potentially important processes for DSD evolution in the simulations. These include collision-coalescence, sedimentation, evaporation, resolved "turbulent-like" transport[4], and in-cloud droplet activation. Different sensitivity tests including or neglecting the effects of these processes are analyzed. Table 5.1 summarizes the sensitivity tests discussed in this section. Note that here "in-cloud droplet activation" refers specifically to the activation that occurs above either the cloud base or the 2000-m altitude model level. For each time step and each point in the horizontal grid, the cloud base was defined as a 120-m layer starting at the first model level, from bottom to top, where activation occurs (provided that its altitude does not exceed 2000 m).

In all of the simulations, transport and mixing of model fields occurred by resolved (grid-scale) transport and parameterized sub-grid scale mixing, with contributions from numerical mixing associated with the advection calculations. However, the resolved flow was much more turbulent in the TURB and CTRL cases, in which random initial θ perturbations were applied, than in other simulations. Therefore, the effects of resolved turbulent transport on DSD evolution are studied by comparing simulations with and without θ perturbations, keeping in mind that the resolved flow also affects the subgrid mixing directly by impacting spatial gradients of model fields. Here, "effects of turbulence" refers specifically to the effects via resolved turbulent transport and mixing of model fields, not considering the effects of turbulence on collision-coalescence, small-scale fluctuations of supersaturation, droplet clustering, etc. For simplicity, the simulations without initial random θ perturbations are referred as "laminar". In effect, the spinup of turbulent motion in the laminar simulations was greatly delayed so that the flow remained quasi-laminar over the entire simulation time (in principle, *any* flow asymmetries or noise, even at the level of machine roundoff, would eventually spin up turbulent-like motion if the simulations were run long enough).

Differences in the resolved supersaturation among simulations with different grid spacings can affect the weight of condensate, and hence the buoyancy and vertical velocity, which, in turn, feeds back on the supersaturation and amount of condensate.

[4]Because these simulations are 2D, "turbulent-like" may be a more appropriate way to describe the smaller-scale eddies in them; 3D turbulence of course has notably different properties from 2D. However, hereafter these motions are called "turbulence" for brevity.

Table 5.1 - Summary of the cases designed to analyze the roles of the broadening mechanisms in the model. For each case, the inclusion of collision-coalescence (Coll-coal), sedimentation (Sed), turbulent-like resolved flow (Turb), evaporation (Evap), in-cloud activation (Act) and the fixed-N_d assumption ($N_d = C$) is indicated by a check mark (✓) in the corresponding column.

Name	Coll-coal	Sed	Turb	Evap	Act	$N_d = C$
CTRL	✓	✓	✓	✓	✓	-
CCS	✓	✓	-	-	✓	-
TURB	-	-	✓	-	✓	-
EVAP	-	-	-	✓	✓	-
ACT	-	-	-	-	✓	-
CBACT	-	-	-	-	-	-
ND100	-	-	-	-	-	✓

To limit differences caused by this effect, the weight of condensate was neglected in the calculation of buoyancy for the tests shown in this section. Neglecting the weight of the condensate is particularly useful to keep a dynamical consistency between the varying-N_d and the fixed-N_d tests (ND100 in Table 5.1). Although there remained some cloud structure and dynamical differences among the simulations, particularly when the model grid spacing was altered, these differences were generally small. The "piggybacking" methodology (GRABOWSKI, 2014; GRABOWSKI, 2015; GRABOWSKI; MORRISON, 2016) could be used to separate the impacts of dynamical and microphysical changes clearly[5], but such an effort is left to future work.

Figure 5.8 shows the microphysical properties of the cloud at $t = 16$ min for the 100×100 and 30×30 simulations, where all the processes mentioned in Table 5.1 were considered (CTRL simulations). This configuration is similar to those discussed in the previous section except that the weight of the droplets was neglected in the buoyancy calculation here. This had the effect of increasing the vertical velocity and increasing the physical size of the cloud.

Decreasing the grid spacing, in the CTRL simulations, allowed the model to better represent the fine-scale structure of the cloud, especially the sub-cloud-scale turbulent-like eddies. However, there was generally little impact on the cloud micro-

[5]The "piggybacking" method applies two (or more) different sets of cloud and thermodynamic variables associated with different model configurations, typically different microphysics schemes or different settings within a scheme. One set is fully coupled to the model dynamics and drives the flow, while the other set is driven by the same flow but does not feed back to it. This allows testing the impact of model changes using the same modeled flow field.

physical and DSD structure overall, seen by comparing the top and bottom panels in Figure 5.8, with one important exception: both σ and ΔD_{99} were significantly smaller in the high-resolution simulation compared to the low-resolution simulation below $\sim$ 2.5 km. This region was less affected by entrainment, evaporation, and collision-coalescence. As it is shown later in this chapter, that feature was seen in all simulations and was mainly associated with changes in vertical rather than horizontal model grid spacing. Narrowing of the DSDs with decreasing vertical grid spacing is discussed in detail in Section 45.3.4.

Figure 5.8 - Vertical cross-sections of a) number mixing ratio (N_d), b) mean diameter (D_m), c) DSD standard deviation (σ), d) difference between the diameters of the 99^{th} and 50^{th} percentiles of the DSD (ΔD_{99}), and e) collision-coalescence rate (CCrate) for the low-resolution 100×100 simulation (top row) and high-resolution 30×30 (bottom row) simulations for the CTRL case, at time $t =$ 16 min.

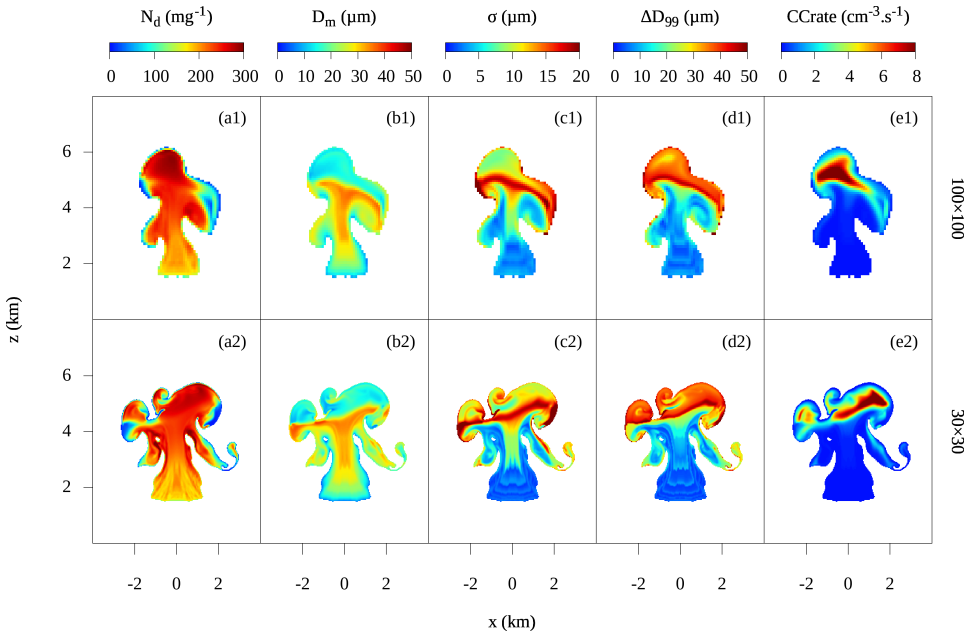

5.3.1 Effects of collision-coalescence, evaporation, and turbulent transport

Collision-coalescence played a dominant role in the evolution of the DSDs in the simulations. This was demonstrated by the CCS test, in which collision-coalescence and sedimentation were included but evaporation was neglected and the flow was laminar (note that additional simulations indicated little impact from also turning

off sedimentation). Figure 5.9 shows vertical cross-sections of model fields from the CCS simulations at high and low model resolutions, in the same format as Figure 5.8. With laminar flow, the cloud was nearly symmetric, especially at the lower resolution. Otherwise note the similarity between the distribution of DSD parameters in the CCS simulations and that in the CTRL case. Like in CTRL, the CCS simulations reproduced the mechanism of in-cloud droplet activation induced by the reduction in N_d from collision-coalescence discussed above. This led to a strong reduction in D_m and to an increase in N_d and ΔD_{99} near cloud top similar to CTRL. Interestingly, the largest values of σ were found at the boundary between the regions containing larger and smaller D_m values, respectively, suggesting the role of mixing in broadening the DSDs in the model (an aspect discussed in detail in Section 45.3.3). Similar to CTRL, increasing the model resolution for the CCS simulation did not have any major influence on the characteristics of the simulated DSDs other than better resolving small-scale details in the microphysical and macrophysical cloud structure and the narrowing of DSDs below 2.5 to 3 km with higher resolution.

Figure 5.9 - Similar to Figure 5.8, but for the CCS simulations.

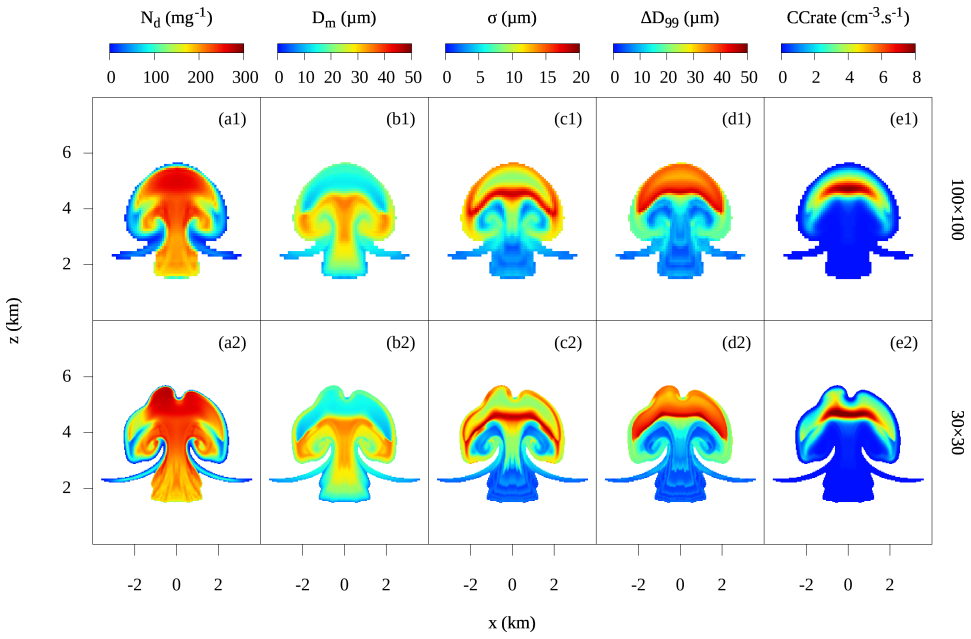

Consistent with the conclusion from the CCS simulation regarding the dominant role of collision-coalescence on DSD evolution, turning off collision-coalescence led to large changes in the cloud microphysical structure. In the TURB test, which neglected collision-coalescence, sedimentation and evaporation but had a turbulent-

like flow, in-cloud activation was greatly reduced compared to CCS and CTRL. Thus, the broad region of small D_m, large σ, and $\Delta D_{99} > 30$ μm in the upper part of the cloud from collision-coalescence and its inducement of droplet activation in CCS and CTRL did not occur in TURB (compare Figure 5.10 with Figure 5.8). Instead, the largest values of ΔD_{99} were located at the interface between relatively undilute cloudy air and the entrained air associated with the circulation of turbulent eddies near cloud top (Figure 5.10d). Values of ΔD_{99} were generally greater than 10 μm in the upper part of the cloud, where smaller resolved eddies contributed to mixing. This contrasted with the laminar simulations described below that had much smaller values of ΔD_{99} in the upper cloud region. Correspondingly, the largest diagnosed collision-coalescence rates were in eddies near cloud top in TURB, but occurred lower down in the cloud core in the other simulations with laminar flow.

Figure 5.10 - Similar to Figure 5.8, but for the TURB simulations. CCrate here constitutes a diagnosed rate because collision-coalescence is turned off in these simulations.

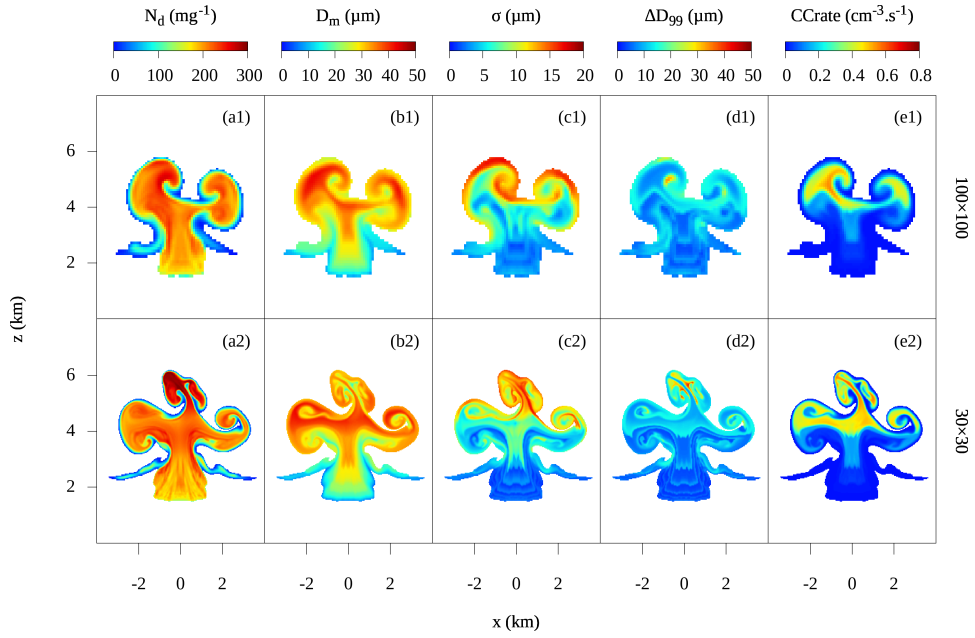

The largest values of σ in TURB were located along the cloud boundary near cloud top (Figure 5.10c), associated with relatively large N_d values. This suggests, indirectly, the role of droplet activation in broadening DSDs at cloud top. Although resolved turbulent motion enhanced this feature, it was also seen in the laminar simulations described below. This was evidently caused by cloud dilution that re-

duced N_d and thereby promoted in-cloud droplet activation in ascending air along the cloud top (similar to the inducement of droplet activation from the reduction of N_d by collision-coalescence discussed above). It should be emphasized that cloud "dilution" here (and in the rest of the paper) specifically refers to the mixing of cloudy and cloud-free air without necessarily involving evaporation. When evaporation is turned off, this is analogous to extremely inhomogeneous mixing, whereby N_d is reduced but the DSD mean size and shape are unaffected (in contrast to homogeneous mixing, in which N_d remains constant but droplet size decreases from evaporation).

Note that dilution can also broaden DSDs by generating spatial heterogeneity in the supersaturation field and condensational growth rates followed by in-cloud mixing of DSDs with different growth histories, similar to the "eddy hopping" mechanism. However, based on simulations described later in Section 45.3.2 that excluded droplet activation above cloud base, the effects of droplet activation seemed to dominate over those from this mixing mechanism in driving the local maximum of σ at the cloud top. This is in contrast to the lateral cloud edges, where this "eddy hopping" mechanism appeared to be more important (detailed in Section 45.3.2).

Also note that droplet activation along the cloud top may be augmented by the generation of high supersaturation from separately advecting temperature and water vapor, which can produce large supersaturation values along cloud edges because of the nonlinear relationship between temperature and saturation mixing ratio (STEVENS et al., 1996b; GRABOWSKI; MORRISON, 2008), with contributions from evaporation as the cloud edge advects into non-cloudy grid cells depending on the ratio of the phase relaxation and advective timescales (HOFFMANN, 2016). However, sharp peaks in supersaturation right at cloud top were not evident in the supersaturation field (similar to results from the 3D simulation seen in Figure 5.3a), outside of a few isolated grid points; thus, the generation of spuriously high supersaturation from this mechanism appeared to be relatively unimportant here.

Figure 5.11 illustrates results from the EVAP simulations, which have laminar flow and neglect collision-coalescence, and sedimentation but included evaporation. The largest values of σ (> 12 μm) and ΔD_{99} (> 30 μm) were primarily restricted to the cloud top. The structure of σ was similar to that in TURB, and as it is shown later, also similar to tests of the same configuration except with evaporation turned off. As discussed above, the peak in σ along the cloud top was evidently related to droplet activation that was induced by the reduction of N_d from dilution. Thus, the

effects of evaporation on the DSD width appeared to be small. Limited sensitivity to evaporation was broadly consistent with an analysis of evaporation rates from the 3D simulation in Figure 5.3, which showed that the vast majority of cloudy points underwent condensation, with only a few points right along the cloud edge experiencing evaporation (mainly at points along the cloud top and lower down associated with the toroidal circulation). Like in the previous cases, increasing the model resolution in the EVAP simulations better resolved the cloud structure, although the impact on the cloud microphysical structure was limited above 2.5 to 3 km.

Figure 5.11 - Similar to Figure 5.10, but for the EVAP simulations.

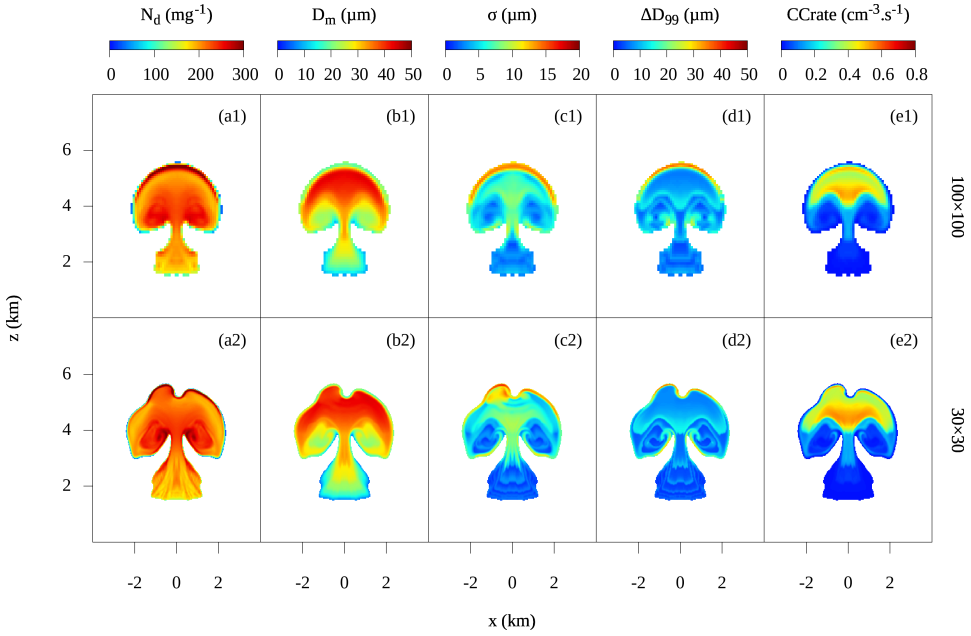

To briefly summarize, these sensitivity tests suggest that the representation of collision-coalescence had a major impact on the evolution of the DSDs, which is not surprising given the strongly nonlinear drop growth by collision-coalescence once drops grow large enough for significant collision-coalescence to occur. Note, however, that the effects of collision-coalescence on DSD width were augmented by in-cloud droplet activation that occurred in strong upward motion when collision-coalescence reduced N_d below the diagnosed number of activated CCN. Because the model did not explicitly track aerosols inside clouds and instead assumed that the concentration of unactivated aerosols was equal to that of the background aerosols minus the existing droplet concentration following Equation 5.1, this effect might

have been overemphasized. Note that the diagnosed CCrate in the TURB and EVAP simulations, with collision-coalescence turned off, was about 10 times smaller than the CCrate from the simulations including collision-coalescence (CTRL and CCS). This reflects the smaller mean drop sizes and much narrower DSDs in the former two cases. However, because collision-coalescence is significant only after the DSDs reach a sufficient mean size and spread, it is important to understand mechanisms responsible for DSD broadening prior to the occurrence of significant collision-coalescence.

5.3.2 Effects of droplet activation

Here, two additional cases designed to better understand the role of droplet activation on DSD broadening are considered. In the first case, the original activation scheme was employed (ACT case) and, in the second case, droplet activation was allowed only inside a layer of 120-m depth at cloud base (CBACT case). For each model column, the cloud base was assumed to be located at the first level, from bottom to top, where activation occurred (provided that its altitude did not exceed 2000 m). In all simulations described below collision-coalescence, sedimentation, and evaporation were turned off, and the flow was laminar.

In cumulus clouds, the supersaturation can increase with height above cloud base, if generation of supersaturation from cooling by adiabatic expansion in updrafts exceeds the sink from condensation on growing droplets (KHAIN et al., 2000; LEBO et al., 2012). However, in reality, aerosol scavenging should limit droplet activation above cloud base, at least to some extent. Aerosol scavenging inside clouds can be compensated by entrainment, but this depends on fractional entrainment rates and how the background N_a varies with height. The activation approaches in the ACT and CBACT simulations can be considered approximately as the upper and lower bounds, respectively, of the activation in real clouds.

Figure 5.12 shows that in the ACT simulations, in which neither collision-coalescence, sedimentation, evaporation nor resolved turbulence were considered, D_m increased nearly monotonically with height and the cloud-top peak of N_d was remarkably diminished compared to CTRL and CCS, which both included collision-coalescence. This is true to an even greater extent for CBACT (Figure 5.13) compared to CTRL and CCS. The fields of both D_m and N_d were also smoother and more uniform in ACT and especially CBACT. By turning off collision-coalescence, the source for large drops was limited. In-cloud activation was also suppressed when collision-coalescence was turned off, as discussed in the previous section, limiting the generation of small droplets in ACT (especially in the cloud core). In CBACT,

droplet activation was simply turned off above cloud base. With the sources of both large and small drops limited (or turned off) above cloud base in ACT and CBACT, the DSDs in the upper part of the cloud core were narrower than in CTRL (i.e., smaller σ and ΔD_{99}); compare Figures 5.12, 5.13c,d and 5.8c,d. The lack of a tail at large sizes and the weaker small mode of the DSDs are also seen when the DSDs in ACT and CBACT (Figures 5.14,5.15) are compared to those from CTRL (Figure 5.6).

Figure 5.12 - Similar to Figure 5.8, but for the ACT case, and with two extra rows for the simulations with high vertical- (30×100) and high horizontal resolution (100×30). CCrate here constitutes a diagnosed rate because collision-coalescence is turned off in these simulations.

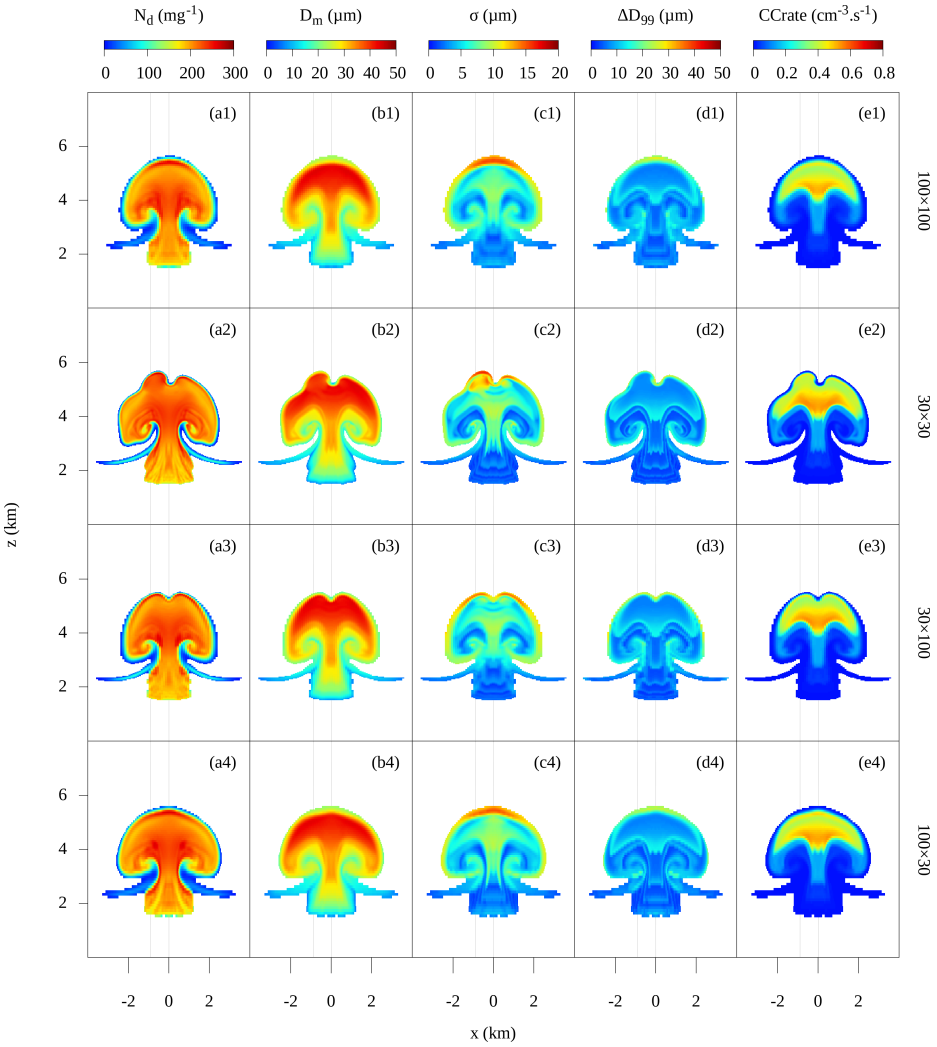

Also note that the upper part of the cloud core in ACT had ΔD_{99} values about one-half as large as those in TURB, with the peak collision-coalescence rate shifted downward relative to cloud top (compare Figures 5.12d,e and 5.10c). This finding supports the earlier discussion on the role of turbulent motion in broadening DSDs near cloud top, since the only difference between TURB and ACT is that resolved flow was turbulent in the former and laminar in the latter.

Figure 5.13 - As in Figure 5.12, except for the CBACT simulations.

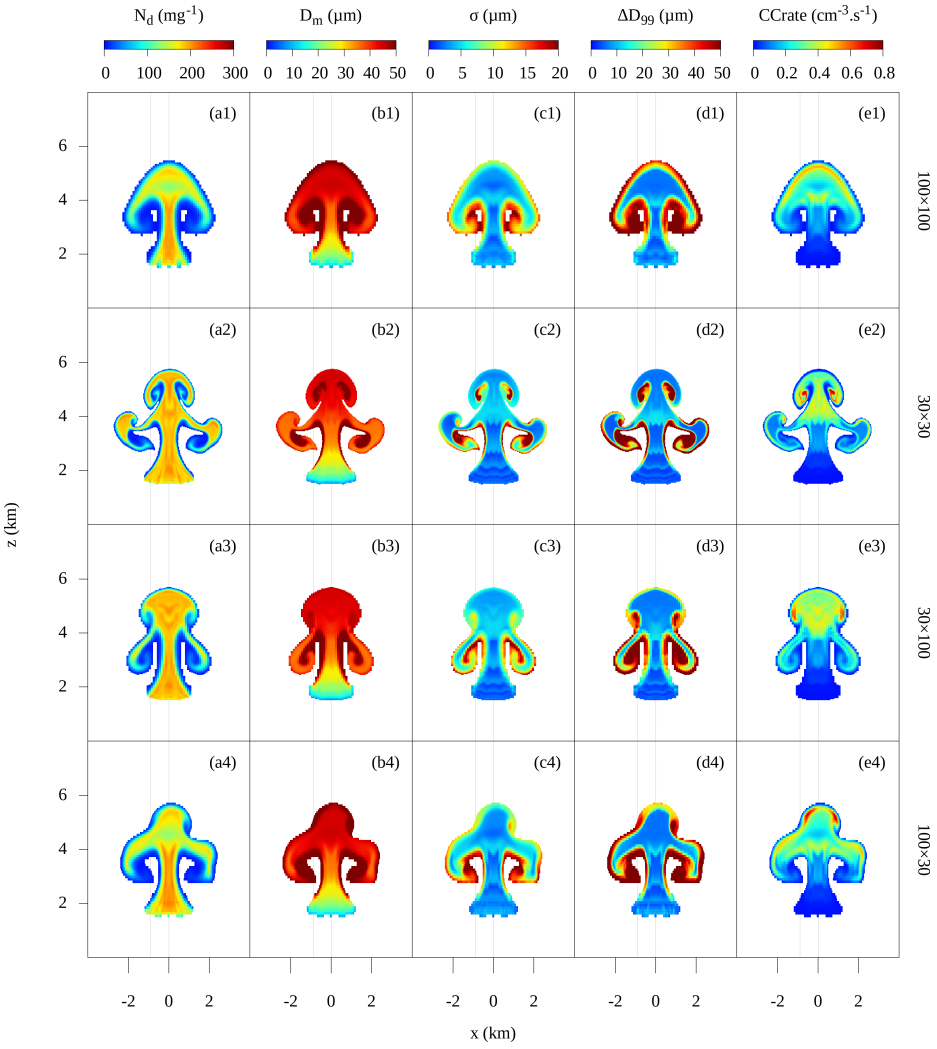

There are several major differences in DSD characteristics between ACT and CBACT, further highlighting the important role of droplet activation above cloud base. Much higher supersaturations occurred in CBACT (supersaturation near the lateral cloud edge reached $\sim$ 30%, not shown, similar to values reported by Lebo

et al. (2012)), leading to mean droplet sizes that were 2-3 times larger compared to ACT near the cloud edges. However, in the cloud core, σ was greater in ACT than CBACT by up to about a factor of 2. These results suggest that in-cloud droplet activation is important for broadening DSDs in the cloud core even when activation is not enhanced by the reduction of N_d from collision-coalescence. It is also seen that many areas of relatively large σ in the cloud core in ACT (Figure 5.12) associated with in-cloud droplet activation had relatively small ΔD_{99} (< 10 μm), consistent with the idea that droplet activation broadens DSDs to small sizes but has a weaker influence on the large drop tail.

While the DSDs were generally narrower (smaller σ) in CBACT than ACT, there was still substantial DSD broadening in CBACT, especially along the cloud edges (Figure 5.13). This broadening could only occur from entrainment and mixing processes in conjunction with condensation because all other broadening mechanisms were turned off in CBACT. Interestingly, the DSDs were actually much broader along the *lateral* cloud edges in CBACT ($\sigma > 12$ μm and $\Delta D_{99} > 35$ μm) than in ACT, indicating that droplet activation limited DSD broadening there in contrast to its influence on DSDs in the cloud core and along the cloud top. Evidently, this occurred because activation of droplets limited the effects of dilution in reducing N_d locally. In ACT, there was a region of relatively large N_d and small D_m along the lateral cloud edges at mid-levels (approximately 2 to 4 km altitude), whereas the opposite occurred in CBACT.

The results for the lateral cloud edges described above contrast with the situation along cloud top; in ACT, there were sharp maxima in σ and ΔD_{99} along the cloud top for all model resolutions tested (Figure 5.12c,d). Whereas in CBACT, there were either weak local maxima in σ and ΔD_{99} at cloud top in the lower-resolution simulations (first, third, and fourth rows in Figure 5.13) or no apparent maxima at all at cloud top in the 30×30 simulation (second row from the top in Figure 5.13). This result again indicates the important role of droplet activation along the cloud top in broadening the modeled DSDs.

The diagnosed CCrate was generally smaller in CBACT than ACT (Figure 5.12e)-5.13e), consistent with smaller N_d, σ, and ΔD_{99} in the cloud core without any in-cloud activation. Nonetheless, there were some small, isolated regions of higher CCrate near the cloud edges in CBACT compared to ACT, reflecting the relatively broad DSDs there compared to those in ACT.

The results discussed above are further supported by comparing DSDs from selected

locations inside the cloud at $t = 16$ min from ACT (Figure 5.14) and CBACT (Figure 5.15). It is seen that the DSDs were narrower in the cloud interior (left panels in the figures) for CBACT than ACT because of the absence of a tail to small sizes in the absence of in-cloud droplet activation. In contrast, DSDs were fairly wide in CBACT near the cloud edge (right panels in the figures) with a shoulder of the DSDs extending to large sizes; significant concentrations of droplets exceeded a diameter of 100 μm. This DSD shoulder extending to large droplet sizes was absent in ACT. These DSD results were consistent with stronger condensational growth of droplets associated with much higher supersaturations along the lateral cloud edges in CBACT (not shown).

Figure 5.14 - As in Figure 5.6, except for the bin DSDs at different altitudes at $t = 16$ min in the 100×100 simulation for the ACT simulations.

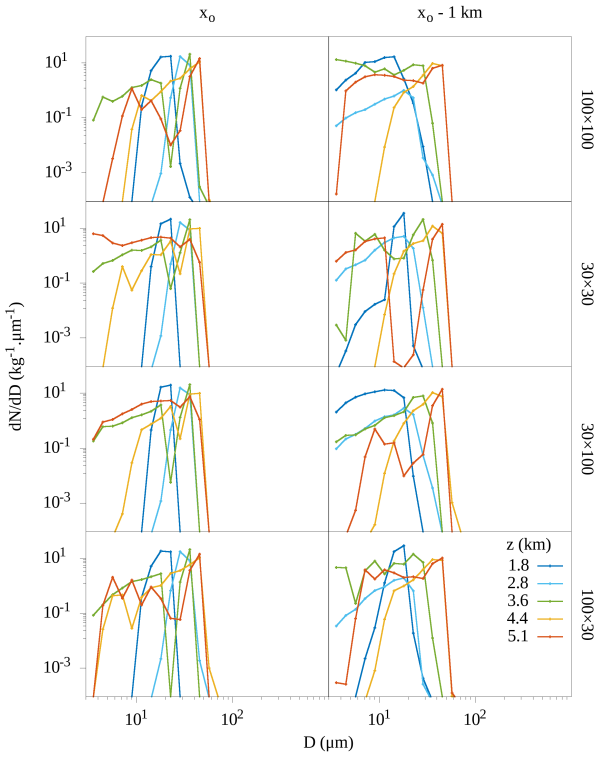

Varying the resolution in CBACT induced some differences in the dynamics of the cloud. Notable is the second thermal and associated toroidal circulation region that developed around 5 km altitude at 30×30 grid spacing, leading to enhanced entrainment in this region. This second thermal-like feature is clearly seen in the microphysical fields in the 2^{nd} and 4^{th} rows of Figure 5.13.

Figure 5.15 - As in Figure 5.14, except for the CBACT simulations.

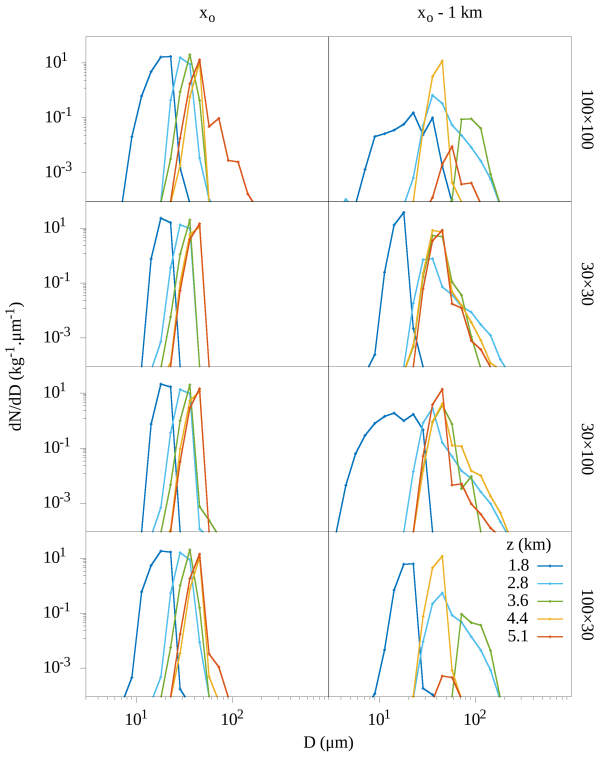

The role of varying the model grid spacing (vertical×horizontal), in terms of the horizontally averaged (in-cloud) profiles of D_m, σ, and ΔD_{99} for both the ACT and the CBACT simulations, is further highlighted in Figures 5.16 and 5.17 for $t = 7$ and 16 min, respectively. Results show that the horizontally averaged D_m was mostly insensitive to the model resolution when the grid spacing was reduced from 100×100 to 30×30. In general, both the ACT and CBACT simulations produced narrower DSDs (smaller σ and ΔD_{99}) with a decrease in *vertical* grid spacing at $t = 7$ min (Figure 5.16), although the impact of changing grid spacing was somewhat smaller and less robust (i.e., more variable with height) in ACT than CBACT. There was much less sensitivity to changes in *horizontal* grid spacing. This picture is less clear at $t = 16$ min (Figure 5.17). In regions of enhanced entrainment associated with inflow from the cloud's toroidal circulation around 3 km altitude (and also 5 km altitude in the 30×30 simulation with the secondary circulation), the higher-resolution simulations had wider DSDs, whereas elsewhere they were generally narrower. At $t = 7$ min, the cloud was still very shallow, especially in the CBACT simulations, and entrainment and dilution were limited before the development of a coherent toroidal circulation. At $t = 16$ min, on the other hand, the cloud was three times

deeper and well-developed toroidal circulations were evident (similar to those seen in Figure 5.4). This enhanced the inflow of environmental air into the cloud (i.e., entrainment), especially at mid-levels, in turn augmenting DSD broadening from dilution followed by in-cloud mixing. This mechanism is analyzed in more detail below.

Figure 5.16 - Mean profiles of a,d) droplet mean diameter (D_m), b,e) standard deviation of the DSD (σ), and c,f) difference between the diameters of the 99^{th} and 50^{th} percentiles of the DSD (ΔD_{99}) for different model resolutions (colored lines labeled at the bottom of the figure) in the ACT and CBACT simulations at $t = 7$ min.

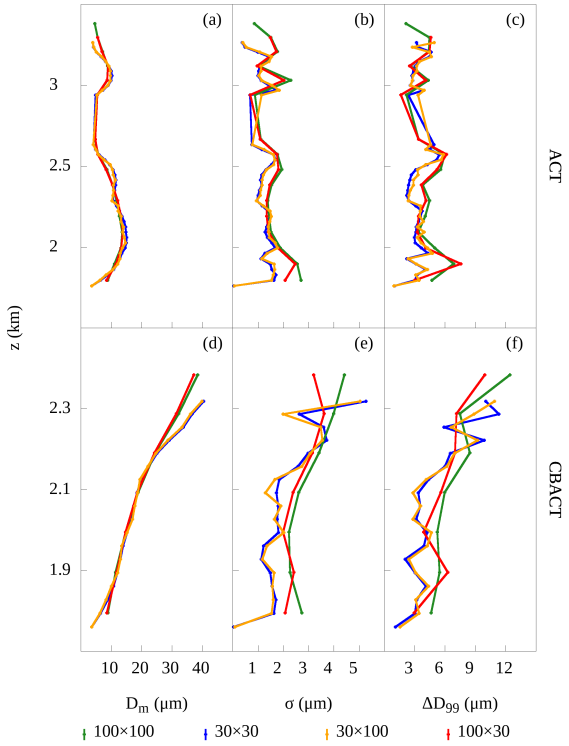

Figure 5.17 - Similar to Figure 5.16, but for $t = 16$ min.

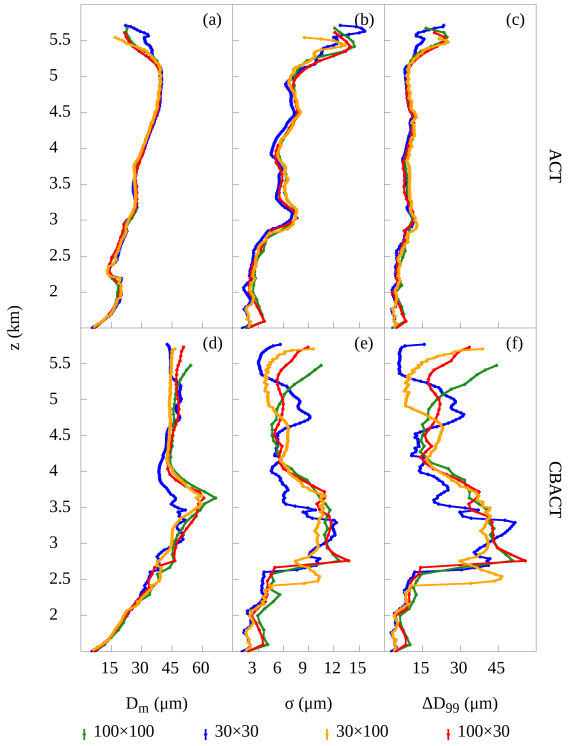

5.3.3 The role of cloud dilution

Relationships between entrainment, dilution, and DSD characteristics are further examined through scatterplots and histograms of θ_e, N_d, σ, and ΔD_{99}. As shown by the histograms in Figure 5.18b,h, in the ACT simulations, the points with high (low) N_d occurred more (less) frequently in the high-resolution (30×30) than low-resolution (100×100) simulations. In other words, when the resolution was increased, there was a shift toward slightly larger values of N_d. However, as illustrated by the scatterplots in the right columns of Figure 5.18, the relationship between ΔD_{99} and N_d was rather weak at both resolutions. On the other hand, except for a cluster of points with nearly monodisperse DSDs at $\theta_e \sim 345$ K, σ generally increased with N_d at a given θ_e value. This is consistent with the effects of in-cloud droplet activation, which broadens the DSDs toward small sizes, increasing σ but having less influence on ΔD_{99}. What, then, drives the variability in ΔD_{99}? The answer resides in the degree of cloud dilution.

Figure 5.18 - Histograms of equivalent potential temperature (θ_e) (a,g) and droplet number mixing ratio (N_d) (b,h) as well as scatterplots of the standard deviation of the DSD (σ) (d,f,j,l) and the difference between the diameters of the 99^{th} and 50^{th} percentiles of the DSD (ΔD_{99}) (c,e,i,k) in the space of N_d versus θ_e, at $t = 7$ min (upper plots) and $t = 16$ min (lower plots) in the ACT simulations. The scatterplots in (c,d,i,j) and (e,f,k,l) correspond to the lower-resolution and higher-resolution simulations, respectively, as labeled in the plots. In the scatterplots of the high-resolution simulation, only one out of every three points is shown to facilitate the visualization.

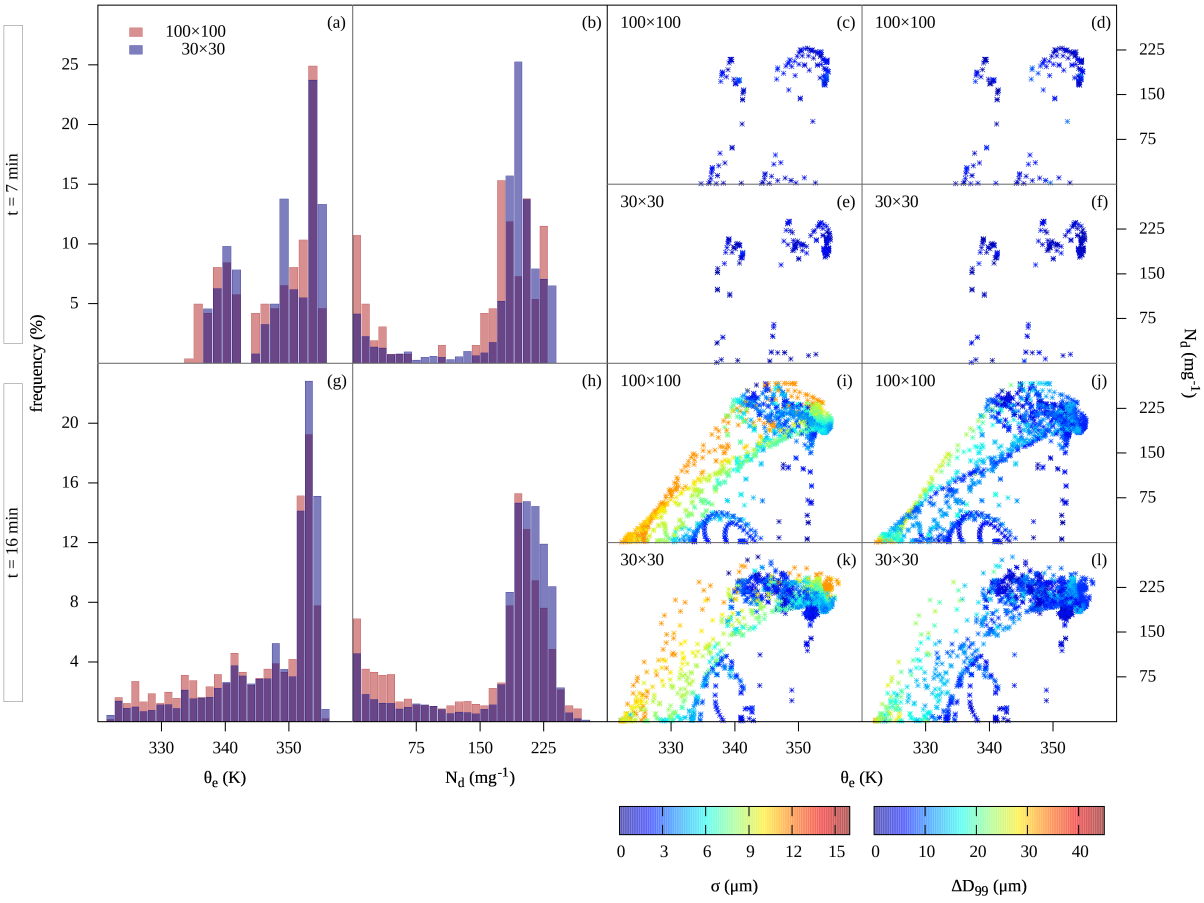

At $t = 16$ min in Figure 5.18, ΔD_{99} had a reasonably strong negative correlation with θ_e, which is consider as a proxy for the degree of dilution of the cloudy air here. Thus, the DSDs with the broadest tails tended to occur at points that were more dilute (i.e., those with lower θ_e). This provides more evidence for the role of dilution in DSD broadening. A negative correlation between σ and θ_e was also evident when $N_d <\sim 150$ mg^{-1}, consistent with DSD broadening from dilution. When the model resolution was increased, there was a small shift in the θ_e distribution toward higher values

(Figure 5.18a,g). This was likely related to better resolving fine-scale structures near the cloud edge, thereby slightly reducing cloud dilution. This led to higher N_d values, as seen in Figure 5.18b,h, although the reduction in N_d from dilution was counterbalanced by activation of droplets in entrained air in the ACT test. Again, the overall impact of model resolution on N_d was small.

Figure 5.19 - Similar to Figure 5.18, but for the CBACT simulations.

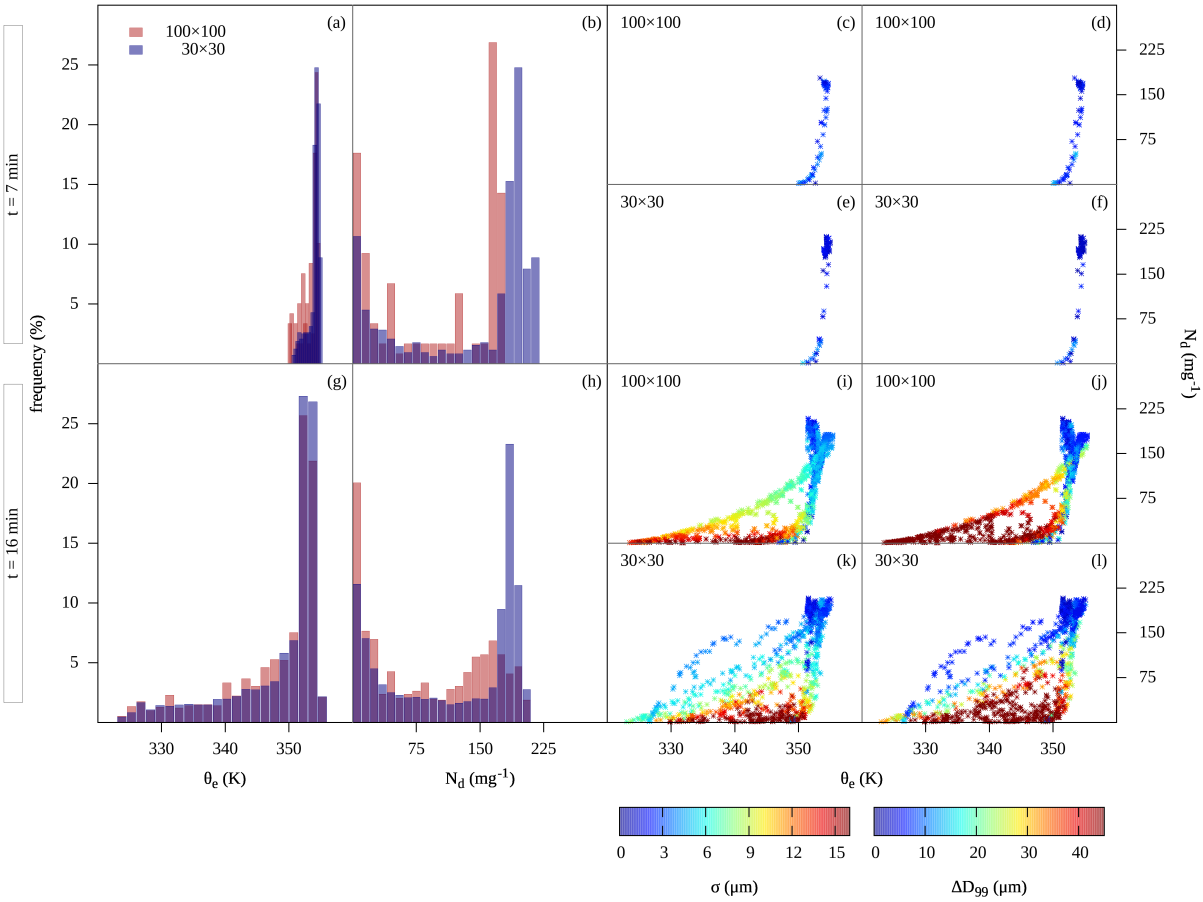

Without in-cloud droplet activation, in CBACT, there were clear decreases in σ and ΔD_{99} with increases in N_d (Figure 5.19i-l). Larger σ and ΔD_{99} also tended to occur at points with lower θ_e, again highlighting the role of cloud dilution in DSD broadening. However, this relationship was less evident in the high-resolution simulation, plausibly because of greater spatial variability and delayed in-cloud mixing at high resolution. For example, small-scale entrainment in the high-resolution simulation

could have led to points with low θ_e but relatively small ΔD_{99} prior to in-cloud mixing. There was again a shift toward higher θ_e values at higher model resolution in CBACT (Figure 5.19a,g), similar to ACT, while there was a stronger shift toward higher values of N_d at higher resolution (Figure 5.19b,h) associated with the reduced dilution. The difference in N_d between the low- and high-resolution simulations in CBACT was larger than in ACT because there was no droplet activation above cloud base in CBACT to compensate for the reduction in N_d from dilution.

Overall, these results show that the greatest DSD broadening and widest DSDs tended to occur in both the ACT and CBACT cases in cloud regions that experienced more entrainment and mixing with the environment and hence greater dilution, especially at low model resolution. However, this relationship was strongly modulated by droplet activation. Thus, the variations of N_d in the ACT and CBACT simulations were determined by two competing processes: activation and dilution. Note that dilution (in the absence of evaporation) itself does not affect the DSD shape; it acts indirectly by creating the conditions for subsequent DSD broadening. Specifically, dilution reduces N_d, which results in locally increased supersaturations and droplet condensational growth rates when this diluted air rises within the updraft. DSD broadening ensues when this air is mixed with less dilute cloud core air containing droplets that experienced lower supersaturation and slower growth. This broadening mechanism from dilution and in-cloud mixing is similar to "eddy hopping" (COOPER, 1989; GRABOWSKI; ABADE, 2017; ABADE et al., 2018), with broadening from the mixing of DSDs that have different growth histories. This process is greatly amplified by the toroidal circulation, which leads to inflowing air that enhances entrainment and dilution along the cloud edges, followed by lifting of this air as it moves toward the cloud core. This mechanism was able to generate embryo raindrop sizes (larger than $\sim$ 80 μm) in CBACT even though condensation and mixing were the only processes directly affecting the DSDs above cloud base.

When in-cloud droplet activation above cloud base was allowed (as in ACT), the increase in N_d that occurred following dilution increased water vapor competition among droplets, which resulted in reduced supersaturation, limiting condensational growth. This reduced the potential for DSD broadening from subsequent in-cloud mixing with less dilute cloud air (i.e., it limited the dilution-driven "eddy hopping" broadening mechanism). However, by constituting a source of small droplets, such activation extended DSDs to small sizes, which itself broadened the DSDs, particularly in terms of σ.

5.3.4 Simulations with fixed N_d

In the absence of collision-coalescence, sedimentation, evaporation, and droplet activation above cloud base (i.e., the CBACT case), cloud dilution could still produce wide DSDs with $\sigma > 10$ μm and $\Delta D_{99} > 30$ μm, particularly in regions of enhanced entrainment associated with the cloud's toroidal circulation(s). Above, it was proposed a dilution-driven "eddy hopping"-like mechanism to explain this behavior. Here, this mechanism and other DSD broadening processes are further investigated by removing the effects of dilution on N_d (ND100 simulations). To restrict the DSD broadening induced by dilution in the simulations, additional simulations were performed with N_d fixed to a constant value at every grid point inside the cloud, once the activation created enough droplets to exceed the cloud mask threshold of $N_d = 1$ mg^{-1}. At each time step, it was set $N_d = 100$ mg^{-1} everywhere in the cloud by scaling the existing DSD uniformly in all size bins such that the DSD mean size, shape, and width were not affected. Although doing so violated water mass conservation, this simple test allowed to remove the direct effects of DSD dilution. For the ND100 simulations, droplet activation is restricted to the cloud base only.

Figure 5.20 illustrates the effects of fixing N_d. It is seen that the DSD broadening was highly reduced in these simulations due to the lack of DSD dilution, compared to CBACT (compare Figures 5.16-5.17 and 5.20). This comparison provides further evidence for the important role of the "eddy-hopping"-like mechanism whereby dilution reduces N_d locally, leading to spatial heterogeneity of droplet growth and subsequent broadening from in-cloud mixing of DSDs. Of course, even though N_d was constant in these simulations and hence there was no direct dilution of the DSDs, there was still dilution of the thermodynamic variables from entrainment and mixing with environmental air. This could also have led to spatial variability in supersaturation and droplet growth and hence DSD broadening after in-cloud DSD mixing—another "eddy-hopping"-like mechanism. However, given the large decrease in DSD width when N_d was fixed compared to the CBACT simulations (up to a factor of ~ 3 decrease in σ and ΔD_{99} above 3 km), the dilution of thermodynamic properties appeared to be of secondary importance in broadening DSDs compared to direct dilution of the DSDs and reduction in N_d.

For the ND100 simulations, differences in the horizontally averaged profiles of σ and ΔD_{99} as a function of the model resolution remained similar to the other cases. At $t = 7$ min and below approximately 2.5 km altitude at $t = 16$ min, decreasing the *vertical* grid spacing from 100 m to 30 m reduced the horizontally averaged σ and

ΔD_{99} values by approximately 20 to 50%. There was little sensitivity to changes in horizontal grid spacing. At later times above 2.5 km, the profiles of σ and ΔD_{99} were less sensitive to the model grid spacing. This likely reflected the more complicated cloud structure and effects of the toroidal circulations that developed at these later times, including the secondary toroidal circulation that developed in the 30×30 simulation.

Figure 5.20 - Mean profiles of a,d) droplet mean diameter (D_m), b,e) standard deviation of the DSD (σ), and c,f) difference between the diameters of the 99^{th} and 50^{th} percentiles of the DSD (ΔD_{99}) for different model resolutions (colored lines labeled at the figure bottom) at $t = 7$ min and $t = 16$ min for the ND100 simulations.

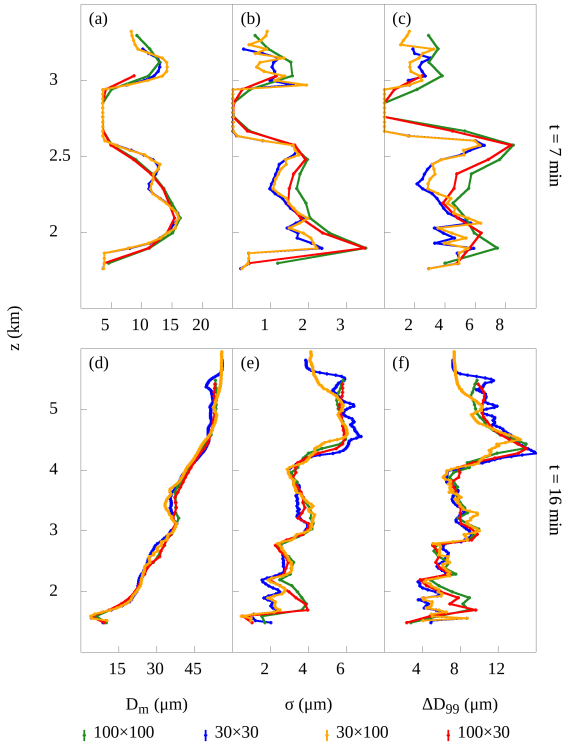

Although the effects of unphysical DSD broadening caused by vertical numerical diffusion cannot be isolated, the narrowing of DSDs as vertical grid spacing is decreased, with little sensitivity to horizontal grid spacing, is consistent with such numerical broadening. For example, Morrison et al. (2018) showed a decrease in ΔD_{99} by about a factor of 1.5-2 when the vertical grid spacing was reduced from

40 to 20 m in their idealized one-dimensional tests that included only vertical advection and condensational growth (meaning that vertical numerical diffusion was the only broadening mechanism). The potential for physical DSD broadening from the "eddy hopping"-like mechanism increases when supersaturation gradients are larger, simply because this leads to more heterogeneity in droplet growth. Because details of cloud structure and the supersaturation field are better resolved as the grid spacing is decreased, with larger supersaturation maxima and greater spatial variability (not shown), one might anticipate that broader DSDs should occur with increasing resolution. However, the opposite behavior occurred here earlier in the simulations (e.g., at $t = 7$ min), and thus the broadening effects of better resolving spatial variability in the thermodynamic fields seem to be secondary to unphysical DSD broadening from vertical numerical diffusion. Later in the simulations (e.g., at $t = 16$ min) above ~ 2.5 km, where entrainment and mixing seemed to play a more important role in the cloud evolution, there was less sensitivity of DSD width to model resolution. In this instance, it is possible that the reduction in unphysical numerical broadening from increased model resolution was compensated by increased physical DSD broadening from better resolving small-scale features and thermodynamic heterogeneities.

5.4 Remarks

The simulations analyzed in this study provided useful insights to understand the processes that lead to DSD broadening in Eulerian bin-microphysics models. Several "mechanism denial" experiments allowed identification of the effects of different processes that influenced DSDs in simulations of an idealized warm cumulus cloud. It was shown that the modeled DSD evolution was strongly affected by collision-coalescence, reflecting the rapid drop growth that occurs once embryo raindrops are generated. Collision-coalescence rates were greatest in the upper part of the cloud core similar to Khain et al. (2013). The reduction in N_d from collision-coalescence also induced droplet activation in regions of strong ascent and high supersaturation within the cloud core, consistent with the results of Hall (1980). Thus, collision-coalescence broadened the DSDs to large sizes directly, and to small sizes from the subsequent in-cloud droplet activation. The result was a broad region in the upper part of the cloud with small mean droplet sizes but large DSD standard deviations ($\sigma > 10$ μm) and broad tails ($\Delta D_{99} > 30$ μm). The occurrence of in-cloud activation in regions of strong ascent has been discussed by previous studies (HEYMSFIELD et al., 2009; PINSKY; KHAIN, 2002; SEGAL et al., 2003; YANG et al., 2015). However, because aerosols were not explicitly tracked in the model, this effect of in-cloud

droplet activation may have been overemphasized in these simulations compared to reality.

Additional simulations were analyzed to further examine the effects of resolved turbulent motion, sedimentation, evaporation, and droplet activation on DSD evolution. Turbulent eddies enhanced DSD broadening near cloud top by influencing entrainment and DSD mixing processes, while evaporation played only a minor role in DSD evolution and sedimentation had little effect. Droplet activation, especially along the cloud top, led to DSD broadening to small sizes and $\sigma > 10$ μm. This activation was associated with cloud dilution, which reduced N_d locally, inducing the activation of droplets when this air ascended. This mechanism was confirmed by simulations in which droplet activation above cloud base was turned off.

Even with collision-coalescence, sedimentation, evaporation, and in-cloud (above cloud base) droplet activation turned off in the model, and laminar flow, the dilution of parcels at the cloud interface from mixing with cloud-free environmental air still led to wide DSDs ($\sigma > 10$ μm) and large tails ($\Delta D_{99} > 40$ μm), particularly along the lateral cloud edges. From an analysis of mixing via θ_e, it was shown that the widest DSDs, in this case, tended to occur in parcels that were strongly diluted, especially for the low-resolution simulations. The reduction in N_d from dilution meant locally higher supersaturation and stronger condensational growth when this air ascended in the updraft (i.e., super-adiabatic growth, as discussed by Yang et al. (2016)), leading to broad DSDs after mixing with DSDs from the less dilute cloud core. Thus, dilution created the conditions for DSD broadening by reducing N_d locally and introducing spatial heterogeneity in droplet growth rates. This result is consistent with the idea of "eddy hopping" as a DSD broadening mechanism, whereby DSDs undergoing different growth histories are broadened by their mixing (COOPER, 1989; GRABOWSKI; ABADE, 2017; ABADE et al., 2018). This mechanism was confirmed by additional simulations also with collision-coalescence, sedimentation, evaporation, and in-cloud (above cloud base) droplet activation turned off in the model, and laminar flow, but N_d fixed at a constant value within the cloud by adjusting N_d without changing the DSD mean size, width, or shape. These simulations had much narrower DSDs and no sharp maxima in σ and ΔD_{99} along the cloud boundaries compared to the corresponding simulations that did not fix N_d.

The effects of horizontal and vertical model grid spacing on the simulated DSD characteristics were also examined. Overall, the main effect of increasing resolution in all of the process sensitivity tests was to better resolve fine-scale cloud macrophysical

and microphysical structure. Impacts on the overall DSD features were generally small, but there was a noticeable decrease in σ and ΔD_{99} in the lower part of the cloud (below about 2.5 to 3 km) with decreased *vertical* grid spacing in all of the tests. This is a cloud region that was less affected by entrianment and dilution, collision-coalescence, and other physical DSD broadening processes. Narrower DSDs with decreased vertical grid spacing were also evident in the fixed-N_d simulations with collision-coalescence, sedimentation, evaporation and in-cloud activation turned off. This sensitivity of DSD width to the model vertical resolution is a signature of DSD broadening from vertical numerical diffusion, a non-physical feature detailed in Morrison et al. (2018). Quantifying this artificial numerical broadening directly is cumbersome given that it is flow dependent and difficult to separate from the other mixing processes (e.g., horizontal mixing). Nonetheless, decreasing the vertical grid spacing from 100 m to 30 m led to reductions in σ and ΔD_{99} by 20 to 50% in the fixed-N_d simulations at earlier times (t = 7 min), consistent with the behavior of DSD broadening from vertical numerical diffusion. However, above 2.5 km at later simulation times (t = 16 min) there was little sensitivity to vertical grid spacing, which was likely due to the dominant role of other processes in DSD broadening, especially horizontal mixing. Thus, while there was a signature of artificial DSD broadening from numerical diffusion associated with vertical advection, the overall evolution of DSD width in this case was dominated by other physical mechanisms, particularly collision-coalescence, in-cloud droplet activation, and dilution, above $\sim$ 2.5 km. Note these results apply specifically to simulations of an isolated, growing cumulus cloud. For other cloud types in which these physical processes may be less active, such as stratocumulus, artificial numerical DSD broadening may play a more important role. A detailed investigation of the DSD broadening mechanisms in bin model simulations of other cloud types is left to future work.

6 VARIABILITY OF DROPLET SPECTRAL DISPERSION IN CONVECTIVE CLOUDS

In single- and double-moment bulk-microphysics parameterizations, the shape parameter of gamma DSDs is commonly fixed or diagnosed using empirical formulations. As discussed in Section 2.3, errors in the description of μ lead to erroneous representation of physical processes, such as condensation, collision-coalescence, sedimentation and riming.

In this chapter, a study of the variability of ϵ (or μ) in observations and numerical simulations of growing convective cumuli is presented, taking into account changes in the background N_a. Comparison of observations and idealized simulations of a shallow cumulus using a LES model with bin and bulk microphysics parameterizations allowed to evaluate the performance of the model and its response to varying N_a. The bin simulations contributed to deepen the analysis of the mechanisms responsible for the variability of ϵ in cumulus clouds. The bulk-microphysics simulations illustrated the impact of improving the description of μ in the model on the evolution of the simulated cloud.

A manuscript based on the results presented in this chapter is being prepared for submission to an international scientific journal.

6.1 Observations

Data from six flights that sampled clouds in locations with contrasting aerosol conditions near the Amazon basin, as part of the ACRIDICON-CHUVA campaign (WENDISCH et al., 2016; MACHADO et al., 2014) are employed here. In other publications related to the ACRIDICON-CHUVA campaign, those flights are referred as "AC07", "AC09", "AC12", "AC13", "AC18" and "AC19", respectively. AC07, AC12 and AC13 measurements belong to the Arc of deforestation, where biomass burning and anthropogenic sources generated relatively high N_a below cloud base ($\sim$2000 cm^{-3} to $\sim$ 4000 cm^{-3}). AC09 and AC18 sampled clouds in remote locations over the unperturbed rainforest, with highly homogeneous surface conditions and $N_a \approx 800$ cm^{-3} below cloud base. Finally, AC19 was performed over the Atlantic ocean, near the mouth of the Amazon River, where N_a below cloud base was ≈ 500 cm^{-3}. Table 6.1, reproduced from Cecchini et al. (2017), summarizes the main characteristics of these flights. For clarity, flights AC07, AC12, AC13, AC09, AC18 and AC19 are renamed here as "AD1", "AD2", "AD3", "RA1", "RA2" and "M1" respectively, as in Cecchini et al. (2017). AD, RA and M stand for "Arc of deforestation",

"Remote Amazon" and "Maritime", respectively.

Table 6.1 - General characteristics of the ACRIDICON-CHUVA cloud profiling missions referred in this study: aerosol number concentration (N_a, in cm^{-3}), Cloud Condensation Nuclei number concentration (N_{CCN} in cm^{-3}, for supersaturation $S = 0.48 \pm 0.033\%$) and cloud base altitude (z_{base}). The names in the third column have the following meaning: M1 – Maritime 1; RA1 and RA2 – Remote Amazon 1 and Remote Amazon 2; AD1, AD2, and AD3 – Arc of Deforestation 1, Arc of Deforestation 2, and Arc of Deforestation 3.

Region	**Flight**	**Name**	$\mathbf{N_a}$	$\mathbf{N_{CCN}}$	$\mathbf{z_{base}}$
Atlantic coast	AC19	M1	465	119	550
Remote Amazon	AC09	RA1	821	372	1125
	AC18	RA2	744	408	1650
Arc of deforestation	AC07	AD1	2498	1579	1850
	AC12	AD2	3057	2017	2140
	AC13	AD3	4093	2263	2135

SOURCE: Cecchini et al. (2017).

Differences in surface characteristics among the AC, RA and M regions were correlated with differences in atmospheric thermodynamic conditions (CECCHINI et al., 2017). Figure 6.1 illustrates the values of θ, q_v and w corresponding to in-cloud 1 Hz measurements during the six aforementioned flights (provided by the Basic HALO Measurement and Sensor System, BAHAMAS), filtered by $w > 0$ m.s^{-1} and total droplet concentration larger than 16 cm^{-3} [1]. The altitude of the cloud bases increased moving from maritime to land deforested conditions, likely due to differences in surface sensible and latent heat fluxes (FISCH et al., 2004). While the dispersion of the θ measurements remained nearly constant with height, the spread of q_v at a given level increased with altitude, with up to 500% variation near $\sim$ 5 km. The spread of q_v at a certain height is likely associated with the presence of subsaturated regions inside the cloud due to entrainment and mixing.

[1] Note that "droplet" here refers to particles measured with the Cloud Droplet Probe

Figure 6.1 - Vertical distribution of the measurements. Left panel: potential temperature (θ). Center panel: water vapor mixing ratio (q_v). Right panel: updraft speed (w) and averaged horizontal components of the wind from flight RA1 (u, v). Dots represent 1 Hz measurements filtered by $w > 0$ m.s^{-1} and $N_c > 16$ cm^{-3}. The black lines represent cloud-free averages for the RA1 flight.

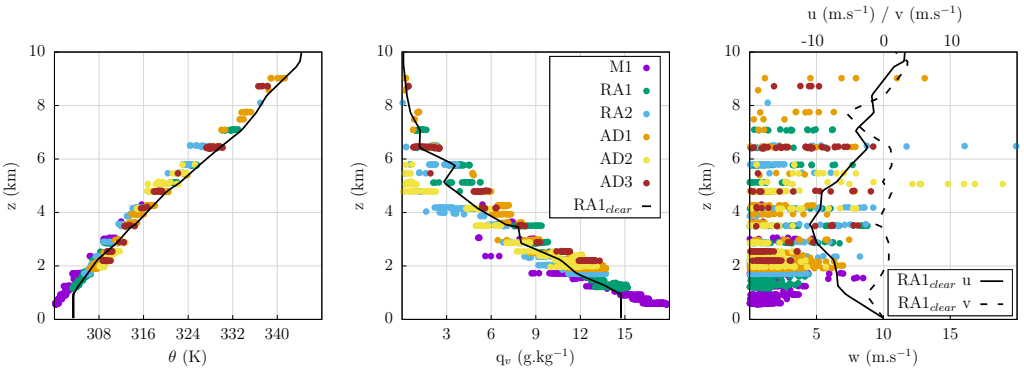

Figure 6.2 illustrates the vertical distribution of bulk properties of the particle size distributions for the 1-Hz measurements of each flight. Only measurements with total concentration larger than 16 cm^{-3} for CDP and 0.04 cm^{-3} for CIPg are displayed (the choice of these thresholds was based on counting statistics, as discussed in the next paragraph). Comparing M, RA and AD flights, it is evident that N_a was positively correlated with the concentration of CDP particles (Figure 6.2a), and negatively correlated with both the effective diameter of CDP particles (Figure 6.2b) and the concentration of CIPg particles (Figure 6.2d), as expected according to Albrecht (1989). Liquid water content (i.e., mass concentrations) was calculated from the measured particle size distributions assuming spherical liquid droplets (Figure 6.2c,f). For CDP particles, the deviation of the liquid water content from the adiabatic liquid water content (q_a) increased with height. Several factors may have determined this behavior, including precipitation and entrainment-induced dilution and evaporation. An increase of liquid water content with height for large particles measured by CIPg supports the former explanation. However, since CIPg particles have non-negligible fall velocities, evaluating precipitation production would require observations at several levels inside the clouds. Large particles (if any) produced *at* the measurement level had likely fallen to lower levels, while the large particles measured by CIPg here were probably produced very close to, but still above, the actual measurement level (note that ACRIDICON-CHUVA flights focused mainly on cloud-top and cloud base, the closer to cloud top the aircraft passes, the lower the chance of finding precipitation particles coming from *higher* levels). In fact, at warm

temperatures (the average location of the 0°C isotherm is indicated by a horizontal dashed line at $\sim$ 4.5-km altitude), the liquid water content for large particles was too low, generally smaller than 0.5 g.m^{-3}, to account for the differences between q_a and liquid water content retrieved from CDP measurements. Above the freezing level, there was a sudden increase in liquid water content and effective diameter of CIPg particles, especially for RA clouds. This coincided with an increase in the frequency of occurrence of aspherical particles, as reported by Cecchini et al. (2017) for the same flights shown here. For the measurements where aspherical particles were present, the calculated water content is likely overestimated.

Figure 6.2 - Vertical distribution of the particle concentration, effective diameter and liquid water content for CCP ($D < 50$ μm) and CIPg ($D > 50$ μm) 1-Hz measurements. The horizontal dashed line represent the average altitude of the 0 ^oC isotherm. The short-dashed lines in panel (c) represents the adiabatic liquid water content estimated from cloud base measurements for each flight.

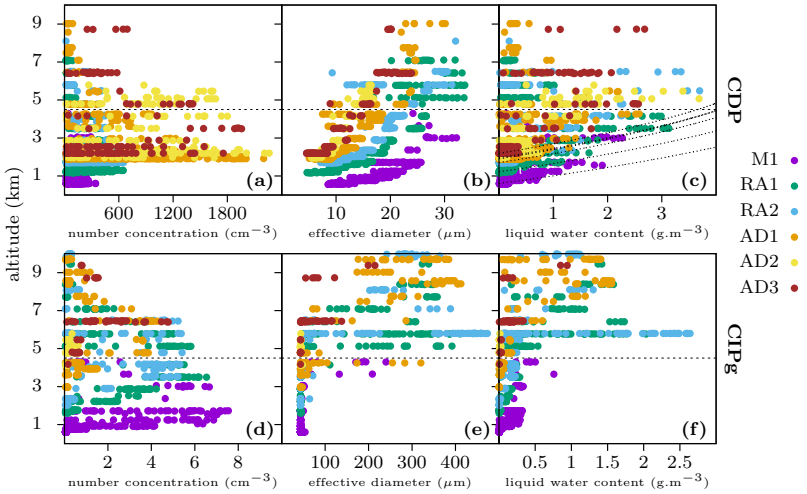

The 1-Hz observations analyzed here constitute averages over flight segments that extend for more than 100 m, thus precluding analysis of much of the intra-cloud variability. Unfortunately, there is a trade-off between the need for studying small-scale particle distributions and the need for reducing random statistical fluctuations of the counting process. Assuming a Poisson probability distribution, if follows that the measured particle concentration has to exceed 16 cm^{-3} and 0.04 cm^{-3}, for the CDP and the CIPg, respectively, for the uncertainty due to counting statistics to be less that 5% (considering an aircraft velocity of 100 m.s^{-1}, at a 1-Hz sampling rate, and reference sample volumes of 25 cm^3 and 10^4 cm^3, for the CDP and the CIPg respectively, Baumgardner et al. (2011)). Uncertainties due to counting statis-

tics are higher for size-binned particle concentrations than for total concentrations, especially for size intervals away from the mode. Additional analysis (not shown) indicated that the largest uncertainties associated with the counting process are found below the freezing level for CIPg particles, and above the freezing level, for CDP particles. Hereinafter, all quantitative analyses focus on CDP measurement. To improve the reliability of the DSD information obtained from CDP measurements, averages of the 1-Hz data over 100-m and 500-m intervals of height above cloud base are employed. Although small aspherical particles ($D < 50\mu$m) were often detected in these measurements (CECCHINI et al., 2017), is unclear whether they constitute large aerosols or ice particles. For simplicity, particles measured by CDP will hereinafter be referred as "droplets".

6.1.1 DSD broadening mechanisms inferred from the observations

Figure 6.3 shows the average DSDs every 100 m depth for each flight, the height above cloud base (h) is represented by a color scale. Hereinafter, all observations are filtered according to a mask defined by $w > 0$ m.s^{-1}, $N_c > 16$ cm^{-3} and cloud water content (q_c) larger than 0.1 g.m^{-3}. Droplet growth and spectral broadening with height were noticeable for all flights. The broadest DSDs tended to contain multiple modes, which was likely a result of larger variability in individual 1 Hz DSDs at more advanced stages of cloud development. Perhaps the most remarkable difference among DSDs from the different flights is the concentration of smaller particles close to cloud base. At the lowest levels, as N_a increases, the concentration of droplets with $D <\sim 8$ μm increased several orders of magnitude, thus resulting in broader DSDs in the polluted flights, compared to clean flights.

Figure 6.3 - Average DSDs every 100 m depth for each flight. The color scale represents height above cloud base (h).

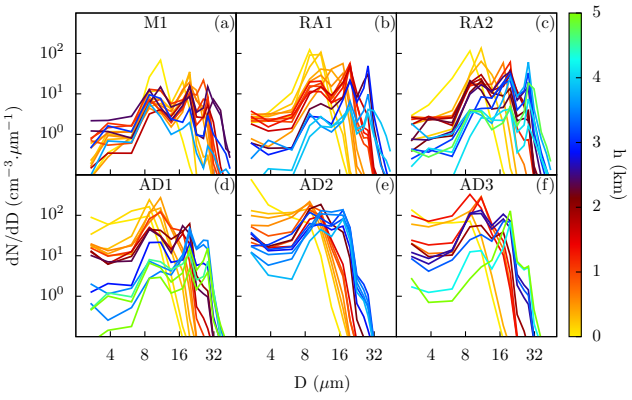

The relationship of DSD shape with N_a, w and h from ACRIDICON-CHUVA measurements was studied by Cecchini et al. (2017). Their analysis is extended here to explore more details of the DSD variability. First, to provide some context, some of the aspects discussed by Cecchini et al. (2017) are illustrated here. In their study, no strong correlation was found between w and ϵ, therefore the this illustration focuses on the variability of ϵ with respect to N_a and h.

Figure 6.4 - Mean diameter (D_m), standard deviation (σ) and relative dispersion (ϵ) corresponding to the 100-m depth averaged DSDs in Figure 6.3. The bottom panels show a zoom on the lower 1 km above cloud base.

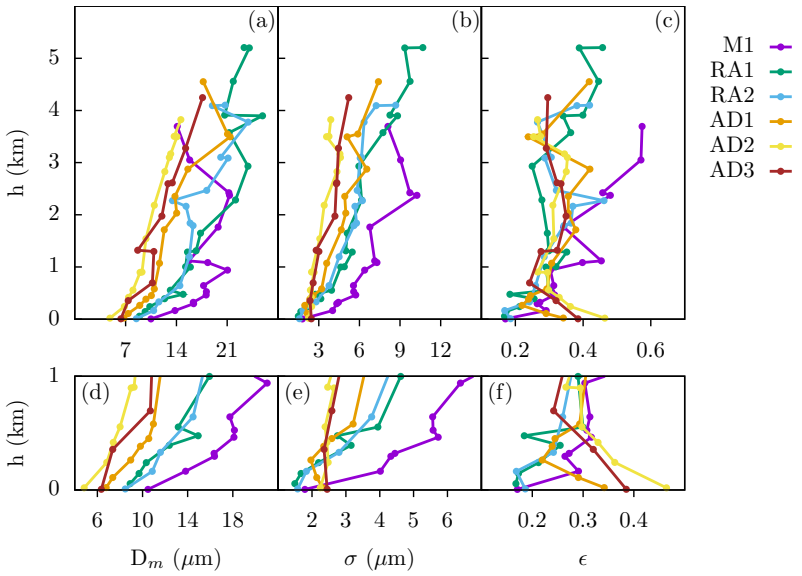

Cecchini et al. (2017) showed that, in pristine conditions, the DSD shape varies much more with h (which is considered as a proxy for cloud development) than in polluted conditions. They also concluded that the correlation between ϵ and N_a is opposite in sign above and below $h \sim 500$ m. To complement their analysis, vertical profiles of D_m, σ and ϵ for the 100-m average DSDs (Figure 6.4) are shown here. Figure 6.4a,b shows that D_m was negatively correlated with N_a for a fixed h. On the other hand, σ and N_a were positively correlated near cloud base but negatively correlated at higher h (Figure 6.4b,e). This behavior was associated with different rates of change of σ with height, depending on N_a, i.e., $\left.\frac{\partial \sigma}{\partial h}\right|_{N_a}$ decreased as N_a increased. A faster rate of increase of σ with height in clean clouds was consistent with more efficient DSD broadening and earlier rain initiation. Different ratios of σ to D_m for a given N_a explain large differences in ϵ close to the cloud base (Fig-

ure 6.4f), with ϵ varying by at least 30% at the lowest level. Taking the derivative of $\epsilon(N_a, h)$ with respect to N_a, it is seen that the condition for $\left.\frac{\partial \epsilon}{\partial N_a}\right|_h$ to be positive (i.e., ϵ increases with increasing N_a) is that $\left.\frac{\partial \sigma}{\partial N_a}\right|_h > \frac{\sigma}{D_m}\left.\frac{\partial D_m}{\partial N_a}\right|_h$, which holds for $\left.\frac{\partial D_m}{\partial N_a}\right|_h < 0$ and $\left.\frac{\partial \sigma}{\partial N_a}\right|_h > 0$ at cloud base. Increasing ϵ with increasing N_a at cloud base is in agreement with Chen et al. (2016). As Chen et al. (2016) pointed out, DSD narrowing from condensational growth slows down as N_a increases in the aerosol-limited regime (REUTTER et al., 2009), due to the reduction in the parcel supersaturation compared to a more pristine situation. However, their analysis applied condensational growth theory in an adiabatic parcel at the level of maximum supersaturation. Therefore, this mechanism cannot simply be extrapolated to other levels inside clouds, where other mechanisms, such as collision-coalescence and entrainment/mixing may play important roles. In fact, for the observations analyzed here, there was no clear relationship between ϵ and N_a above cloud base (Figure 6.4).

Figure 6.5 - Averages of the relative dispersion (ϵ) for 500-m h and 0.5 q_c/q_a intervals in the observations.

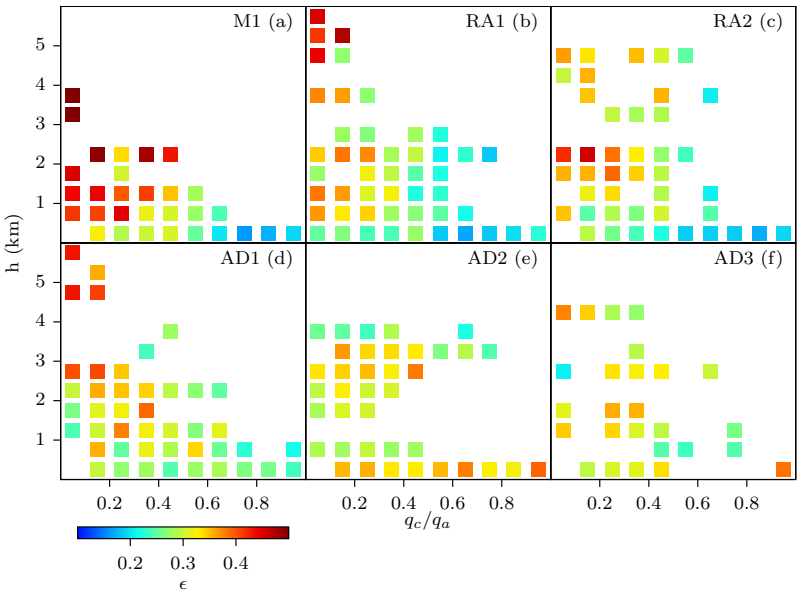

To illustrate the variability of DSD shape in the observations further, the average of ϵ for 500-m intervals in h and intervals of 0.5 in q_c/q_a, was calculated (Figure 6.5). Near cloud base, it is reasonable to regard q_c/q_a as a proxy for the adiabaticity of the cloud, with q_c deviating from q_a in cloud regions that underwent mixing with the

environment. The increase of ϵ with increasing N_a at cloud base discussed above was even more evident at high q_c/q_a values, i.e., within nearly undiluted cloud cores. For $q_c/q_a > 0.5$, ϵ increased by $\sim 69\%$ from the M and RA flights to the AD flights, while the increase was only $\sim 15\%$ for $q_c/q_a \leq 0.5$. Thus, it follows that the variability of ϵ at cloud base described above was mainly determined by adiabatic processes, which justifies the consistency with the analysis of Chen et al. (2016). On the other hand, Figure 6.5 indicates that, for lower values of N_a (flights M1, RA1 and RA2), ϵ tended to decrease as q_c/q_a increased at all heights, with ϵ being generally larger than 0.3 for $q_c/q_a < 0.5$. Although this behavior can be associated with the mixing of droplets undergoing different paths inside the cloud (i.e., the "eddy-hopping" mechanisms Grabowski and Abade (2017)), other processes can simultaneously decrease q_c and broaden the DSDs too. For instance, as collision-coalescence intensifies, which depends strongly on h for a given N_a (FREUD; ROSENFELD, 2012), the DSD width increases and precipitation-sized droplets are eventually produced, leading to a decrease in q_c/q_a after sedimentation. Overall, ϵ appeared to be less correlated with q_c/q_a for the AD flights, consistent with delayed rain development and enhanced in-cloud droplet activation in polluted clouds, which broadens the DSDs toward smaller sizes. As it is discussed later in this section, in-cloud droplet activation can be significant in both adiabatic and diluted cloudy areas.

An increase in cloud dilution with h as a consequence of entrainment and mixing, as well as a decrease in q_c via conversions to precipitation and sedimentation, likely explain the relatively low number of observations with high q_c/q_a ($q_c/q_a > 0.5$) above the cloud base. Although the existence of undiluted or nearly undiluted convective cloud cores has been reported by several observational studies (e.g., Khain et al. (2013) and references therein), if any undiluted cloud cores occurred in the cases here they would likely be missed since the clouds were mainly sampled by the cloud-top (or base) aircraft penetrations. Hypothetically, if there were observations with high q_c/q_a at all levels, and if the same $\epsilon - q_c/q_a$ relationship found in the measurements shown here were applicable to high q_c/q_a values too, the average ϵ at each height would be smaller than in Figure 6.4 for the clean cases, with smaller changes in the profile of ϵ for the polluted cases. This way, the positive correlation between ϵ and q_c/q_a would be extended to the entire profile, instead of being restricted to only cloud base, erroneously suggesting that DSDs were broader in polluted clouds throughout the cloud. Therefore, neglecting changes in q_c/q_a hinders important details of the relationship between aerosol loading and DSD width. In Section 6.2.3.1, the relationship $\epsilon - q_c/q_a$ is investigated, including for high q_c/q_a values above cloud base, based on idealized bin-microphysics simulations.

Since DSD broadening ultimately triggers collision-coalescence, changes in DSD shape are relevant for investigating warm rain production in clouds. Khain et al. (2013) suggested that the formation of precipitation in warm convective clouds is driven by collision-coalescence in nearly undiluted cloud cores. Figure 6.5 shows that the largest values of relative dispersion in the observations were associated with low q_c/q_a. However, low q_c/q_a is not necessarily driven solely by cloud dilution. As mentioned above, q_c/q_a can also be decreased by precipitation. All else being equal, the wider the DSD, the more rain will be produced via collision-coalescence, decreasing q_c after sedimentation and moving towards the left side of the graphs in Figure 6.5. Thus, DSD broadening from entrainment followed by dilution and mixing and from collision-coalescence in adiabatic cores are indistinct in Figure 6.5. Moreover, large ϵ values are not necessarily related to the generation of larger droplets. In fact, considering equally spaced size bins with mean diameters D_1 and D_2 ($D_1 < D_m < D_2$), ϵ is increased more by increasing the concentration in D_1 than by a similar increase in D_2, provided that $|D_1 - D_{m1}| = |D_2 - D_{m2}|$, with D_{m1} and D_{m2} being the mean diameter of the DSD after increasing the concentration in D_1 or D_2, respectively.

Figure 6.6 - Similar to Figure 6.5 but for the difference between the diameters of the 99^{th} and 50^{th} percentiles of the DSD (ΔD_{99}).

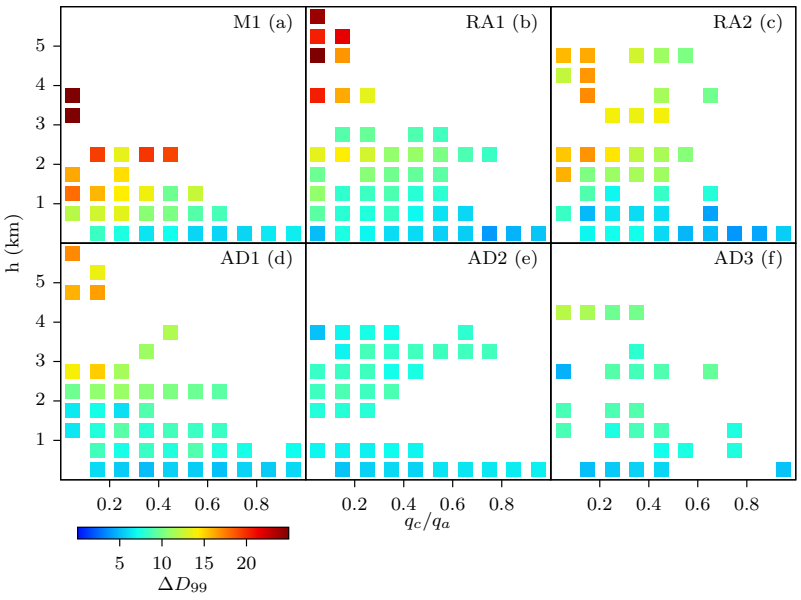

To focus on the right (large sizes) tail of the DSD, Figure 6.6 illustrates the distribution of the averages values of ΔD_{99} for each pair $(q_c/q_a; h)$. Like ϵ, ΔD_{99} was larger for smaller q_c/q_a in the clean cases, but unlike ϵ, ΔD_{99} had a specific dependence

on h for each aerosol condition. This is consistent with the well established effect of aerosols on precipitation efficiency (ALBRECHT, 1989). However, ΔD_{99} was better correlated with ϵ in the M, RA1 and RA2 flights, indicating that the distribution of ϵ in these cases was associated with DSD broadening toward large droplet sizes, than in the AD flights. In the AD flights, the trends of ΔD_{99} across the space of $(q_c/q_a; h)$ differed from those of ϵ. Lower values of ΔD_{99} in the polluted flights, especially AD2 and AD3, indicated that the relatively large ϵ values across most of the space of $(q_c/q_a; h)$ for these cases were associated with broadening to small drop sizes.

In summary, these results suggest that two main broadening mechanisms determined the variability of ϵ above cloud base in the sampled clouds: collision-coalescence and in-cloud droplet activation. In clean cases, droplet growth by collision-coalescence dominated, increasing ϵ and ΔD_{99} with increasing h while simultaneously decreasing q_c/q_a by precipitation. In polluted cases, in-cloud activation played a relatively greater role at most heights, evidenced by the highly uniform distribution of relatively large values of ϵ (~ 0.3) and relatively low values of ΔD_{99} ($<\sim 12\mu$m). In-cloud activation can occur in diluted and nearly undiluted cloud regions, depending on the transport of unactivated aerosols from cloud base and on entrainment rates. Since activation has little direct impact on q_c [2], the larger values of ϵ were not restricted to low q_c/q_a.

6.1.1.1 Variability of the shape parameter in the observations

If the DSD follows a gamma distribution, then the ratio $\sigma/D_m \equiv \epsilon$ is related to μ ($\mu = \frac{1}{\epsilon^2} - 1$). Figure 6.7 illustrates the variations of μ depending on q_c/q_a and N_c, where N_c was averaged for intervals of $\Delta\mu = 5$ and $\Delta(q_c/q_a) = 0.1$. Considering that the largest uncertainties in the DSD measurements were found above the freezing level (Section 6.1), only points with temperatures higher than 0 ^{o}C are included in Figure 6.7. As expected, the largest values of N_c were found at high q_c/q_a.

As discussed in the previous section, negative (positive) correlations between ϵ (or μ) and q_c/q_a responded primarily to enhanced rain production in the clean cases, while in polluted cases, the variability of ϵ (or μ) was less related to changes in q_c/q_a. The role of in-cloud droplet activation was evident in the relationship between N_c and μ. For $q_c/q_a <\sim 0.5$ in the cleaner cases, and for most q_c/q_a values in the most polluted cases (AD2, AD3), μ was inversely related to N_c overall, again suggesting

[2] Activation does cause an *indirect* effect on q_c. Increasing N_c by activation decreases the phase relaxation timescale, thus decreasing the supersaturation and consequently the condensation rate.

the role of in-cloud droplet activation in broadening the DSDs toward the left (small) side of the size spectrum. Note that collision-coalescence reduces μ as well as N_c [3], so the decrease of μ with increasing N_c for a given q_c/q_a was necessarily related to new droplet formation. Droplet activation at low q_c/q_a above cloud base may occur in diluted cloud regions, associated with the entrainment of aerosols and the local increase in the supersaturation caused by a reduction of N_c due to dilution, or in undiluted regions of the cloud, due to the activation of aerosols ascending from cloud base. As discussed in Chapter 5, the reduction of N_c by collision-coalescence increases the supersaturation locally by increasing the phase relaxation timescale, thus leading to activation of remaining aerosols and large condensation rates. Thus, there can exist favorable conditions for in-cloud droplet activation at low q_c/q_a, either related to dilution or precipitation, in both clean clouds and polluted clouds.

Figure 6.7 - Averages of the cloud droplet number concentration (N_c) for intervals of 5 units of μ and 0.1 units of q_c/q_a in the observations.

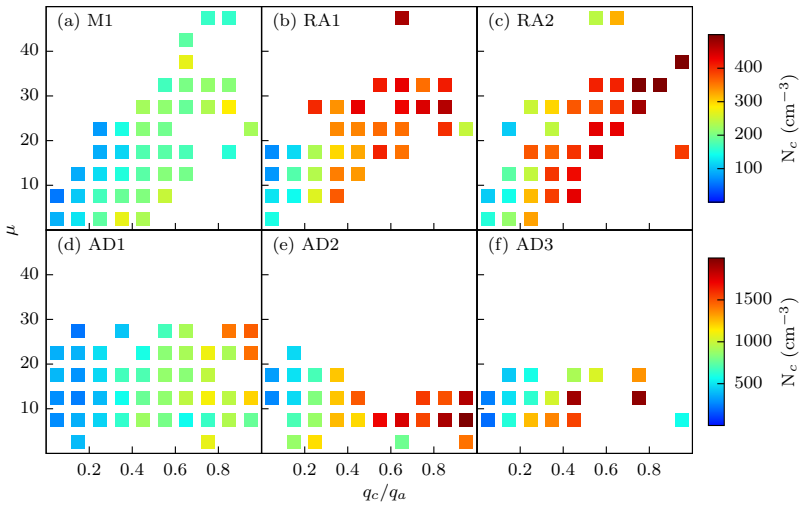

These results indicate that, for the convective clouds sampled during ACRIDICON-CHUVA, bulk parameterizations that diagnose μ as inversely related to N_c are valid only for limited ranges of q_c/q_a and N_a ($q_c/q_a <\sim 0.5$ or $N_a > 3000\ cm^{-3}$). In clean clouds, μ was positively correlated with N_c overall, considering the full range of q_c/q_a. In order to analyze the potential for diagnosing μ from N_c and/or q_c/q_a, linear functions for μ depending on N_c (μ_1) and q_c/q_a (μ_2) separately, as well as a

[3]Collisional breakup can increase N_c, but it depends on the presence of drops with diameter of at least a few millimeters (PORCù et al., 2013). Drops larger than 100 μm are rare in these observations.

power law depending on both q_c/q_a and N_c (μ_3) were fitted. Results are summarized in Table 6.3, for clean (M1, RA1 and RA2), polluted (AD2, AD3) and transition (AD1) aerosol conditions. Figure 6.8 shows scatter plots of parameterized μ against observed μ for each aerosol regime. For the clean cases, μ_2 is a better approximation to μ compared to μ_1, with an increase of $\sim 34\%$ in the root-mean-square error (RMSE) from μ_2 to μ_1. For polluted cases, μ_1 and μ_2 gave similar RMSE. In all cases, no gain is obtained by considering both q_c/q_a and N_c in a power law functional relationship. Therefore, it can be concluded that q_c/q_a is more adequate for describing the variability of μ in these flights than N_c, at least for the functional relationships tested here.

Figure 6.8 - Scatterplots of observed versus parameterized shape parameter (μ) using the relationships specified in Table 6.3 for each aerosol regime: clean ($N_a < 900$ cm^{-3}, flights M1, RA1 and RA2), transition ($N_a \sim 2500$ cm^{-3}, flight AD1), and polluted ($N_a > 3000$ cm^{-3}, flights AD2 and AD3).

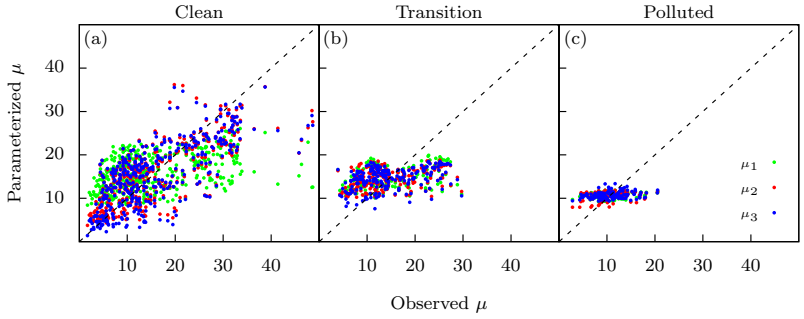

To represent the variations in the slope of the linear function that relates μ and q_c/q_a for different aerosol conditions, it was derived μ_4 (see Table 6.3) from linear fits of μ as a function of q_c/q_a in each flight. Figure 6.9 illustrates the performance of this approximation compared to the parameterizations of Grabowski (1998), Rotstayn and Liu (2003), Thompson et al. (2008) and Morrison et al. (2009) (Table 6.2), which diagnose μ from N_c. Despite the large scatter of μ_4, around the 1 : 1 line from the actual μ, it reduces the RMSE up to $\sim$ 3 times compared to the other parameterizations. Figure 6.9 shows that the biggest improvements introduced by μ_4 are for larger values of μ. This is especially important for representing rain initiation in bulk models, by modulating cloud droplet autoconversion and self-collection for the formulations for these processes that depend on μ.

Figure 6.9 - Scatterplot of observed versus parameterized shape parameter (μ) using the μ_4 relationship defined in Table 6.3 and the parameterizations specified in Table 6.2.

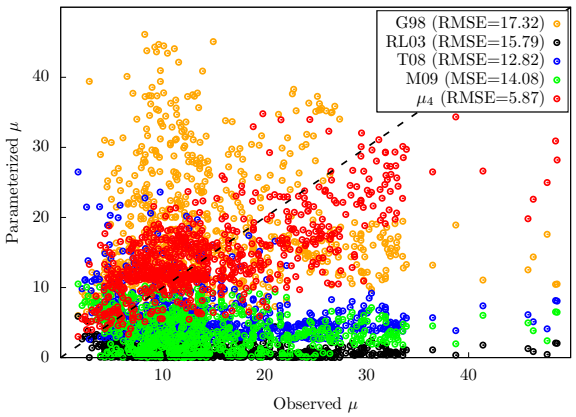

Table 6.2 - Parameterizations for the relative dispersion (ϵ)/shape parameter (μ) illustrated in Figure 6.9. N_c represents the droplet number concentration, in cm^{-3}.

Reference	**Expression**
Grabowski (1998)	$\epsilon = 0.146 - 5.964 \times 10^{-2} \ln\left(\frac{N_c}{2000}\right)$
Rotstayn and Liu (2003)	$\epsilon = 1 - 0.7e^{-0.003N_c}$
Thompson et al. (2008)	$\mu = \frac{1000}{N_c} + 2$
Morrison et al. (2009)	$\epsilon = 5.714 \times 10^{-4} N_c + 0.2714$

In summary, results from the ACRIDICON-CHUVA observations provided interesting insights into microphysical characteristics of Amazonian clouds. Specifically, it has been shown here that the spatial variability of DSD widths could be approximately described by means of the ratio q_c/q_a, especially in clean clouds, presumably due to the predominance of collision-coalescence which broadens the DSDs while also decreasing q_c through precipitation. However, the lack of observations closer to the center of mass of the clouds limited the scope of these conclusions. In the next section, results from simulations of an idealized cumulus cloud are discussed to complement the analysis of the observations.

Table 6.3 - Fitted functions relating the shape parameter (μ) with N_c and/or q_c/q_a for each aerosol regime in the observations: clean ($N_a <$ 900 cm^{-3}, flights M1, RA1 and RA2), transition ($N_a \sim 2500$ cm^{-3}, flight AD1), and polluted ($N_a > 3000$ cm^{-3}, flights AD2 and AD3).

	Clean	**Transition**	**Polluted**
$\mu_1 = aN_c + b$	$a = 0.0335 \pm 0.0035$ $b = 7.0585 \pm 0.9975$ $RMSE = 8.63$	$a = 0.0065 \pm 0.0011$ $b = 9.4835 \pm 0.9443$ $RMSE = 5.76$	$a = -0.0014 \pm 0.0006$ $b = 12.0728 \pm 0.6166$ $RMSE = 3.23$
$\mu_2 = a\left(\frac{q_c}{q_a}\right) + b$	$a = 33.2747 \pm 1.5260$ $b = 3.02492 \pm 0.6646$ $RMSE = 6.45$	$a = 8.8067 \pm 1.5240$ $b = 10.0103 \pm 0.8889$ $RMSE = 5.79$	$a = -4.0482 \pm 1.2540$ $b = 11.9921 \pm 0.4847$ $RMSE = 3.19$
$\mu_3 = a\left(\frac{q_c}{q_a}\right)^b N_c^c$	$a = 27.5022 \pm 7.9480$ $b = 0.8204 \pm 0.0489$ $c = c = 0.0435 \pm 0.0485$ $RMSE = 6.52$	$a = 5.0548 \pm 3.4370$ $b = 0.1258 \pm 0.0766$ $c = 0.1763 \pm 0.0955$ $RMSE = 5.80$	$a = 15.2420 \pm 9.3820$ $b = -0.0586 \pm 0.0687$ $c = -0.0649 \pm 0.0795$ $RMSE = 3.21$
$\mu_4 = a\left(\frac{q_c}{q_a}\right) + b$	$a = m_a N_a + n_a \quad b = m_b N_a^{n_b}$ $m_a = -0.0126 \pm 0.0006 \quad n_a = 40.9953 \pm 1.3880$ $m_b = 0.0125 \pm 0.0228 \quad n_b = 0.8449 \pm 0.2294$ $RMSE = 5.87$		

6.2 Simulations

Here, the results of idealized simulations of a single convective cloud, using a LES configuration of the WRF model (SKAMAROCK et al., 2008) are presented. Unless specified, all model configurations are the same as the 3D simulation in Chapter 5.

6.2.1 Model description

The model horizontal domain comprised 40 km × 20 km (x × y) with open lateral boundary conditions. The top of the model vertical grid was located at 10 km altitude, with a 3-km damping layer. As initial conditions, averaged profiles of θ, q_v and the horizontal components of the wind (u and v) measured outside of the clouds (no cloud or rain drops present) in the RA1 flight were employed. These profiles are represented by black lines in Figure 6.1. The initial values of θ and q_v were assumed to be constant with height from surface to cloud base, to roughly mimic a well-mixed boundary layer. The initial u and v were assumed to be equal to zero at the surface, and increasing linearly from the surface to the cloud base.

Results using two different microphysics schemes, TAU and M09, are discussed here. The TAU scheme includes only warm phase processes. The DSD was divided into 35 mass-doubling bins with radii ranging between 1.56 μm and 5080 μm, approximately. In the bulk parameterization of M09, cloud droplets were represented by a gamma distribution, with μ varying between 2 and 10 depending on N_c, following the observations of Martin et al. (1994) (Table 6.2). For this study, the same droplet activation method employed in TAU was applied in the M09 scheme. The condensation/evaporation rates were calculated assuming saturation adjustment. Additionally, for parameterizing collision-coalescence processes (i.e., autoconversion, accretion and selfcollection of both cloud droplet and rain drops), the method of Seifert and Beheng (2006) was used in substitution of the scheme of Khairoutdinov and Kogan (2000) that is employed in the standard version of M09. Seifert and Beheng (2006) considers a threshold diameter of 80 μm to distinguish cloud droplets from rain drops.

In both microphysics schemes, aerosols with radii larger than the critical radius defined by Köhler theory (Equation 3.3), were instantaneously activated. All newly activated droplets were assumed to acquire a radius of $\sim 1.5\mu$m, thus the effects of large aerosols and GCCN are not explored.

Aerosols were considered to be uniformly distributed throughout the model do-

main at $t = 0$, following a log-normal size distribution. According to ACRIDICON-CHUVA (flight RA1) measurements below cloud base, $\bar{r}_a$ and σ_a were specified as 0.07 μm and 1.5, respectively. $\kappa = 0.1$ was assumed, based on previous studies of aerosol properties over the Amazon (GUNTHE et al., 2009; MARTIN et al., 2010; PÖHLKER et al., 2016). The aerosol size distribution was represented by a set of 19 bins, for radii between 0.0076 and 7.6 μm (KOGAN, 1991), and was allowed to vary through activation and advection. Aerosol replenishment was neglected.

The bin-microphysics simulations were employed to extend the analysis of the observed relationship $\mu - q_c/q_a$ to include more levels inside the cloud, taking advantage of the information the model provides regarding microphysical process rates throughout the cloud. The bulk microphysics scheme was used to illustrate the effect of the fitted $\mu - q_c/q_a$ expression on the calculation of bulk processes rates, compared to the original M09 scheme.

6.2.2 General characteristics of the simulations

The nomenclature used for each simulation is shown in Table 6.4. Each simulation is identified by the type of microphysics scheme used (i.e., bin or bulk), followed by up to two subscripts. One of the subscript is used exclusively for Bulk simulations, and indicates the approach employed to diagnose μ (0 for the original M09 approach, μ for the expression fitted from the observations here, i.e., μ_4). The other subscript represents the value of N_a assumed at $t = 0$ (c when $N_a = 900$ cm^{-3} and p when $N_a = 3000$ cm^{-3}). Whenever a subscript is missing, it means that text refers to both options of the corresponding subscript.

Table 6.4 - Nomenclature used for the simulations.

Type	**μ approach**	**$N_a = 900$ cm^{-3}**	**$N_a = 3000$ cm^{-3}**
Bin	–	Bin$_c$	Bin$_p$
Bulk	M09	Bulk$_{0c}$	Bulk$_{0p}$
	μ_4	Bulk$_{\mu c}$	Bulk$_{\mu p}$

Figures 6.10 and 6.11 show average cross sections of q_c and N_c, respectively, in simulations with $N_a = 900$ cm^{-3} and $N_a = 3000$ cm^{-3}, using the bin and bulk approaches, as specified in Table 6.4. Although the bulk scheme included ice processes, the amounts of ice, snow and graupel produced in these simulations were negligible small compared to cloud and rain water. As a result of having the same thermo-

dynamic background, the shape and size of the clouds in different simulations were similar at each displayed time, at least up to $t = 12$ min. From $t = 15$ min on, differences in rain production determined changes in the structure of the clouds among simulations. Maximum values of N_c in the simulations with $N_a = 3000$ cm^{-3} were at least twice the maximum of N_c in the simulations with $N_a = 900$ cm^{-3}. Correspondingly, rain developed earlier in the latter. At $t = 18$ min, rain mass concentrations exceeded 2 g.m^{-3} in the upper half of the cloud in the tests with $N_a = 900$ cm^{-3}, while they were generally less than 1 g.m^{-3} in the tests with $N_a = 3000$ cm^{-3}. The changes in rain production due to varying N_a were more pronounced in Bulk$_0$ simulations compared to Bin simulations, with rain initiating earlier (later) in Bulk$_{0c}$ (Bulk$_{0p}$) than in Bin$_c$ (Bin$_p$). On the other hand, rain production was significantly delayed in Bulk$_\mu$ simulations with respect to Bulk$_0$ and Bin, as a consequence of the different treatment of μ. In Section 6.2.4, the reasons for the differences between Bulk$_0$ and Bulk$_\mu$ are discussed, focusing on the effect of μ on the rate of collision-coalescence.

Note that, although the same activation method was used in all cases, there were remarkable differences in N_c between Bin and Bulk simulations for the same N_a (Figure 6.11), especially in the most polluted situation. This was related to differences in the evolution of the resolved supersaturation in Bin and Bulk, with the maximum supersaturation occurring in undiluted or nearle undiluted regions in the upper half of the cloud in the Bulk simulations and at cloud base or near entrainment regions in the Bin simulations (not shown). As a consequence, activation was more intense in Bulk than in Bin within the cloud core. Differences in the evolution of the supersaturation among simulations with different microphysics schemes were likely associated with the treatment of the condensation/evaporation (i.e., explicit water vapor diffusion in TAU versus saturation adjustment in M09, Grabowski and Jarecka (2015), Grabowski and Morrison (2017)) [4]. A detailed investigation of the mechanisms driving differences in N_c between the Bulk and Bin simulations is left for future work, but the particular behavior of N_c is taken into account here when comparing the simulations. Larger N_c was consistent with later rain initiation in Bulk$_p$ compared to Bin$_p$. However, earlier rain initiation and larger N_c in Bulk$_{0c}$ with respect to Bin$_c$, evidenced that collision-coalescence was more efficient in the former. The reasons for this behavior are discussed in Section 6.2.4.

[4]Note that calculation of the critical diameter for activation here was based on the resolved supersaturation at the beginning of the time step, i.e., before removing water vapor by condensation/evaporation or other water vapor sink processes.

Figure 6.10 - Average cross sections of cloud water content (q_c), rain water content and wind velocity (m.s^{-1}) for several times (rows) in different simulations (columns). Averages in cloudy areas of the cross section include only points at which the liquid water content is higher than 0.1 g.m^{-3}. Averaged rain water contents thresholds of 1 g.m^{-3}, 2 g.m^{-3} and 3 g.m^{-3} are represented by thin, continuous, black contours, shaded black contours and thick, continuous, black contours, respectively. The area enclosed between purple lines corresponds to averaged temperatures between -10 ^{o}C and 0 ^{o}C. The vectors represent the averaged wind velocity field.

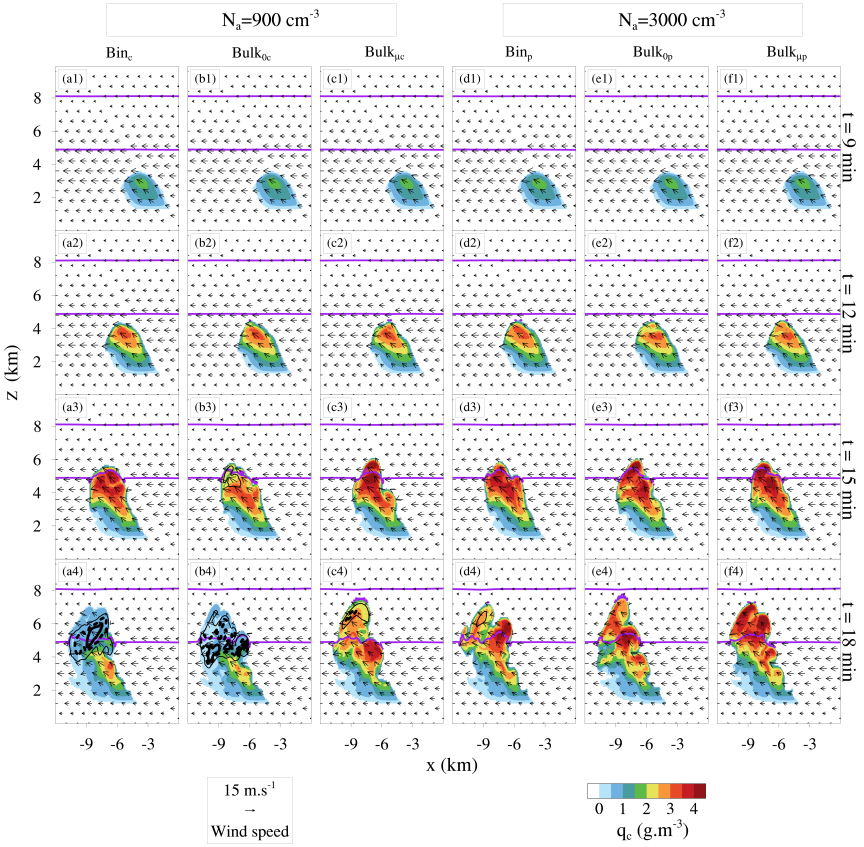

6.2.3 Comparison between the bin-microphysics simulations and the observations

In order to compare results from the simulations with the observations presented in Section 6.1, the cloud top was tracked every 1 min in the simulations. For consistency, the same filter was applied to observations and model outputs, i.e., $N_c > 1$ cm^{-3}, $q_c > 0.1$ g.kg^{-1} and $w > 0$ m.s^{-1}. Since the exact distance at which the observations were obtained with respect to the cloud tops is unknown, different positions below the top of the simulated cloud were considered. Figure 6.12 shows horizontal averages of q_c and N_c for several heights below cloud top in the Bin$_c$ and Bin$_p$ simulations,

along with the mean profiles corresponding to flights RA1 and AD2, respectively. These flights were chosen as a reference because the average values of N_a measured below cloud base in them (821 cm^{-3} and 3057 cm^{-3}, respectively) were similar to the values of N_a assumed in the simulations. Different colors in Figure 6.12 represent different "trajectories" Ln at which the sampled model level was located n grid levels below the highest cloudy pixel at all times in the simulations. Given the large sampling uncertainties related to the observations of large drops (see Section 6.1), this comparison focuses on cloud droplets only.

Figure 6.11 - Similar to Figure 6.10 but for the cloud droplets (filled contours) and rain drops (0.1 cm^{-3}, 0.3 cm^{-3} and 0.5 cm^{-3} black contours) averaged number concentrations (N_c).

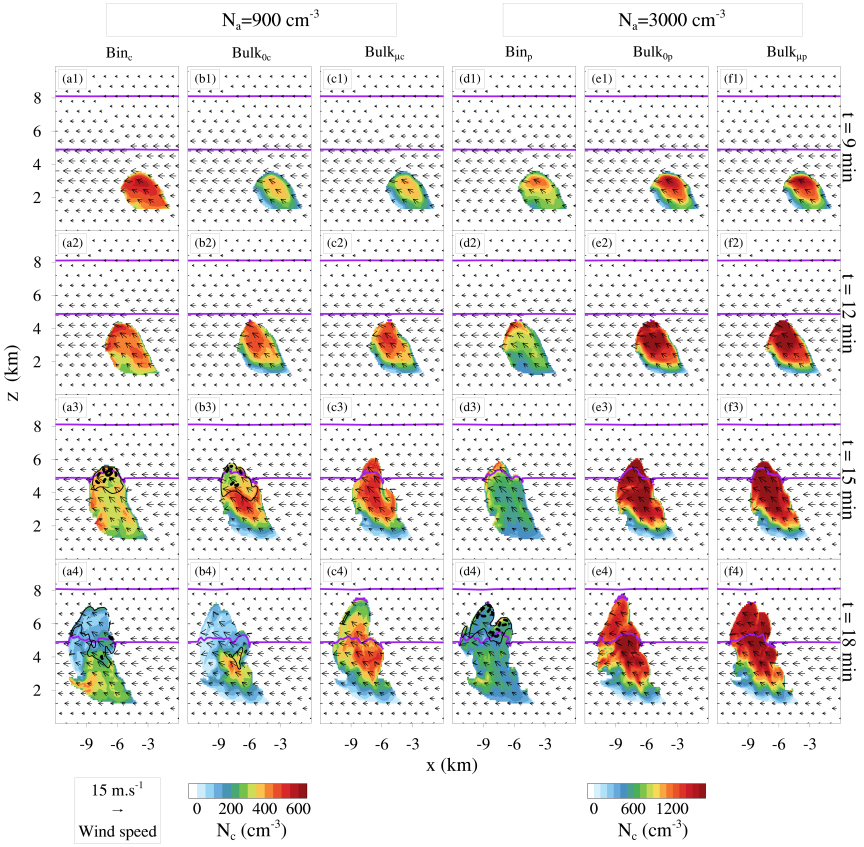

Figure 6.12 shows that the cloud-top values of q_c in the simulations increased as n increased, i.e., moving away from the cloud top. Also, as in the observations, the cloud-top values of q_c in the simulations exhibited a well defined maximum at $\sim$ 3-km above cloud base in the clean case and at $\sim$ 4-km above cloud base in the

polluted case. As discussed in Section 6.2.2, the mean q_c increased with h until the levels where the sink of q_c from rain production and entrainment/dilution exceeded the source of q_c by condensation. For all the choices of Ln, the peak of q_c occurred at lower levels in the simulation with $N_a = 900$ cm^{-3} than in the simulations with $N_a = 3000$ cm^{-3}. This was consistent with the delayed rain generation at larger N_a, as seen in the observations. However, the evolution of q_c in real clouds was also be affected by mixed-phase processes. According to Cecchini et al. (2017), the frequency of occurrence of large ($D > 50$ μm), aespherical particles in these observations increased faster with height above the freezing level in the RA flights (cleaner) than in the AC flights (polluted). This suggests that conversions from cloud water to ice may have constituted a significant sink of q_c close the heights where the peak of q_c was found in the observations, in contrast with the Bin simulations, where only warm phase processes were considered.

Figure 6.12 - Averaged profiles of cloud water content (q_c) and cloud droplet number concentration (N_c) from flights RA1 (a,c) and AD2 (b,d) and from the top of the cloud in Bin$_c$ (a,c) and Bin$_p$ (b,d). Colored contours represent averages at levels Ln located n model grid levels below the highest cloudy pixel at all times in the simulations.

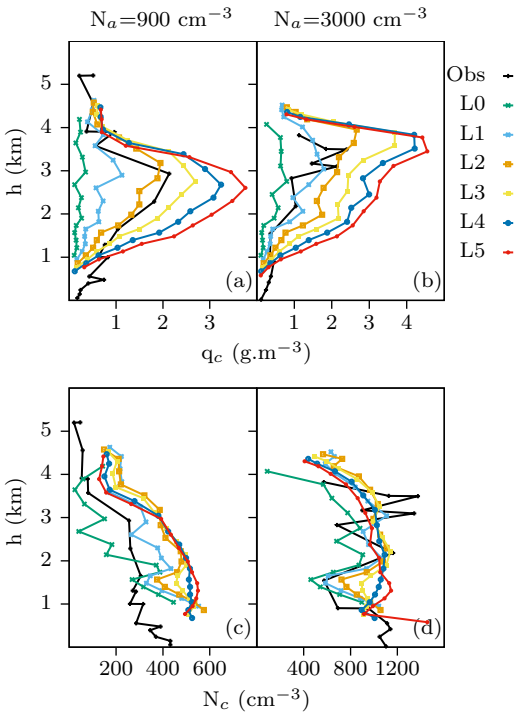

The variations among the N_c trajectories behaved notably different from the variations in the q_c trajectories. In general, N_c values converged as n increased, i.e., the differences in N_c among trajectories decreased as n increased. Nonetheless, values of N_c in $L1$ were up to 5 times the values of N_c in $L0$. The presence of sharp gradients of N_c near the cloud upper edges contrasted with the smoother spatial distribution of q_c. Since higher moments of the DSD give larger weights to larger droplets, the presence of sharp gradients of N_c, not evident in q_c, are attributed to the presence of small droplets associated with cloud top activation. Cloud-top droplet activation as a DSD broadening mechanism in simulations similar to the ones discussed here was discussed in Chapter 5 (HERNÁNDEZ PARDO et al., 2020). The role of broadening mechanisms in these simulations is further discussed in Section 6.2.3.1. For $N_a = 900$ cm^{-3}, N_c was significantly overestimated in most of the trajectories compared to the observations. The overestimation of N_c, given similar N_a and PSD shape as in the observations, may have been related to misrepresentations of aerosol properties, implicit in the hygroscopicity parameter, or to overestimation of the supersaturation with respect to the observations. The fact that the model consistently represented the distance above cloud base of the maximum q_c, while having higher N_c than in the observations and neglecting ice processes, indicates that DSD broadening mechanisms were more efficient in the model than in real clouds. However, this is in contrast with the results of the simulations with $N_a = 3000$ cm^{-3}, where values of N_c in the model were close to the observed ones, but the distance above cloud base of the q_c peak was overestimated with respect to the observations. If ice were included, the removal of q_c could be accelerated, further decreasing the height of maximum q_c. Therefore, including conversion from cloud water to ice could improve the representation of the height of maximum q_c in the $N_a = 3000$-cm^{-3} case, but worsen it in the $N_a = 900$-cm^{-3} case. In any case, the difference between the heights above cloud base of maximum q_c corresponding to an increase in N_a from 900 cm^{-3} to 3000 cm^{-3} was overemphasized in Bin compared to the ACRIDICON-CHUVA observations. Therefore, the enhanced efficiency of DSD broadening mechanisms in Bin$_c$ led to an overestimation of the aerosol effect in the model.

It is important to recognize that an exact correspondence between individual Ln trajectories and "observed" trajectories in Figure 6.12 cannot not be assumed. The latter consist of averaged observations that are assumed to correspond either the cloud base or the cloud top, based on the flight strategies during ACRIDICON-CHUVA, but without knowing the precise distance from the cloud lower and upper boundaries. Conversely, Ln trajectories were defined based on an objective criteria (distance from cloud top) in the model. Thus, the uncertainties associated with the

relative position of the flight paths has to be considered when comparing the model and the observations. For instance, at $h \sim 1$ km, DSDs in $L2$ model trajectories had lower q_c than DSDs in the observed trajectory (Figure 6.12). This could be interpreted as a result of including measurements from deeper clouds, so that the actual distance from the sampled region to cloud top was larger than 200 m in those observations. Note that, since the observed path included measurements from cloud base penetrations, it started at $h = 0$ km, while the model paths started almost 1 km above the cloud base because they contained only cloud-top information.

Figure 6.13 - Left panel: 100-m depth averaged DSDs in the observations. Right panel: averaged DSDs corresponding to ~ 200 m below the highest cloudy pixel in the simulations (i.e., $L2$ trajectories in Figure 6.12).

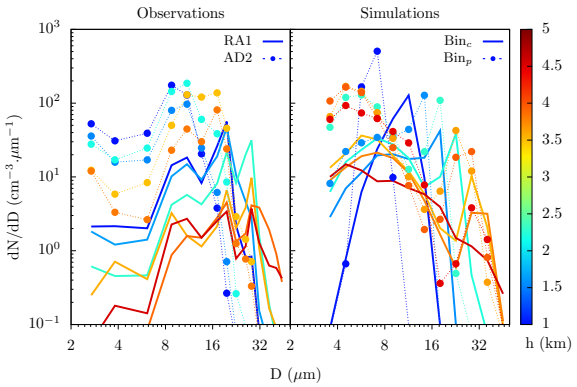

Nevertheless, even if an exact correspondence between individual DSDs from the model and from the observations cannot be assumed simply based on h, their overall trends can still be analyzed. Figure 6.13 illustrates the DSDs corresponding to several heights above cloud base in flights RA1 and AD2 and in the $L2$ trajectories of the Bin$_c$ and Bin$_p$ simulations. Overall, the model represented DSD broadening with h, in agreement with the observations. Multi-modalities in the averaged DSDs indicate the coexistence of growth processes and new droplet activation above cloud base in both the model and observations. While the evolution of the larger-size mode was consistent between the observed and modeled DSDs, there were notable differences in the characteristics of the smaller-size mode. At $h >\sim 1.5$ km, the smaller-size mode was more prominent in the modeled DSDs than in the observations, while the opposite occurred at $h <\sim 1.5$ km. Wide DSDs can result from a feedback between activation and collision-coalescence in nearly undiluted regions of the cloud, i.e., collision-coalescence enhances activation by decreasing N_c, while activation favor

collision-coalescence by augmenting the amount of droplets to be collected (Chapter 5). Therefore, the lack of observations in nearly undiluted cloud regions (see Section 6.1) may have affected the comparison between observed and modeled DSDs above $h =\sim 1.5$ km.

To compare the cloud-top DSDs shown in Figure 6.13 further, the corresponding values of D_m, σ and ϵ were calculated (Figure 6.14) Like in the observations, D_m and σ were inversely related to N_a for most values of h. The rate of change of D_m with height was similar in the observations and simulations, but D_m was smaller in Bin_c than in the corresponding observations (RA1), consistent with the overestimation of N_c discussed above. Conversely, the rate of increase of σ with height was much more intense in the simulations than in the observations, consistent with weaker (stronger) small-size mode in the former below (above) $h =\sim 1.5$ km, as shown in Figure 6.13. This explained the contrasting behavior of ϵ between the observations and the simulations, with ϵ increasing by a factor of ~ 4 from $h = 1$ km to $h = 4$ km in the simulations, but maintaining a constant value of ~ 0.3 above $h \sim$ 1-km in the observations. Like in the observations, the average profile of ϵ at cloud top was similar in both clean and polluted situations for the simulations. In the next section, it is shown that varying N_a between Bin_c and Bin_p simulations did not affect the value of ϵ at cloud base either.

Figure 6.14 - Mean diameter (D_m), standard deviation (σ) and relative dispersion (ϵ) corresponding to the averaged DSDs at cloud-top ($L2$ trajectories) in Bin_c and Bin_p simulations, and to 100-m depth averaged DSDs from flights RA1 and AD2.

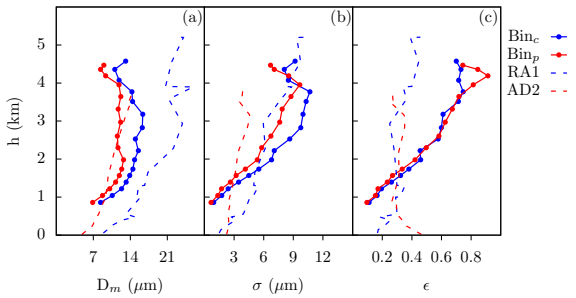

In Section 6.1.1 it was shown that, although the mean profiles of ϵ for clean and polluted observations were similar above cloud base, the underlying mechanisms determining its variability differed in both cases. In observations of cleaner cases (flights M1, RA1 and RA2), ϵ was strongly correlated with q_c/q_a as a results of

enhanced rain production by collision-coalescence. In the most polluted cases (AD flights), although rain production was delayed with respect to cleaner situations, relatively high values of ϵ were maintained due to the predominance of in-cloud droplet activation. In the next Section, the mechanisms determining the variability of DSD shape in Bin_c and Bin_p simulations is analyzed.

6.2.3.1 Variability of the DSD shape in the bin-microphysics simulations

Figure 6.15 illustrates values of ϵ along the $y = 0$-km cross-section in the Bin_c and Bin_p simulations. Spurious oscillations of DSD shape for values of ϵ smaller than ~ 0.15 were evident inside the cloud at all times. This was likely related to advection issues, such as the non-conservation of integral quantities of the DSDs when binned quantities are advected individually in Eulerian models (OVTCHINNIKOV; EASTER, 2009). However, the range of variation of ϵ was far greater than the amplitude of these oscillations. At earlier simulation times ($t \leq 12$ min), larger values of ϵ ($>\sim 0.4$) were located near the base and the top of the cloud. As the cloud developed, values of $\epsilon > 0.4$ also appeared in regions affected by entrainment and mixing near the lateral edges of the cloud. Isolines of equivalent potential temperature (θ_e) equal to 343 K and 346 K are represented by black continuous contours in Figure 6.15. Since θ_e is conserved in moist adiabatic motions, it can be used to analyze the degree of dilution of parcels rising from cloud base (i.e., smaller θ_e implies greater dilution because mid-tropospheric θ_e is smaller than θ_e at cloud base). It is seen that, at earlier times of cloud development, most of the cloud area was encompassed by the 343-K isoline (see first and second rows in Figure 6.15). However, at $t = 15$ min and $t = 18$ min a considerable fraction of the cloud area had $\theta_e < 343$ K, especially on the downwind side of the cloud near an altitude of 3-km. Large values of ϵ (> 0.4) occurring in this area suggest the effects of dilution and mixing in broadening the DSDs. A more detailed assessment of such effects in similar simulations is presented in Chapter 5. At $t = 18$ min, the largest values of ϵ were located near the cloud top ($\sim 4 - 6$ km altitude), consistent with rain initiation at the higher levels inside the cloud. In Bin_p, the largest values of ϵ near the cloud top at $t = 18$ min were mainly restricted to diluted regions (i.e., regions with $\theta_e < 343$ K). In contrast, at $t = 18$ min in Bin_c, large cloud-top values ($\epsilon > 0.5$) also occurred within the area encompassed by the 343-K isoline, i.e. relatively undiluted cloud regions. This is consistent with enhanced rain production in the clean case. As discussed in Chapter 5, for a clean cumulus cloud simulated with a similar set-up as in this study, collision-coalescence is primarily triggered in nearly undiluted cloud cores, associated with relatively high droplet concentrations compared to more diluted cloud regions, in agreement with

Khain et al. (2013).

Figure 6.15 - Relative dispersion (ϵ, color scale) and wind velocity (vectors) at the y = 0 km cross-section in Bin simulations. The think and thin black continuous contours represent isolines of equivalent potential temperature (θ_e) equal to 343 K and 346 K, respectively.

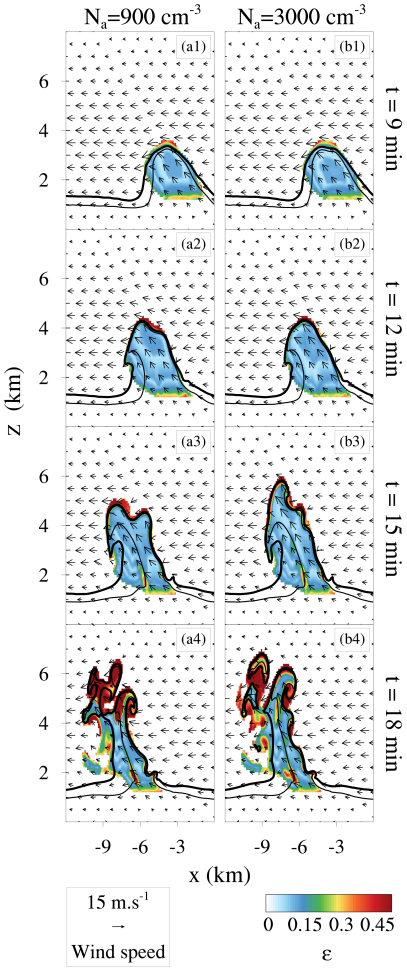

To limit the effects of the spurious oscillations of DSD shape mentioned above on the variability of ϵ, the mean DSDs was calculated in cubic boxes consisting of $5 \times 5 \times 5$ grid points throughout the domain. Figure 6.16 illustrates the values of ϵ and ΔD_{99} corresponding to the box-mean DSDs over 500-m height and 0.1 q_c/q_a intervals. In both clean and polluted situations, ϵ tended to increase with decreasing q_c/q_a, except at cloud base (Figure 6.16a,c). The role of collision-coalescence and rain production on the distribution of ϵ in the $h - q_c/q_a$ space is confirmed by the values of ΔD_{99}. $\Delta D_{99} >\sim 20$ above 3-km depth (Figure 6.16b,d) coincided with the largest values of ϵ (> 0.5) in Figure 6.16a,c. This indicates that, as h increased, the DSDs

were broadened toward the right side of the size spectrum, leading to precipitation production and thus decreasing q_c/q_a after sedimentation. Accordingly, the largest differences between the Bin_c and Bin_p simulations were found at the highest cloud levels. More efficient conversion from cloud water to rain in Bin_c implied a more efficient concentration of the wider DSDs toward smaller q_c/q_a values compared to Bin_p.

Figure 6.16 - Relative dispersion (ϵ) and difference between the diameters of the 99^{th} and 50^{th} percentiles of the DSD (ΔD_{99}) corresponding to mean DSDs every $5 \times 5 \times 5$ grid-points boxes in Bin_c and Bin_p simulations. Displayed values correspond to averaged ϵ and ΔD_{99} at each 500-m h and 0.1 q_c/q_a intervals.

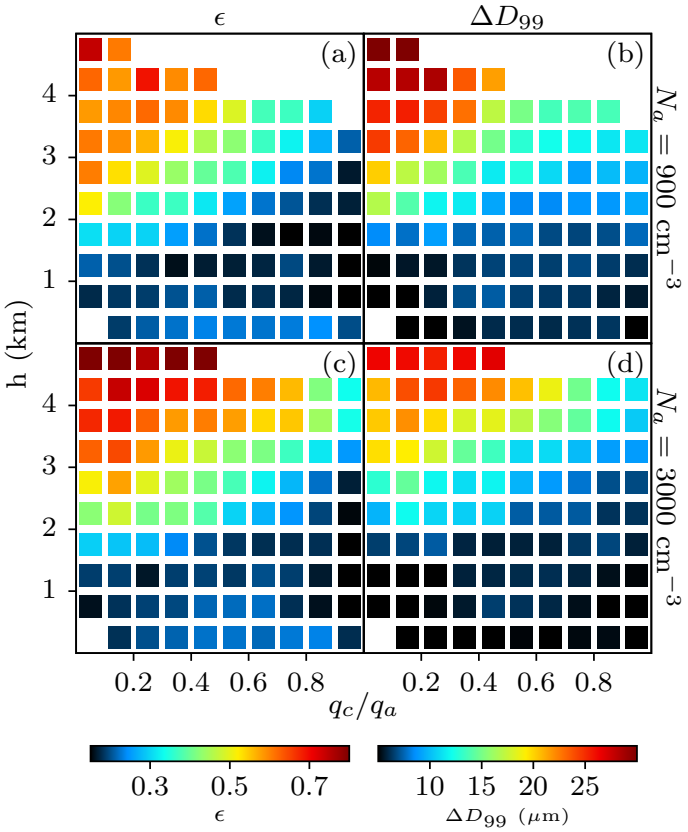

The pattern of relatively large ϵ in the observations for the polluted cases, coinciding with smaller ΔD_{99} compared to the clean cases, suggests DSD broadening toward small sizes due to enhanced droplet activation. This was to some extent reproduced by the model. Note that ϵ reached larger values in Bin_p than in Bin_c. Also, the area occupied by ϵ values larger than a given threshold (for instance, $\epsilon > 0.4$) in the $h - q_c/q_a$ space was larger in Bin_p than in Bin_c, i.e., the range of q_c/q_a and h values

corresponding to broad DSDs increased as N_a increased. Conversely, the maximum value of ΔD_{99} was smaller in Bin_p than in Bin_c, and the height above cloud base at which ΔD_{99} surpassed certain value (e.g., 20 μm) increased from Bin_c to Bin_p. This indicates that, at a given h, the contribution of larger droplets to ϵ decreased as N_a increased. Therefore, the increase of ϵ with increasing N_a is associated with an enhancement in the amount of small droplets, in agreement with the observations. Additional analysis for individual simulation times (not shown) indicates that this mechanism was accentuated near cloud top (consistent with the analysis of the cloud-top DSDs in Section 6.2.3), which explains its occurrence in the observations. However, as shown in Figure 6.13, the small mode of the DSDs near cloud top was more prominent in the model than in the observations. This may have been a result of including nearly undiluted cloud cores in the model analysis that were mostly absent in the observations, as well as of an overestimation of collision-coalescence and in-cloud activation rates in the model. On the other hand, the values of ϵ at cloud base in the simulations were not significantly affected by changing N_a, in contrast to the observations. This might be related to neglecting the solute and curvature effects in the condensation calculations, or assuming the same PSD shape and hygroscopicity in both Bin_c and Bin_p simulations. As shown by Pöhlker et al. (2016), Pöhlker et al. (2018), changes in N_a over the Amazon are associated with different aerosol sources, and thus likely the aerosol particle populations have different size and chemical properties as well.

Figure 6.17 shows the average rate of collision-coalescence (CCrate_c), activation (ACTrate) and condensation (CONDrate) of cloud droplets as a function of h and q_c/q_a. CCrate_c represents the total number concentration of droplets ($D < 50$ μm) collected per second. ACTrate is the ratio of the total number concentration of droplets activated per second to the initial N_a. CONDrate indicates the rate of change of the mean droplet size due to diffusion of water vapor to/from cloud droplets. It is seen that CCrate_c behaved similarly in Bin_c and Bin_p simulations, with a maximum at large q_c/q_a values and relatively high heights above cloud base. Note that, although the number of collected droplets was similar in both simulations, the mass transferred from small to large drops during collision-coalescence depends on the collected droplet size. Since droplets were larger on average in Bin_c, mass transfer rates from collision-coalescence were generally larger in Bin_c compared to Bin_p. This is evidenced by the faster decrease of q_c/q_a in Bin_c. Examination of CCrate_c provides further support for the mechanism mentioned earlier, in which the increase in rain production in nearly undiluted cloud-core regions leads to a concentration of the broader DSDs at low q_c/q_a values, as a direct function of h. As

collision-coalescence rates increase with increasing h, the consequent reduction in N_c increases the supersaturation, subsequently enhancing in-cloud droplet activation and condensation too. Large ACTrate and CONDrate occurred at most q_c/q_a values above $h = 3 - 4$ km. In general, larger values of ACTrate and CONDrate in Bin_p compared to Bin_c are consistent with an enhanced contribution of smaller droplets to increases in ϵ in Bin_p, as discussed above. At $h <\sim 3$ km, ACTrate and CONDrate were inversely related to q_c/q_a. At these heights, the dilution occurring at the edges of the cloud was the main factor affecting q_c/q_a. Thus activation and condensational growth in diluted regions of the cloud were the main mechanisms increasing ϵ for $h <\sim 3$ km in the simulations (i.e., at levels where collision-coalescence is weaker), leading to DSD broadening toward the left and right sides of the size spectrum, respectively.

Figure 6.17 - Similar to Figure 6.16 but for the rate of collision-coalescence (CCrate_c), activation (ACTrate) and condensation (CONDrate) of cloud droplets.

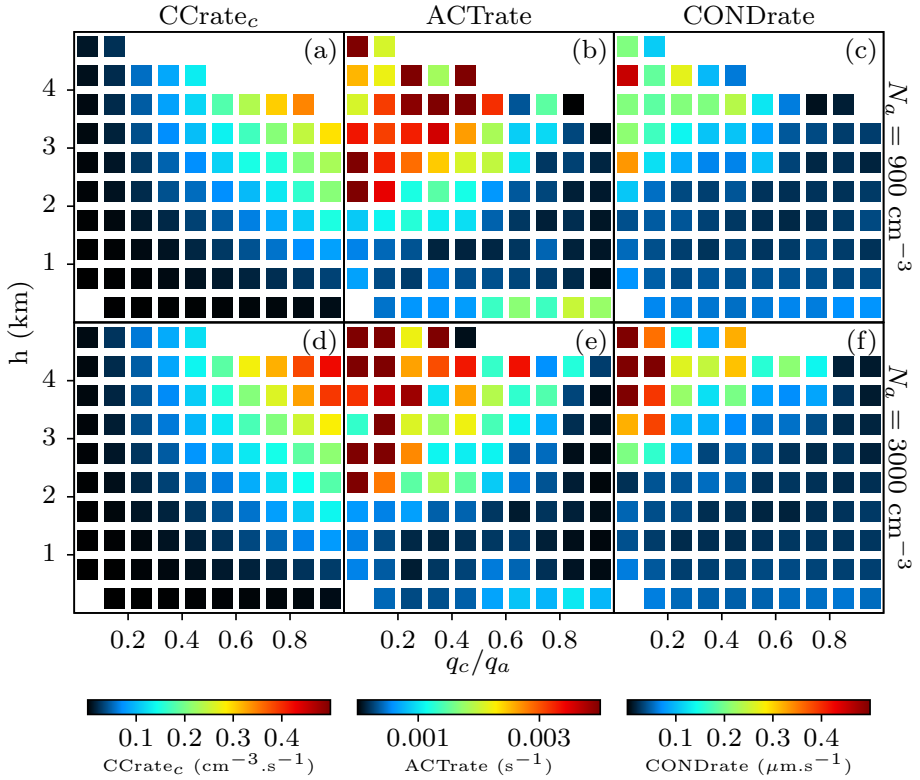

The analysis of the simulations supports the idea that ϵ increases with decreasing q_c/q_a either due to entrainment, dilution and mixing near the cloud edges, or due to precipitation production in nearly undiluted cloud cores. However, the depen-

dence of ϵ on h was stronger in the simulations than in the observations (Figures 6.14 and 6.16), with ϵ being larger (smaller) in the observations than in the model below (above) ~ 1 km. The underestimation of ϵ at low h in the model may have been associated with an under-representation of entrainment and dilution at early cloud stages and low levels above cloud base. As shown in Figure 6.17 activation and condensation were maximum at $q_c/q_a < 0.1$ at low levels (i.e, nearly diluted regions). Mixing of parcels undergoing different condensation/activation paths can ensure DSD broadening in clouds (GRABOWSKI; ABADE, 2017). Thus, increasing entrainment and dilution at levels close to the cloud base could improve comparison with the observations. On the other hand, the overestimation of ϵ at $h > 1$ km in the model may have been related to excessive collision-coalescence, which led to DSD broadening toward large droplet sizes and also toward small sizes through its feedback on the rate of droplet activation. The absence of ice processes as a sink of q_c at higher levels in the simulations, as well as the lack of measurements at nearly undilute cloud areas, might be additional factors explaining differences in ϵ between the model and observations. Further research including different models, as well as observations of several levels inside convective clouds would be beneficial for a better understanding of the variability of ϵ in cumulus clouds.

Although physical processes typical of cumulus clouds determine a clear correlation between DSD shape and the degree of deviation of q_c from q_a, expressing ϵ (or μ) as a function of q_c/q_a involves significant uncertainties. Results from Bin simulations here suggest that the correlation between μ and q_c/q_a change with h (i.e., in-cloud processing). Nevertheless, considering the relationship between μ and q_c/q_a represents an improvement compared to other parameterizations commonly used in double-moment bulk schemes that are based on N_c only (see Section 6.1). Following the impact of including the relationship $\mu = f(q_c/q_a)$ in the parameterization of M09 is discussed, for analogous simulations as in the Bin tests above.

6.2.4 Impact of changes in the shape parameter in the bulk-microphysics simulations

In Section 6.2.2 it was shown that Bulk_0 simulations, based on the double-moment microphysics scheme of M09 (with the modifications described in Section 6.2.1) differed significantly from Bin simulations. Specifically, it was shown that rain production was more efficient in Bulk_0 than in Bin. Considering that DSD broadening mechanisms were generally more efficient in Bin simulations than in the observations, it follows that rain production was overestimated in Bulk_0 to an even larger

extent.

Figure 6.18 - Similar to Figure 6.12 but for the Bulk simulations.

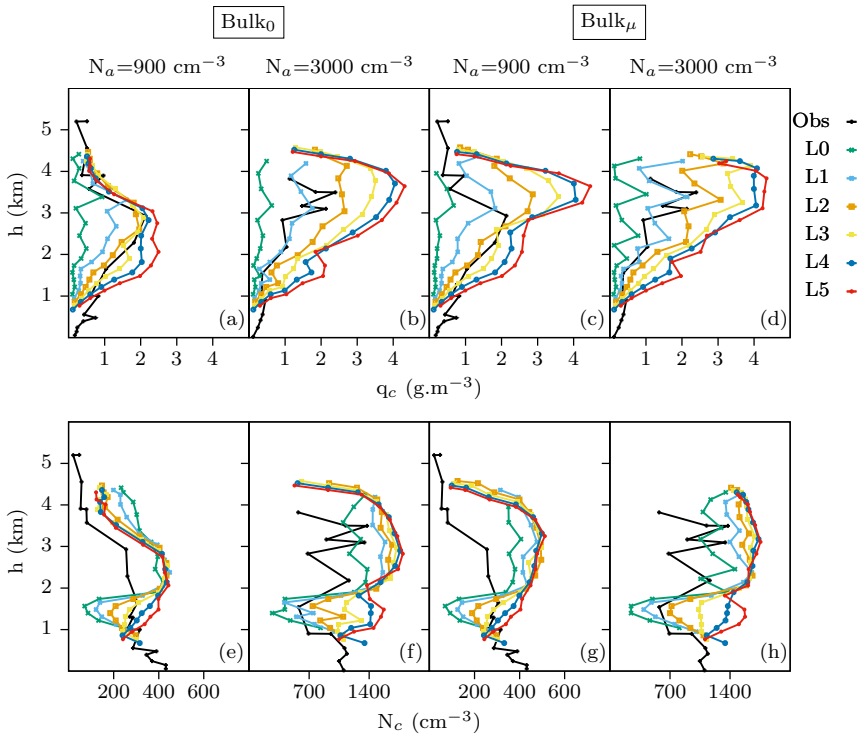

Figure 6.18 shows that Bulk$_0$ provided a good estimation of the distance above cloud base of maximum q_c at cloud top in both clean and polluted situations, compared to the Bin simulations and the observations. However, as in Bin$_c$ simulations, N_c was overestimated with respect to the observations, which indicates overestimation of the efficiency of cloud-water-to-rain conversions in the model. Another aspect indicating an overestimation of the rain-production efficiency in Bulk compared to the observations is the assumption of a larger threshold diameter separating cloud droplets from rain drops in the former (i.e., 80 μm in Bulk, versus 50 μm in the observations). If the efficiency of cloud-water-to-rain conversion were similar in the model and the observations, droplets would remain in the cloud-water category for longer times in Bulk simulations than in the observations, due to the larger threshold diameter in the former, thus reaching the q_c-maximum at higher h than in the observations. In contrast, applying the μ_4 formulation in Bulk$_\mu$ led to delayed precipitation development, especially in the simulations with $N_a = 900$ cm^{-3}. This effect was less evident in the simulations with $N_a = 3000$ cm^{-3}, consistent with less rain production in that case.

Figure 6.19 - Mean profiles of the shape parameter (μ) and the droplet collision-coalescence rate (CCrate_c) in Bin and Bulk simulations.

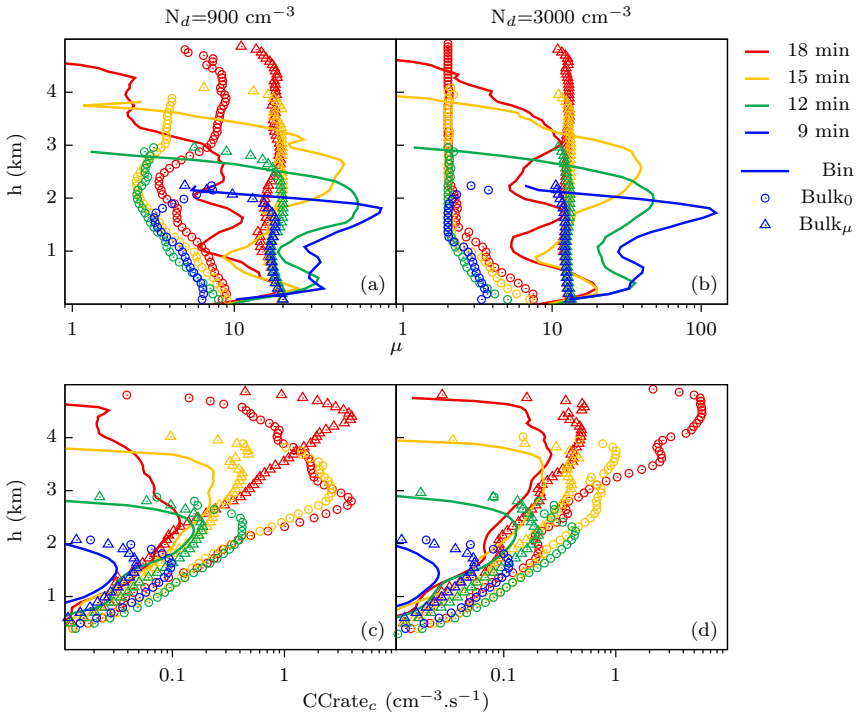

The mean profiles of μ from each simulation are illustrated in Figure 6.19a,b. It is seen that the mean profile of μ in Bulk_μ was generally closer to the Bin profile, compared to Bulk_0. Note that an upper limit for μ of 20 was applied in Bulk_μ, while in Bulk_0 μ had a lower limit of 2 and an upper limit of 10. As the simulation time increased, both bulk schemes tended to overestimate μ compared to the bin scheme near the cloud top. However, that behavior had different implications for each μ approach.

In Bulk_0, μ was inversely related to N_c; thus the reduction of N_c from the cloud core to cloud edge led to increasing μ toward the cloud boundaries. This was evident in the upper third of the cloud at all times in Bulk_0, related to the decrease of N_c toward the cloud top, at levels above the height of maximum N_c (see Figure 6.11). The local minimum of μ near $h = 5$ km, at $t = 18$ min in the Bulk_{0c} simulation was associated with a local increase of N_c due to cloud-top droplet activation. Although the $\mu - N_c$ relationship employed by M09 might represent inter-cloud variability in certain situations (as it follows from the observations reported by Martin et al. (1994)), it is generally inconsistent with the intra-cloud variability found in the observations and the Bin simulations here. Results from analysis of the observations

and Bin simulations indicate that variations of μ within a single cloud can be larger than variations among clouds in different environments.

The $\mu - q_c/q_a$ relationship employed in Bulk$_\mu$ (i.e, μ_4) provides a better approximation of the intra-cloud variability of μ than previous parameterizations. Besides being closer to Bin on average, μ_4 reproduces the increase in DSD width toward the cloud edges, for instance, the mean profile of μ in Bulk$_\mu$ simulations consistently represented the decrease of μ at cloud top at all times. The overestimation of μ at upper levels mentioned above was a consequence of delayed rain initiation in Bulk$_\mu$ compared to Bin, consistent with larger N_c in the former.

Figure 6.19c,d shows average profiles of CCrate$_c$ in the simulations. CCrate$_c$ from the bulk schemes was calculated as the change in N_c due to autoconversion, accretion and selfcollection. It accounted for two droplets in case of selfcollection (collision of two droplets resulting in a droplet that is bigger than the original two, but not as big as to be considered a rain drop) or autoconversion (collision of two droplets forming a rain drop), and for one droplet in case of accretion (collision of one rain drop and one cloud droplet, resulting in a bigger rain drop). Note that the method of Seifert and Beheng (2006) for parameterizing these processes in Bulk considers a threshold diameter separating clouds droplets and rain of 80 μm, while in Bin, CCrate$_c$ was diagnosed from the total number of colliding droplets smaller than 50-μm diameter. It was verified here that increasing the threshold diameter from 50 μm to 80 μm had negligible impact on CCrate$_c$ for $t < 15$ min in Bin simulations, due to the predominance of small droplets in early stages of cloud development. With the increase in droplet sizes later in the simulations, the choice of the threshold diameter became important. Assuming a 50 μm threshold diameter in Bin, at $t > 15$ min, can overemphasize the differences between Bin's and Bulk's CCrate$_c$ values. Nevertheless, the threshold diameter in Bin was maintained here as 50 μm for consistency with the comparison between Bin and CDP measurements in Section 6.2.3.1.

At all times, CCrate$_c$ was lower in the Bin simulations (Figure 6.19c,d), consistent with the larger values of μ (i.e., narrower DSDs) in Bin compared with Bulk simulations. The high rate of collision-coalescence in Bulk$_0$, associated with $\mu \leq 10$, compensated for the larger N_c produced by the bulk scheme, compared to the Bin simulations and the observations (see Section 6.2.2 and Figure 6.18). This explains why Bulk$_0$ provided a good estimation of the height above cloud base of maximum q_c compared to the observations, and an earlier rain initiation compared to Bin, despite having much higher N_c (and therefore smaller mean droplet sizes). Increas-

ing μ from Bulk$_0$ to Bulk$_\mu$ improved the estimation of CCrate$_c$, thus increasing the height above cloud base of maximum q_c. At $t = 18$ min in Bulk$_{\mu c}$, CCrate$_c$ increased with height for $h > 3$ km, in contrast with Bulk$_0$ and Bin. This was a consequence of the persistence of cloud water in Bulk$_\mu$, whereas conversion from cloud water to rain predominated in Bulk$_0$ and Bin, especially when $N_a = 900$ cm^{-3}.

Figure 6.20 - Difference between the values of the droplet collision-coalescence rate (CCrate$_c$) in Bulk and Bin simulations (error=CCrate$_c$(Bulk)−CCrate$_c$(Bin)) for intervals of cloud water content (q_c) and cloud droplet number concentration (N_c) up to $t = 12$ min.

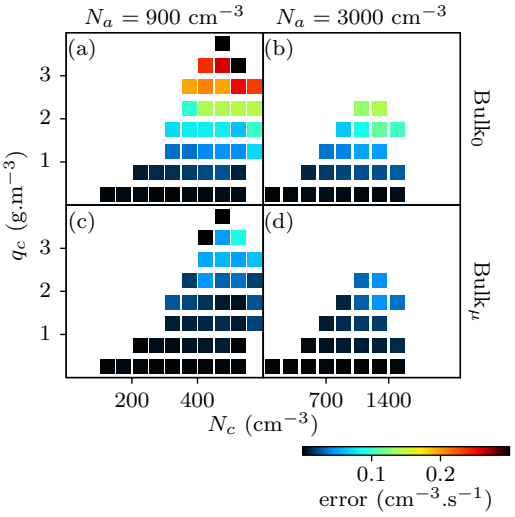

It has been shown here that CCrate$_c$ was generally larger in the Bulk simulations compared to the Bin simulations. However, because CCrate$_c$ expresses the number of collision events, it increases with increasing N_c, for similar values of D_m and σ and similar collision efficiency. Therefore, the difference in N_c among simulations should be considered in this discussion. Figure 6.20 shows the difference between the values of CCrate$_c$ in Bulk and Bin simulations (error=CCrate$_c$(Bulk)−CCrate$_c$(Bin)) for intervals of q_c and N_c up to $t = 12$ min. This indicates that, for a given interval of N_c and q_c, adopting μ_4 in Bulk$_\mu$ led to clear improvements in the estimation of CCrate$_c$ compared to Bulk$_0$. A similar tendency to decrease the error is observed at all times, but this effect is illustrated only at the earliest simulation times when the effect of the threshold diameter difference between CCrate$_c$ calculated from Bin and Bulk was minimum.

These tests illustrate a clear case of compensation of errors in simulations with

bulk microphysics. Specifically, it is shown that the impact of the overestimated N_c on rain development, in Bulk_0, was balanced out by an overestimation of the collision-coalescence rate, related to the assumption of excessively broad DSDs. In turn, including larger values of μ (i.e., narrower DSDs) in Bulk_μ improved the representation of the collision-coalescence, evidencing the effect of the erroneous N_c.

6.3 Remarks

This study addressed the intra-cloud and inter-cloud variability of droplet size distribution shape in observations and numerical simulations of cumulus clouds, with emphasis on the dependence of DSD broadening mechanisms on the background aerosol concentration. Observations from the ACRIDICON-CHUVA campaign were compared with results from idealized simulations of an isolated cumulus cloud using bin and bulk microphysics parameterizations. Factors impacting the spatial distribution of the spectral dispersion of droplets in cumulus clouds, especially height above cloud base, adiabaticity and aerosol loading (KHVOROSTYANOV; CURRY, 1999; KHVOROSTYANOV; CURRY, 2008), were explored in the observations and the bin-microphysics simulations. Prospective relationships for diagnosing the shape parameter of the droplet gamma size distribution for use in bulk-microphysics models were discussed.

Relatively clean clouds ($N_a < 900$ cm^{-3}), developed over maritime or remote rainforest regions, showed a strong relationship between ϵ and q_c/q_a. The bin-microphysics simulations indicated that this behavior is primarily caused by collision-coalescence, which simultaneously increases ϵ and decreases q_c through rain production. In the observations, the strengthening of collision-coalescence was indicated by an increase in the tail of the DSDs with height above cloud base. At lower levels, DSDs with relatively large relative dispersion ($\epsilon \sim 0.3 - 0.4$) and short tails ($\Delta D_{99} \sim 12$ μm), for $q_c/q_a < 0.5$, were likely associated with the existence of high activation and condensation rates in diluted parcels near the cloud edges. This way, the inverse relationship between ϵ and q_c/q_a was sustained in both diluted and nearly undiluted regions of clean clouds.

Polluted clouds ($N_a > 2000$ cm^{-3}), observed over deforested regions, showed a smaller variability of droplet size distribution shape, with a weaker dependence on q_c/q_a. This is consistent with a lower rate of collision-coalescence and delayed rain production in polluted clouds compared with cleaner clouds. Large DSD relative dispersion values ($\epsilon \sim 0.3 - 0.4$) coinciding with short tails ($\Delta D_{99} \sim 8$ μm) occurred at most levels and values of q_c/q_a in the observations. This was likely caused by

enhanced droplet activation throughout the cloud. A similar effect occurred in the bin simulations, with a tendency to increase ϵ and to decrease ΔD_{99} for higher N_a. This was associated with an increase in the rate of in-cloud droplet activation and a decrease in droplet growth rate by collision-coalescence.

In general, the variability of ϵ was larger in the bin simulations than in the observations. An inverse relationship between ϵ and q_c/q_a was evident at most levels above cloud base in both polluted ($N_a = 3000$ cm^{-3}) and cleaner ($N_a = 900$ cm^{-3}) simulations. However, while the slope of the $\epsilon - q_c/q_a$ relationship was approximately the same at all h in the observations, it notably increased (in absolute value) with h in the simulations. One factor that could impact this comparison is the fact that all measurements performed above the cloud base in the observations corresponded to levels near the top of the clouds. Nevertheless, additional analysis showed that a pronounced increase of this slope with h also occurred when only the upper 500 m of the cloud at each simulation time was considered. Therefore, this behavior suggests that spectral broadening mechanisms may have been too efficient in the model compared to the observed clouds. Comparison of the cloud-top evolution showed that the location of the maximum cloud water content was consistent between the simulations and observations, despite the larger N_c and the lack of ice in the former (note that the presence of ice particles above the freezing level in these observations was reported by Cecchini et al. (2017)). An overestimation of the spectral broadening at the higher levels in the simulations may have been related to excessive collision-coalescence, as well as to spurious mechanisms, such as the numerical diffusion in mass/size space associated with the combination of condensational growth with advection in physical space (MORRISON et al., 2018; HERNÁNDEZ PARDO et al., 2020). Additionally, an underestimation of entrainment and dilution at early stages of cloud development and low levels above cloud base could explain narrower droplet spectra at the lower levels in the model compared to the observations. Narrower spectra at lower levels and broader spectra at upper levels led to a larger variation of the relative dispersion with height in the model than in the observations. Further research including the representation of mixed-phase processes in the simulations and different models, as well as observations from several levels inside convective clouds, would be beneficial for a better understanding of the variability of droplet size distribution shape in cumulus clouds.

It was shown here that considering the dependence of ϵ on q_c/q_a led to an improvement compared to previous parameterizations that diagnose ϵ from N_c, at least for $N_a \leq 900$ cm^{-3}. Applying the new approach in bulk-microphysics simulations of an

isolated cumulus improved collision-coalescence rates compared to bulk simulations that diagnosed the relative dispersion based on N_c. Future work to evaluate the impact of these approaches further in cloud-resolving simulations is planned.

7 CONCLUSIONS

This research is intended to contribute to improving existing knowledge on the performance of microphysics parameterizations for representing warm-phase cloud processes, including aerosol-cloud interactions, in convective clouds. To this end, the roles of warm-phase microphysical processes in idealized-simulations of convective clouds were analyzed in detail, taking advantage of in-situ measurements obtained as part of the ACRIDICON-CHUVA field campaign near the Amazon basin.

The first part of this research work explored cloud sensitivities to changes in aerosol properties, such as total number concentration, size distribution and composition. This analysis focused on the droplet number concentration and effective diameter at the top of a shallow cumulus simulated with a bin-microphysics single-column model, for initial conditions typical of the Amazonian region. The impact of considering bin versus bulk PSDs was evaluated, in order to investigate the influence of entrainment and activation scavenging on the derived sensitivities.

The responses of simulated cloud-top DSDs to changes in the aerosol parameters showed a pronounced dependency on the model assumptions regarding the entrainment and the evolution of the aerosol size distribution, which modulated the depletion of aerosols and supersaturation in the modeled cloud. In simulations with bin PSDs, the rate of activation at a certain time had a strong impact on the intensity of the activation afterwards, due to a faster depletion of aerosols in the right tail of the PSDs, generating distinctive regimes in the sensitivity of cloud-top DSDs to aerosols. In turn, the assumption of bulk PSDs determined a slower depletion of activable aerosols in the simulations, leading to more uniformly distributed responses to changes in the aerosol properties than in simulations with bin PSDs and being consistent with the results of Feingold (2003), Reutter et al. (2009) and Ward et al. (2010). Nonetheless, it was shown that for all the model configurations tested, the sensitivities of cloud-top DSDs to the aerosol parameters depended on the position within the multidimensional space defined by all the aerosol parameters analyzed, especially on the value of $\bar{r}_a$. This implies that cloud sensitivities cannot be fully described by supersaturation-based regimes (REUTTER et al., 2009).

A second study assessed the role of different DSD broadening mechanisms in bin microphysics parameterizations using idealized 2D and 3D Weather Research and Forecasting model simulations of an isolated warm cumulus cloud. It was shown that the modeled DSD evolution was strongly affected by collision-coalescence, reflecting the rapid drop growth that occurs once embryo raindrops are generated. The

reduction in droplet number mixing-ratio from collision-coalescence also induced droplet activation in regions of strong ascent and high supersaturation within the cloud core. Thus, collision-coalescence broadened the DSDs to large sizes directly, and to small sizes from the subsequent in-cloud droplet activation. Turbulent eddies enhanced DSD broadening near cloud top by influencing entrainment and DSD mixing processes, while evaporation played only a minor role in DSD evolution and sedimentation had little effect. Droplet activation, especially along the cloud top, led to DSD broadening to small sizes and $\sigma > 10$ μm. This activation was associated with cloud dilution, which reduced the droplet number mixing-ratio locally, thus increasing the supersaturation. Locally higher supersaturation, associated with reduction in the droplet number mixing-ratio from dilution in entrainment regions, also led to stronger condensational growth when this air ascended in the updraft, generating broad DSDs after mixing with DSDs from the less dilute cloud core. This result is consistent with the idea of "eddy hopping" as a DSD broadening mechanism, whereby DSDs undergoing different growth histories are broadened by their mixing (COOPER, 1989; GRABOWSKI; ABADE, 2017; ABADE et al., 2018).

Impacts on the overall DSD features with increasing the model resolution were generally small, but there was a noticeable decrease in σ and ΔD_{99} in the lower part of the cloud (below about 2.5 to 3 km) with decreased *vertical* grid spacing in all of the tests. This sensitivity of DSD width to the model vertical resolution is a signature of DSD broadening from vertical numerical diffusion, a non-physical feature detailed in Morrison et al. (2018). However, above 2.5 km there was little sensitivity to vertical grid spacing, which was likely due to the dominant role of other processes in DSD broadening, especially horizontal mixing. Thus, while there was a signature of artificial DSD broadening from numerical diffusion associated with vertical advection, the overall evolution of DSD width in this case was dominated by other physical mechanisms, particularly collision-coalescence, in-cloud droplet activation, and dilution, above ~ 2.5 km.

The third part of this research presented an analysis of the spatial distribution of ϵ within observed and modeled convective clouds. Factors impacting the spatial distribution of the spectral dispersion of droplets, especially height above cloud base, adiabaticity and aerosol loading were investigated. Relatively clean clouds ($N_a < 900$ cm^{-3}) showed a strong relationship between ϵ and q_c/q_a. The bin-microphysics simulations indicated that this behavior is primarily caused by collision-coalescence, which simultaneously increases the relative dispersion and decreases the cloud water content through rain production, and by in-cloud activation

and condensation in diluted parcels near the cloud edges. Observations of polluted clouds ($N_a > 2000$ cm^{-3}) showed a smaller variability of droplet size distribution shape, with a weaker dependence on q_c/q_a. This is consistent with less efficient collision-coalescence and enhanced in-cloud droplet activation in polluted clouds compared with cleaner clouds. A similar effect was reproduced in the bin simulations, with a tendency to increase ϵ and to decrease ΔD_{99} for higher aerosol concentrations, associated with an increase in the rate of in-cloud activation and a decrease in droplet growth rate by collision-coalescence.

Comparison between bin- and bulk-microphysics simulations and observations suggested that spectral broadening mechanisms were too efficient in the model with respect to the observed clouds, compensating for the overestimation of the droplet concentration in the former. In bin parameterizations, this may have been related to an excessive collision-coalescence, as well as to spurious mechanisms, such as the numerical diffusion in mass/size space associated with the combination of condensational growth with advection in physical space mentioned above (MORRISON et al., 2018). On the other hand, in bulk schemes, excessive rain production resulted from an erroneous representation of the intra-cloud variability of the shape parameter of gamma DSDs. It is shown that considering the dependence of μ on q_c/q_a represents an improvement compared to parameterizations that diagnose μ based on N_c, at least for $N_a \leq 900$ cm^{-3}. Applying the former approach in bulk-microphysics simulations of an isolated cumulus was found to improve the estimation of the collision-coalescence rate compared to bulk simulations that assume a dependence of μ on N_c.

The proposed $\mu - q_c/q_a$ relationship empirically accounts for the effects of the most important broadening mechanisms in cumulus clouds, without making any assumptions regarding adiabaticity like previously derived formulations. One drawback of using q_c/q_a to diagnose μ in bulk-microphysics models is that it requires accurate representations of intra-cloud variations in q_c, as well as of the cloud base temperature and pressure, thus depending on the model resolution. Nonetheless, the simplicity of this formulation allows its application in single-moment bulk microphysics schemes, which are computationally cheaper. The tradeoff of increasing the model resolution while decreasing the amount of moments predicted by the microphysics scheme, but using a better description of the shape parameter, versus employing lower resolutions with two-moment microphysics and a poorer description of μ should be carefully considered.

The analysis and interpretation of the simulations in this research work allowed to infer details regarding the evolution of DSDs in an Eulerian model with bin microphysics. An emerging approach in microphysical modeling is the Lagrangian particle-based approach, in which the hydrometeor population is represented by a sampling of point particles (often called "super-droplets") that move following Lagrangian trajectories in the Eulerian modeled flow (SHIMA et al., 2009; SöLCH; KäRCHER, 2010; RIECHELMANN et al., 2012; UNTERSTRASSER et al., 2017; GRABOWSKI et al., 2018; JARUGA; PAWLOWSKA, 2018; SEIFERT et al., 2019; DZIEKAN et al., 2019). This approach presents a much different methodology than Eulerian bin microphysics (GRABOWSKI et al., 2019). It would be useful to compare how DSDs evolve in Lagrangian particle-based versus bin schemes. This has been done for idealized simulations of a laboratory chamber (GRABOWSKI, 2020), and work is planned to extend this effort to simulations of a cumulus cloud. Although Lagrangian schemes have limitations related to the finite number of superdroplets that can be used, they do not have any numerical diffusion of DSDs. Therefore, such a comparison will be especially useful for evaluating the effects of numerical diffusion in bin schemes within Eulerian models, which is key for studies of aerosol-cloud interactions, warm rain production and effects of turbulence, entrainment and mixing in clouds.

REFERENCES

ABADE, G. C.; GRABOWSKI, W. W.; PAWLOWSKA, H. Broadening of cloud droplet spectra through eddy hopping: turbulent entraining parcel simulations. **Journal of the Atmospheric Sciences**, v. 75, n. 10, p. 3365–3379, 2018. 9, 67, 71, 110

ALBRECHT, B. A. Aerosols, cloud microphysics, and fractional cloudiness. **Science**, v. 245, n. 4923, p. 1227–1231, 1989. 2, 3, 75, 82

ALTARATZ, O.; KOREN, I.; REISIN, T.; KOSTINSKI, A.; FEINGOLD, G.; LEVIN, Z.; YIN, Y. Aerosols' influence on the interplay between condensation, evaporation and rain in warm cumulus cloud. **Atmospheric Chemistry and Physics**, v. 8, n. 1, p. 15–24, 2008. 31

ANDERSON, T.; ACKERMAN, A.; HARTMANN, D.; ISAAC, G.; KINNE, S.; MASUNAGA, H.; NORRIS, J.; PöSCHL, U.; SCHMIDT, K.; SLINGO, A.; TAKAYABU, Y. Temporal and spatial variability of clouds and related aerosols. In: CHARLSON, R. J.; HEINTZENBERG, J. (Ed.). **Clouds in the perturbed climate system: their relationship to energy balance, atmospheric dynamics, and precipitation**. Cambridge, MA, USA: MIT Press, 2009. p. 127–147. 7

ANDREAE, M. O.; AFCHINE, A.; ALBRECHT, R.; HOLANDA, B. A.; ARTAXO, P.; BARBOSA, H. M. J.; BORRMANN, S.; CECCHINI, M. A.; COSTA, A.; DOLLNER, M.; FÜTTERER, D.; JÄRVINEN, E.; JURKAT, T.; KLIMACH, T.; KONEMANN, T.; KNOTE, C.; KRÄMER, M.; KRISNA, T.; MACHADO, L. A. T.; MERTES, S.; MINIKIN, A.; PÖHLKER, C.; PÖHLKER, M. L.; PÖSCHL, U.; ROSENFELD, D.; SAUER, D.; SCHLAGER, H.; SCHNAITER, M.; SCHNEIDER, J.; SCHULZ, C.; SPANU, A.; SPERLING, V. B.; VOIGT, C.; WALSER, A.; WANG, J.; WEINZIERL, B.; WENDISCH, M.; ZIEREIS, H. Aerosol characteristics and particle production in the upper troposphere over the Amazon basin. **Atmospheric Chemistry and Physics**, v. 18, n. 2, p. 921–961, 2018. Available from: <https://www.atmos-chem-phys.net/18/921/2018/>. 3, 7

ANDREAE, M. O.; ROSENFELD, D.; ARTAXO, P.; COSTA, A. A.; FRANK, G. P.; LONGO, K. M.; SILVA-DIAS, M. A. F. Smoking rain clouds over the Amazon. **Science**, v. 303, n. 5662, p. 1337–1342, 2004. 2, 3

ANTTILA, T.; KERMINEN, V.-M. On the contribution of Aitken mode particles to cloud droplet populations at continental background areas – a parametric sensitivity study. **Atmospheric Chemistry and Physics**, v. 7, n. 17, p. 4625–4637, 2007. 30

AYALA, O.; ROSA, B.; WANG, L.-P. Effects of turbulence on the geometric collision rate of sedimenting droplets. Part 2. theory and parameterization. **New Journal of Physics**, v. 10, n. 7, p. 075016, jul 2008. 10

AYALA, O.; ROSA, B.; WANG, L.-P.; GRABOWSKI, W. W. Effects of turbulence on the geometric collision rate of sedimenting droplets. Part 1. results from direct numerical simulation. **New Journal of Physics**, v. 10, n. 7, p. 075015, jul 2008. 10

BAKER, M. B.; BREIDENTHAL, R. E.; CHOULARTON, T. W.; LATHAM, J. The effects of turbulent mixing in clouds. **Journal of the Atmospheric Sciences**, v. 41, n. 2, p. 299–304, 1984. 9

BAKER, M. B.; CORBIN, R. G.; LATHAM, J. The influence of entrainment on the evolution of cloud droplet spectra: I. a model of inhomogeneous mixing. **Quarterly Journal of the Royal Meteorological Society**, v. 106, n. 449, p. 581–598, 1980. 10, 11

BAKER, M. B.; LATHAM, J. The evolution of droplet spectra and the rate of production of embryonic raindrops in small cumulus clouds. **Journal of the Atmospheric Sciences**, v. 36, n. 8, p. 1612–1615, 1979. 10

BAUMGARDNER, D.; BRENGUIER, J.; BUCHOLTZ, A.; COE, H.; DEMOTT, P.; GARRETT, T.; GAYET, J.; HERMANN, M.; HEYMSFIELD, A.; KOROLEV, A.; KRäMER, M.; PETZOLD, A.; STRAPP, W.; PILEWSKIE, P.; TAYLOR, J.; TWOHY, C.; WENDISCH, M.; BACHALO, W.; CHUANG, P. Airborne instruments to measure atmospheric aerosol particles, clouds and radiation: a cook's tour of mature and emerging technology. **Atmospheric Research**, v. 102, n. 1, p. 10 – 29, 2011. 76

BAUMGARDNER, D.; JONSSON, H.; DAWSON, W.; O'CONNOR, D.; NEWTON, R. The cloud, aerosol and precipitation spectrometer: a new instrument for cloud investigations. **Atmospheric Research**, v. 59-60, p. 251 – 264, 2001. 18

BERRY, E. X.; REINHARDT, R. L. An analysis of cloud drop growth by collection: Part I. double distributions. **Journal of the Atmospheric Sciences**, v. 31, n. 7, p. 1814–1824, 1974. 1

BLYTH, A. M. Entrainment in cumulus clouds. **Journal of Applied Meteorology**, v. 32, n. 4, p. 626–641, 1993. 10, 11

BOUCHER, O.; RANDALL, D.; ARTAXO, P.; BRETHERTON, C.; FEINGOLD, G.; FORSTER, P.; KERMINEN, V.-M.; KONDO, Y.; LIAO, H.; LOHMANN, U.; RASCH, P.; SATHEESH, S.; SHERWOOD, S.; STEVENS, B.; ZHANG, X. Clouds and aerosols. In: STOCKER, T.; QIN, D.; PLATTNER, G.-K.; TIGNOR, M.; ALLEN, S.; BOSCHUNG, J.; NAUELS, A.; XIA, Y.; V., B.; MIDGLEY, P. (Ed.). **Climate change 2013: the physical science basis. contribution of Working Group I to the Fifth Assessment Report of the Intergovernmental Panel on Climate Change**. Cambridge, United Kingdom and New York, NY, USA: Cambridge University Press, 2013. 3

BRAGA, R. C.; ROSENFELD, D.; WEIGEL, R.; JURKAT, T.; ANDREAE, M. O.; WENDISCH, M.; PÖSCHL, U.; VOIGT, C.; MAHNKE, C.; BORRMANN, S.; ALBRECHT, R. I.; MOLLEKER, S.; VILA, D. A.; MACHADO, L. A. T.; GRULICH, L. Further evidence for ccn aerosol concentrations determining the height of warm rain and ice initiation in convective clouds over the Amazon basin. **Atmospheric Chemistry and Physics**, v. 17, n. 23, p. 14433–14456, 2017. 2, 3

BRENGUIER, J.-L.; GRABOWSKI, W. W. Cumulus entrainment and cloud droplet spectra: a numerical model within a two-dimensional dynamical framework. **Journal of the Atmospheric Sciences**, v. 50, n. 1, p. 120–136, 1993. 10, 11

BURNET, F.; BRENGUIER, J.-L. Observational study of the entrainment-mixing process in warm convective clouds. **Journal of the Atmospheric Sciences**, v. 64, n. 6, p. 1995–2011, 2007. 10

CECCHINI, M. A.; MACHADO, L. A. T.; ANDREAE, M. O.; MARTIN, S. T.; ALBRECHT, R. I.; ARTAXO, P.; BARBOSA, H. M. J.; BORRMANN, S.; FÜTTERER, D.; JURKAT, T.; MAHNKE, C.; MINIKIN, A.; MOLLEKER, S.; PÖHLKER, M. L.; PÖSCHL, U.; ROSENFELD, D.; VOIGT, C.; WEINZIERL, B.; WENDISCH, M. Sensitivities of Amazonian clouds to aerosols and updraft speed. **Atmospheric Chemistry and Physics**, v. 17, n. 16, p. 10037–10050, 2017. 3, 19, 26, 35, 78

CECCHINI, M. A.; MACHADO, L. A. T.; COMSTOCK, J. M.; MEI, F.; WANG, J.; FAN, J.; TOMLINSON, J. M.; SCHMID, B.; ALBRECHT, R.; MARTIN, S. T.; ARTAXO, P. Impacts of the manaus pollution plume on the microphysical properties of Amazonian warm-phase clouds in the wet season. **Atmospheric Chemistry and Physics**, v. 16, n. 11, p. 7029–7041, 2016. 3

CECCHINI, M. A.; MACHADO, L. A. T.; WENDISCH, M.; COSTA, A.; KRÄMER, M.; ANDREAE, M. O.; AFCHINE, A.; ALBRECHT, R. I.; ARTAXO, P.; BORRMANN, S.; FÜTTERER, D.; KLIMACH, T.; MAHNKE, C.; MARTIN, S. T.; MINIKIN, A.; MOLLEKER, S.; PARDO, L. H.; PÖHLKER, C.; PÖHLKER, M. L.; PÖSCHL, U.; ROSENFELD, D.; WEINZIERL, B. Illustration of microphysical processes in Amazonian deep convective clouds in the gamma phase space: introduction and potential applications. **Atmospheric Chemistry and Physics**, v. 17, n. 23, p. 14727–14746, 2017. 44, 73, 74, 76, 77, 92, 107

CHANDRAKAR, K. K.; CANTRELL, W.; CHANG, K.; CIOCHETTO, D.; NIEDERMEIER, D.; OVCHINNIKOV, M.; SHAW, R. A.; YANG, F. Aerosol indirect effect from turbulence-induced broadening of cloud-droplet size distributions. **Proceedings of the National Academy of Sciences**, v. 113, n. 50, p. 14243–14248, 2016. 12

CHANDRAKAR, K. K.; CANTRELL, W.; SHAW, R. A. Influence of turbulent fluctuations on cloud droplet size dispersion and aerosol indirect effects. **Journal of the Atmospheric Sciences**, v. 75, n. 9, p. 3191–3209, 08 2018. 12

CHAUMAT, L.; BRENGUIER, J.-L. Droplet spectra broadening in cumulus clouds. Part II: microscale droplet concentration heterogeneities. **Journal of the Atmospheric Sciences**, v. 58, n. 6, p. 642–654, 2001. 10

CHEN, J.; LIU, Y.; ZHANG, M.; PENG, Y. New understanding and quantification of the regime dependence of aerosol-cloud interaction for studying aerosol indirect effects. **Geophysical Research Letters**, v. 43, n. 4, p. 1780–1787, 2016. 8, 12, 79, 80

CHEN, S.; YAU, M. K.; BARTELLO, P. Turbulence effects of collision efficiency and broadening of droplet size distribution in cumulus clouds. **Journal of the Atmospheric Sciences**, v. 75, n. 1, p. 203–217, 2018. 10

CHEN, S.; YAU, M.-K.; BARTELLO, P.; XUE, L. Bridging the condensation–collision size gap: A direct numerical simulation of continuous

droplet growth in turbulent clouds. **Atmospheric Chemistry and Physics**, v. 18, n. 10, p. 7251–7262, 2018. 10

CLARKE, A. D.; KAPUSTIN, V. N.; EISELE, F. L.; WEBER, R. J.; MCMURRY, P. H. Particle production near marine clouds: sulfuric acid and predictions from classical binary nucleation. **Geophysical Research Letters**, v. 26, n. 16, p. 2425–2428, 1999. 7

COOPER, W. A. Effects of variable droplet growth histories on droplet size distributions. Part I: theory. **Journal of the Atmospheric Sciences**, v. 46, n. 10, p. 1301–1311, 1989. 9, 67, 71, 110

COOPER, W. A.; LASHER-TRAPP, S. G.; BLYTH, A. M. The influence of entrainment and mixing on the initial formation of rain in a warm cumulus cloud. **Journal of the Atmospheric Sciences**, v. 70, n. 6, p. 1727–1743, 2013. 10, 11

CUBISON, M. J.; ERVENS, B.; FEINGOLD, G.; DOCHERTY, K. S.; ULBRICH, I. M.; SHIELDS, L.; PRATHER, K.; HERING, S.; JIMENEZ, J. L. The influence of chemical composition and mixing state of los angeles urban aerosol on ccn number and cloud properties. **Atmospheric Chemistry and Physics**, v. 8, n. 18, p. 5649–5667, 2008. 8

DÁVILA, J.; HUNT, J. C. R. Settling of small particles near vortices and in turbulence. **Journal of Fluid Mechanics**, v. 440, p. 117–145, 2001. 10

DAWE, J. T.; AUSTIN, P. H. Interpolation of LES cloud surfaces for use in direct calculations of entrainment and detrainment. **Monthly Weather Review**, v. 139, n. 2, p. 444–456, 2011. 46

DEVENISH, B. J.; BARTELLO, P.; BRENGUIER, J.-L.; COLLINS, L. R.; GRABOWSKI, W. W.; IJZERMANS, R. H. A.; MALINOWSKI, S. P.; REEKS, M. W.; VASSILICOS, J. C.; WANG, L.-P.; WARHAFT, Z. Droplet growth in warm turbulent clouds. **Quarterly Journal of the Royal Meteorological Society**, v. 138, n. 667, p. 1401–1429, 2012. 9

DODSON, D. S.; GRISWOLD, J. D. S. Droplet inhomogeneity in shallow cumuli: the effects of in-cloud location and aerosol number concentration. **Atmospheric Chemistry and Physics**, v. 19, n. 11, p. 7297–7317, 2019. 9

DUSEK, U.; FRANK, G. P.; HILDEBRANDT, L.; CURTIUS, J.; SCHNEIDER, J.; WALTER, S.; CHAND, D.; DREWNICK, F.; HINGS, S.; JUNG, D.; BORRMANN, S.; ANDREAE, M. O. Size matters more than chemistry for

cloud-nucleating ability of aerosol particles. **Science**, v. 312, n. 5778, p. 1375–1378, 2006. 8

DZIEKAN, P.; WARUSZEWSKI, M.; PAWLOWSKA, H. University of Warsaw Lagrangian cloud model (UWLCM) 1.0: a modern large-eddy simulation tool for warm cloud modeling with Lagrangian microphysics. **Geoscientific Model Development**, v. 12, n. 6, p. 2587–2606, 2019. 112

ENGSTRÖM, A.; EKMAN, A. M. L. Impact of meteorological factors on the correlation between aerosol optical depth and cloud fraction. **Geophysical Research Letters**, v. 37, n. 18, 2010. 7

ENUKASHVILY, I. M. A numerical method for integrating the kinetic equation of coalescence and breakup of cloud droplets. **Journal of the Atmospheric Sciences**, v. 37, n. 11, p. 2521–2534, 1980. 1

ERVENS, B.; CUBISON, M.; ANDREWS, E.; FEINGOLD, G.; OGREN, J. A.; JIMENEZ, J. L.; DECARLO, P.; NENES, A. Prediction of cloud condensation nucleus number concentration using measurements of aerosol size distributions and composition and light scattering enhancement due to humidity. **Journal of Geophysical Research: Atmospheres**, v. 112, n. D10, 2007. 8

ERVENS, B.; FEINGOLD, G.; KREIDENWEIS, S. M. Influence of water-soluble organic carbon on cloud drop number concentration. **Journal of Geophysical Research: Atmospheres**, v. 110, n. D18, 2005. 30

FAN, J.; ZHANG, R.; LI, G.; TAO, W.-K.; LI, X. Simulations of cumulus clouds using a spectral microphysics cloud-resolving model. **Journal of Geophysical Research: Atmospheres**, v. 112, n. D4, 2007. 2, 3

FEINGOLD, G. Modeling of the first indirect effect: analysis of measurement requirements. **Geophysical Research Letters**, v. 30, n. 19, 2003. 8, 23, 29, 34, 35, 38, 109

FEINGOLD, G.; TZIVION, S.; LEVIV, Z. Evolution of raindrop spectra. part i: solution to the stochastic collection/breakup equation using the method of moments. **Journal of the Atmospheric Sciences**, v. 45, n. 22, p. 3387–3399, 1988. 16, 20

FERRIER, B. S. A double-moment multiple-phase four-class bulk ice scheme. Part I: description. **Journal of the Atmospheric Sciences**, v. 51, n. 2, p. 249–280, 1994. 1

FISCH, G.; TOTA, J.; MACHADO, L. A. T.; DIAS, M. A. F. S.; LYRA, R. F. d. F.; NOBRE, C. A.; DOLMAN, A. J.; GASH, J. H. C. The convective boundary layer over pasture and forest in Amazonia. **Theoretical and Applied Climatology**, v. 78, p. 47–59, 2004. 74

FLOSSMANN, A. I.; WOBROCK, W. A review of our understanding of the aerosol–cloud interaction from the perspective of a bin resolved cloud scale modelling. **Atmospheric Research**, v. 97, n. 4, p. 478 – 497, 2010. 8

FRANKLIN, C. N.; VAILLANCOURT, P. A.; YAU, M. K.; BARTELLO, P. Collision rates of cloud droplets in turbulent flow. **Journal of the Atmospheric Sciences**, v. 62, n. 7, p. 2451–2466, 2005. 10

FREUD, E.; ROSENFELD, D. Linear relation between convective cloud drop number concentration and depth for rain initiation. **Journal of Geophysical Research: Atmospheres**, v. 117, n. D2, 2012. 80

FREUD, E.; ROSENFELD, D.; KULKARNI, J. R. Resolving both entrainment-mixing and number of activated CCN in deep convective clouds. **Atmospheric Chemistry and Physics**, v. 11, n. 24, p. 12887–12900, 2011. 31

GÁCITA, M. S.; LONGO, K. M.; FREIRE, J. L. M.; FREITAS, S. R.; MARTIN, S. T. Impact of mixing state and hygroscopicity on ccn activity of biomass burning aerosol in Amazonia. **Atmospheric Chemistry and Physics**, v. 17, n. 3, p. 2373–2392, 2017. 8

GILMORE, M. S.; STRAKA, J. M.; RASMUSSEN, E. N. Precipitation uncertainty due to variations in precipitation particle parameters within a simple microphysics scheme. **Monthly Weather Review**, v. 132, n. 11, p. 2610–2627, 2004. 1

GONÇALVES, W.; MACHADO, L.; KIRSTETTER, P.-E. Influence of biomass aerosol on precipitation over the central Amazon: an observational study. **Atmospheric Chemistry and Physics**, v. 15, n. 12, p. 6789–6800, 2015. 2, 3

GRABOWSKI, W. W. Toward cloud resolving modeling of large-scale tropical circulations: a simple cloud microphysics parameterization. **Journal of the Atmospheric Sciences**, v. 55, n. 21, p. 3283–3298, 11 1998. 12, 84, 85

_____. Extracting microphysical impacts in large-eddy simulations of shallow convection. **Journal of the Atmospheric Sciences**, v. 71, n. 12, p. 4493–4499, 2014. 51

_____. Untangling microphysical impacts on deep convection applying a novel modeling methodology. **Journal of the Atmospheric Sciences**, v. 72, n. 6, p. 2446–2464, 2015. 51

_____. Comparison of Eulerian bin and Lagrangian particle-based schemes in simulations of Pi Chamber dynamics and microphysics. **Journal of the Atmospheric Sciences**, v. 77, n. 3, p. 1151–1165, 2020. 112

GRABOWSKI, W. W.; ABADE, G. C. Broadening of cloud droplet spectra through eddy hopping: turbulent adiabatic parcel simulations. **Journal of the Atmospheric Sciences**, v. 74, n. 5, p. 1485–1493, 2017. 9, 67, 71, 80, 101, 110

GRABOWSKI, W. W.; DZIEKAN, P.; PAWLOWSKA, H. Lagrangian condensation microphysics with Twomey CCN activation. **Geoscientific Model Development**, v. 11, n. 1, p. 103–120, 2018. 1, 112

GRABOWSKI, W. W.; JARECKA, D. Modeling condensation in shallow nonprecipitating convection. **Journal of the Atmospheric Sciences**, v. 72, n. 12, p. 4661–4679, 11 2015. 89

GRABOWSKI, W. W.; MORRISON, H. Toward the mitigation of spurious cloud-edge supersaturation in cloud models. **Monthly Weather Review**, v. 136, n. 3, p. 1224–1234, 2008. 23, 55

_____. Untangling microphysical impacts on deep convection applying a novel modeling methodology. Part II: double-moment microphysics. **Journal of the Atmospheric Sciences**, v. 73, n. 9, p. 3749–3770, 2016. 51

_____. Modeling condensation in deep convection. **Journal of the Atmospheric Sciences**, v. 74, n. 7, p. 2247–2267, 06 2017. 89

GRABOWSKI, W. W.; MORRISON, H.; SHIMA, S.-I.; ABADE, G. C.; DZIEKAN, P.; PAWLOWSKA, H. Modeling of cloud microphysics: can we do better? **Bulletin of the American Meteorological Society**, v. 100, n. 4, p. 655–672, 2019. 112

GRABOWSKI, W. W.; VAILLANCOURT, P. Comments on “Preferential concentration of cloud droplets by turbulence: effects on the early evolution of cumulus cloud droplet spectra”. **Journal of the Atmospheric Sciences**, v. 56, n. 10, p. 1433–1436, 1999. 10

GRABOWSKI, W. W.; WANG, L.-P. Growth of cloud droplets in a turbulent environment. **Annual Review of Fluid Mechanics**, v. 45, n. 1, p. 293–324, 2013. 9

GUNTHE, S. S.; KING, S. M.; ROSE, D.; CHEN, Q.; ROLDIN, P.; FARMER, D. K.; JIMENEZ, J. L.; ARTAXO, P.; ANDREAE, M. O.; MARTIN, S. T.; PÖSCHL, U. Cloud condensation nuclei in pristine tropical rainforest air of Amazonia: size-resolved measurements and modeling of atmospheric aerosol composition and ccn activity. **Atmospheric Chemistry and Physics**, v. 9, n. 19, p. 7551–7575, 2009. 8, 22, 41, 88

HALL, W. D. A detailed microphysical model within a two-dimensional dynamic framework: model description and preliminary results. **Journal of the Atmospheric Sciences**, v. 37, n. 11, p. 2486–2507, 1980. 44, 70

HARTMAN, C. M.; HARRINGTON, J. Y. Radiative impacts on the growth of drops within simulated marine stratocumulus. Part I: maximum solar heating. **Journal of the Atmospheric Sciences**, v. 62, n. 7, p. 2323–2338, 2005. 9

_____. Radiative impacts on the growth of drops within simulated marine stratocumulus. Part II: solar zenith angle variations. **Journal of the Atmospheric Sciences**, v. 62, n. 7, p. 2339–2351, 2005. 9

HEIBLUM, R. H.; ALTARATZ, O.; KOREN, I.; FEINGOLD, G.; KOSTINSKI, A. B.; KHAIN, A. P.; OVCHINNIKOV, M.; FREDJ, E.; DAGAN, G.; PINTO, L.; YAISH, R.; CHEN, Q. Characterization of cumulus cloud fields using trajectories in the center of gravity versus water mass phase space: 2. aerosol effects on warm convective clouds. **Journal of Geophysical Research: Atmospheres**, v. 121, n. 11, p. 6356–6373, 2016. 2, 3

Hernández Pardo, L.; MACHADO, L. A. T.; CECCHINI, M. A.; GÁCITA, M. S. Quantifying the aerosol effect on droplet size distribution at cloud top. **Atmospheric Chemistry and Physics**, v. 19, n. 11, p. 7839–7857, 2019. 20

HERNÁNDEZ PARDO, L.; MORRISON, H.; MACHADO, L. A. T.; HARRINGTON, J. Y.; LEBO, Z. J. Drop size distribution broadening mechanisms in a bin microphysics Eulerian model. **Journal of the Atmospheric Sciences**, v. 77, n. 9, p. 3249–3273, 09 2020. 40, 93, 107

HEYMSFIELD, A. J.; BANSEMER, A.; HEYMSFIELD, G.; FIERRO, A. O. Microphysics of maritime tropical convective updrafts at temperatures from -20^o

to -60^o. **Journal of the Atmospheric Sciences**, v. 66, n. 12, p. 3530–3562, 2009. 70

HILL, A.; DOBBIE, S.; YIN, Y. The impact of aerosols on non-precipitating marine stratocumulus. i: model description and prediction of the indirect effect. **Quarterly Journal of the Royal Meteorological Society**, v. 134, n. 634, p. 1143–1154, 2008. 21, 31

HOFFMANN, F. The effect of spurious cloud edge supersaturations in Lagrangian cloud models: an analytical and numerical study. **Monthly Weather Review**, v. 144, n. 1, p. 107–118, 12 2016. ISSN 0027-0644. 55

HOFFMANN, F.; NOH, Y.; RAASCH, S. The route to raindrop formation in a shallow cumulus cloud simulated by a Lagrangian cloud model. **Journal of the Atmospheric Sciences**, v. 74, n. 7, p. 2125–2142, 2017. 11

HOFFMANN, F.; RAASCH, S.; NOH, Y. Entrainment of aerosols and their activation in a shallow cumulus cloud studied with a coupled LCM–LES approach. **Atmospheric Research**, v. 156, p. 43 – 57, 2015. 10, 11, 19

HOLDRIDGE, D.; KYROUAC, J.; KEELER, E. **Balloon-Borne Sounding System (SONDEWNPN)**. 2014. Available from: http://www.arm.gov/instruments/sonde. Access in: 05 Apr. 2019. 40

HUDSON, J. G. Variability of the relationship between particle size and cloud-nucleating ability. **Geophysical Research Letters**, v. 34, n. 8, 2007. 8

HUDSON, J. G.; DA, X. Volatility and size of cloud condensation nuclei. **Journal of Geophysical Research: Atmospheres**, v. 101, n. D2, p. 4435–4442, 1996. 17

IGEL, A. L.; HEEVER, S. C. van den. The role of the gamma function shape parameter in determining differences between condensation rates in bin and bulk microphysics schemes. **Atmospheric Chemistry and Physics**, v. 17, n. 7, p. 4599–4609, 2017. 11

IVANOVA, E. T. Method of parameterizing the condensation process of droplet growth in numerical models. **Izvestiya Academy of Sciences USSR Atmospheric and Oceanic Physics**, v. 13, p. 821–826, 1977. 17, 21

JARUGA, A.; PAWLOWSKA, H. libcloudph++ 2.0: aqueous-phase chemistry extension of the particle-based cloud microphysics scheme. **Geoscientific Model Development**, v. 11, n. 9, p. 3623–3645, 2018. 112

JENSEN, J. B.; AUSTIN, P. H.; BAKER, M. B.; BLYTH, A. M. Turbulent mixing, spectral evolution and dynamics in a warm cumulus cloud. **Journal of the Atmospheric Sciences**, v. 42, n. 2, p. 173–192, 1985. 2

JENSEN, J. B.; NUGENT, A. D. Condensational growth of drops formed on giant sea-salt aerosol particles. **Journal of the Atmospheric Sciences**, v. 74, n. 3, p. 679–697, 2017. 9

JEONG, M.-J.; LI, Z. Separating real and apparent effects of cloud, humidity, and dynamics on aerosol optical thickness near cloud edges. **Journal of Geophysical Research: Atmospheres**, v. 115, n. D7, 2010. 7

KALNAY, E. **Atmospheric modeling, data assimilation and predictability**. [S.l.]: Cambridge University Press, 2002. 1

KARYDIS, V. A.; CAPPS, S. L.; RUSSELL, A. G.; NENES, A. Adjoint sensitivity of global cloud droplet number to aerosol and dynamical parameters. **Atmospheric Chemistry and Physics**, v. 12, n. 19, p. 9041–9055, 2012. 8

KHAIN, A.; LYNN, B.; DUDHIA, J. Aerosol effects on intensity of landfalling hurricanes as seen from simulations with the wrf model with spectral bin microphysics. **Journal of the Atmospheric Sciences**, v. 67, n. 2, p. 365–384, 2010. 1

KHAIN, A.; OVTCHINNIKOV, M.; PINSKY, M.; POKROVSKY, A.; KRUGLIAK, H. Notes on the state-of-the-art numerical modeling of cloud microphysics. **Atmospheric Research**, v. 55, n. 3, p. 159 – 224, 2000. ISSN 0169-8095. 11, 57

KHAIN, A.; PINSKY, M. **Physical processes in clouds and cloud modeling**. [S.l.: s.n.], 2018. ISBN 9780521767439. 2

KHAIN, A.; POKROVSKY, A.; PINSKY, M.; SEIFERT, A.; PHILLIPS, V. Simulation of effects of atmospheric aerosols on deep turbulent convective clouds using a spectral microphysics mixed-phase cumulus cloud model. Part I: model description and possible applications. **Journal of the Atmospheric Sciences**, v. 61, n. 24, p. 2963–2982, 2004. 1

KHAIN, A.; PRABHA, T. V.; BENMOSHE, N.; PANDITHURAI, G.; OVCHINNIKOV, M. The mechanism of first raindrops formation in deep convective clouds. **Journal of Geophysical Research: Atmospheres**, v. 118, n. 16, p. 9123–9140, 2013. 11, 39, 70, 80, 81, 97

KHAIN, A.; ROSENFELD, D.; POKROVSKY, A. Aerosol impact on the dynamics and microphysics of deep convective clouds. **Quarterly Journal of the Royal Meteorological Society**, v. 131, n. 611, p. 2639–2663, 2005. 2, 3

KHAIN, A. P.; BEHENG, K. D.; HEYMSFIELD, A.; KOROLEV, A.; KRICHAK, S. O.; LEVIN, Z.; PINSKY, M.; PHILLIPS, V.; PRABHAKARAN, T.; TELLER, A.; HEEVER, S. C. van den; YANO, J.-I. Representation of microphysical processes in cloud-resolving models: spectral (bin) microphysics versus bulk parameterization. **Reviews of Geophysics**, v. 53, n. 2, p. 247–322, 2015. 2

KHAIN, A. P.; BENMOSHE, N.; POKROVSKY, A. Factors determining the impact of aerosols on surface precipitation from clouds: an attempt at classification. **Journal of the Atmospheric Sciences**, v. 65, n. 6, p. 1721–1748, 2008. 39

KHAIROUTDINOV, M.; KOGAN, Y. A new cloud physics parameterization in a large-eddy simulation model of marine stratocumulus. **Monthly Weather Review**, v. 128, n. 1, p. 229–243, 01 2000. 87

KHVOROSTYANOV, V. I.; CURRY, J. A. Toward the theory of stochastic condensation in clouds. Part II: analytical solutions of the gamma-distribution type. **Journal of the Atmospheric Sciences**, v. 56, n. 23, p. 3997–4013, 12 1999. 12, 106

_____. Analytical solutions to the stochastic kinetic equation for liquid and ice particle size spectra. Part I: small-size fraction. **Journal of the Atmospheric Sciences**, v. 65, n. 7, p. 2025–2043, 07 2008. ISSN 0022-4928. 12, 106

KOGAN, Y.; KHAIROUTDINOV, M.; LILLY, D.; KOGAN, Z.; LIU, Q. Modeling of stratocumulus cloud layers in a large eddy simulation model with explicit microphysics. **Journal of the atmospheric sciences**, v. 52, n. 16, p. 2923–2940, 1995. 21

KOGAN, Y. L. The simulation of a convective cloud in a 3-D model with explicit microphysics. Part I: model description and sensitivity experiments. **Journal of the Atmospheric Sciences**, v. 48, n. 9, p. 1160–1189, 05 1991. 21, 88

KOREN, I.; FEINGOLD, G.; REMER, L. A. The invigoration of deep convective clouds over the atlantic: aerosol effect, meteorology or retrieval artifact? **Atmospheric Chemistry and Physics**, v. 10, n. 18, p. 8855–8872, 2010. 2, 3

KOROLEV, A. V. The influence of supersaturation fluctuations on droplet size spectra formation. **Journal of the Atmospheric Sciences**, v. 52, n. 20, p. 3620–3634, 1995. 9

KOSTINSKI, A. B.; SHAW, R. A. Scale-dependent droplet clustering in turbulent clouds. **Journal of Fluid Mechanics**, v. 434, p. 389–398, 2001. 10

LANCE, S.; BROCK, C. A.; ROGERS, D.; GORDON, J. A. Water droplet calibration of the Cloud Droplet Probe (CDP) and in-flight performance in liquid, ice and mixed-phase clouds during ARCPAC. **Atmospheric Measurement Techniques**, v. 3, n. 6, p. 1683–1706, 2010. 18

LASHER-TRAPP, S. G.; COOPER, W. A.; BLYTH, A. M. Broadening of droplet size distributions from entrainment and mixing in a cumulus cloud. **Quarterly Journal of the Royal Meteorological Society**, v. 131, n. 605, p. 195–220, 2005. 9, 10, 11

LATHAM, J.; REED, R. L. Laboratory studies of the effects of mixing on the evolution of cloud droplet spectra. **Quarterly Journal of the Royal Meteorological Society**, v. 103, n. 436, p. 297–306, 1977. 10

LEBO, Z. J.; JOHNSON, N. C.; HARRINGTON, J. Y. Radiative influences on ice crystal and droplet growth within mixed-phase stratus clouds. **Journal of Geophysical Research: Atmospheres**, v. 113, n. D9, 2008. 9

LEBO, Z. J.; MORRISON, H.; SEINFELD, J. H. Are simulated aerosol-induced effects on deep convective clouds strongly dependent on saturation adjustment? **Atmospheric Chemistry and Physics**, v. 12, n. 20, p. 9941–9964, 2012. 57, 60

LEBO, Z. J.; SEINFELD, J. H. A continuous spectral aerosol-droplet microphysics model. **Atmospheric Chemistry and Physics**, v. 11, n. 23, p. 12297–12316, 2011. Available from: <https://www.atmos-chem-phys.net/11/12297/2011/>. 21

LEE, S. S.; DONNER, L. J.; PHILLIPS, V. T.; MING, Y. Examination of aerosol effects on precipitation in deep convective clouds during the 1997 ARM summer experiment. **Quarterly Journal of the Royal Meteorological Society**, v. 134, n. 634, p. 1201–1220, 2008. 2, 3

LEROY, D.; WOBROCK, W.; FLOSSMANN, A. I. On the influence of the treatment of aerosol particles in different bin microphysical models: a comparison

between two different schemes. **Atmospheric Research**, v. 85, n. 3, p. 269 – 287, 2007. 31

LEVINE, J. Spherical vortex theory of bubble-like motion in cumulus clouds. **Journal of Meteorology**, v. 16, n. 6, p. 653–662, 1959. 44

LI, Z.; NIU, F.; FAN, J.; LIU, Y.; ROSENFELD, D.; DING, Y. Long-term impacts of aerosols on the vertical development of clouds and precipitation. **Nature Geoscience**, v. 4, n. 12, p. 888–894, 2011. 2, 3

LIM, K.-S. S.; HONG, S.-Y. Development of an effective double-moment cloud microphysics scheme with prognostic cloud condensation nuclei (CCN) for weather and climate models. **Monthly Weather Review**, v. 138, n. 5, p. 1587–1612, 2010. 1

LIN, Y.-L.; FARLEY, R. D.; ORVILLE, H. D. Bulk parameterization of the snow field in a cloud model. **Journal of Climate and Applied Meteorology**, v. 22, n. 6, p. 1065–1092, 1983. 1

LIU, Y.; DAUM, P. H. Indirect warming effect from dispersion forcing. **Nature**, v. 419, p. 580–581, 2002. 12

LIU, Y.; DAUM, P. H.; GUO, H.; PENG, Y. Dispersion bias, dispersion effect, and the aerosol–cloud conundrum. **Environmental Research Letters**, v. 3, n. 4, p. 045021, oct 2008. 12

LIU, Y.; DAUM, P. H.; YUM, S. S. Analytical expression for the relative dispersion of the cloud droplet size distribution. **Geophysical Research Letters**, v. 33, n. 2, 2006. 12

LOFTUS, A.; COTTON, W.; CARRIÓ, G. A triple-moment hail bulk microphysics scheme. Part I: description and initial evaluation. **Atmospheric research**, v. 149, p. 35–57, 2014. 1

LU, J.; NORDSIEK, H.; SHAW, R. A. Clustering of settling charged particles in turbulence: theory and experiments. **New Journal of Physics**, v. 12, n. 12, p. 123030, dec 2010. 10

LU, M.-L.; CONANT, W. C.; JONSSON, H. H.; VARUTBANGKUL, V.; FLAGAN, R. C.; SEINFELD, J. H. The Marine Stratus/Stratocumulus Experiment (MASE): aerosol-cloud relationships in marine stratocumulus. **Journal of Geophysical Research: Atmospheres**, v. 112, n. D10, 2007. 12

MACHADO, L. A. T.; DIAS, M. A. F. S.; MORALES, C.; FISCH, G.; VILA, D.; ALBRECHT, R.; GOODMAN, S. J.; CALHEIROS, A. J. P.; BISCARO, T.; KUMMEROW, C.; COHEN, J.; FITZJARRALD, D.; NASCIMENTO, E. L.; SAKAMOTO, M. S.; CUNNINGHAM, C.; CHABOUREAU, J.-P.; PETERSEN, W. A.; ADAMS, D. K.; BALDINI, L.; ANGELIS, C. F.; SAPUCCI, L. F.; SALIO, P.; BARBOSA, H. M. J.; LANDULFO, E.; SOUZA, R. A. F.; BLAKESLEE, R. J.; BAILEY, J.; FREITAS, S.; LIMA, W. F. A.; TOKAY, A. The CHUVA project: how does convection vary across Brazil? **Bulletin of the American Meteorological Society**, v. 95, n. 9, p. 1365–1380, 2014. 17, 40, 73

MANSELL, E. R.; ZIEGLER, C. L.; BRUNING, E. C. Simulated electrification of a small thunderstorm with two-moment bulk microphysics. **Journal of the Atmospheric Sciences**, v. 67, n. 1, p. 171–194, 2010. 1

MARTIN, G.; JOHNSON, D.; SPICE, A. The measurement and parameterization of effective radius of droplets in warm stratocumulus clouds. **Journal of the Atmospheric Sciences**, v. 51, n. 13, p. 1823–1842, 1994. 12, 87, 103

MARTIN, S. T.; ANDREAE, M. O.; ARTAXO, P.; BAUMGARDNER, D.; CHEN, Q.; GOLDSTEIN, A. H.; GUENTHER, A.; HEALD, C. L.; MAYOL-BRACERO, O. L.; MCMURRY, P. H.; PAULIQUEVIS, T.; PöSCHL, U.; PRATHER, K. A.; ROBERTS, G. C.; SALESKA, S. R.; DIAS, M. A. S.; SPRACKLEN, D. V.; SWIETLICKI, E.; TREBS, I. Sources and properties of Amazonian aerosol particles. **Reviews of Geophysics**, v. 48, n. 2, 2010. 22, 41, 88

MARTIN, S. T.; ARTAXO, P.; MACHADO, L. A. T.; MANZI, A. O.; SOUZA, R. A. F.; SCHUMACHER, C.; WANG, J.; ANDREAE, M. O.; BARBOSA, H. M. J.; FAN, J.; FISCH, G.; GOLDSTEIN, A. H.; GUENTHER, A.; JIMENEZ, J. L.; PÖSCHL, U.; SILVA DIAS, M. A.; SMITH, J. N.; WENDISCH, M. Introduction: observations and modeling of the Green Ocean Amazon (GoAmazon2014/5). **Atmospheric Chemistry and Physics**, v. 16, n. 8, p. 4785–4797, 2016. 40

MARTINS, J. V.; TANRé, D.; REMER, L.; KAUFMAN, Y.; MATTOO, S.; LEVY, R. Modis cloud screening for remote sensing of aerosols over oceans using spatial variability. **Geophysical Research Letters**, v. 29, n. 12, p. MOD4–1–MOD4–4, 2002. 7

MATSUI, T.; MASUNAGA, H.; KREIDENWEIS, S. M.; SR., R. A. P.; TAO, W.-K.; CHIN, M.; KAUFMAN, Y. J. Satellite-based assessment of marine low cloud variability associated with aerosol, atmospheric stability, and the diurnal

cycle. **Journal of Geophysical Research: Atmospheres**, v. 111, n. D17, 2006. 7

MAUGER, G. S.; NORRIS, J. R. Meteorological bias in satellite estimates of aerosol-cloud relationships. **Geophysical Research Letters**, v. 34, n. 16, 2007. 7

MCFIGGANS, G.; ARTAXO, P.; BALTENSPERGER, U.; COE, H.; FACCHINI, M. C.; FEINGOLD, G.; FUZZI, S.; GYSEL, M.; LAAKSONEN, A.; LOHMANN, U.; MENTEL, T. F.; MURPHY, D. M.; O'DOWD, C. D.; SNIDER, J. R.; WEINGARTNER, E. The effect of physical and chemical aerosol properties on warm cloud droplet activation. **Atmospheric Chemistry and Physics**, v. 6, n. 9, p. 2593–2649, 2006. Available from: <https://acp.copernicus.org/articles/6/2593/2006/>. 8

MECHEM, D. B.; KOGAN, Y. L. A bulk parameterization of giant CCN. **Journal of the Atmospheric Sciences**, v. 65, n. 7, p. 2458–2466, 2008. 31

MILES, N. L.; VERLINDE, J.; CLOTHIAUX, E. E. Cloud droplet size distributions in low-level stratiform clouds. **Journal of the atmospheric sciences**, v. 57, n. 2, p. 295–311, 2000. 11

MOLLEKER, S.; BORRMANN, S.; SCHLAGER, H.; LUO, B.; FREY, W.; KLINGEBIEL, M.; WEIGEL, R.; EBERT, M.; MITEV, V.; MATTHEY, R.; WOIWODE, W.; OELHAF, H.; DÖRNBRACK, A.; STRATMANN, G.; GROOSS, J.-U.; GÜNTHER, G.; VOGEL, B.; MÜLLER, R.; KRÄMER, M.; MEYER, J.; CAIRO, F. Microphysical properties of synoptic-scale polar stratospheric clouds: in situ measurements of unexpectedly large hno_3-containing particles in the arctic vortex. **Atmospheric Chemistry and Physics**, v. 14, n. 19, p. 10785–10801, 2014. 18

MORRISON, H. Impacts of updraft size and dimensionality on the perturbation pressure and vertical velocity in cumulus convection. Part I: simple, generalized analytic solutions. **Journal of the Atmospheric Sciences**, v. 73, n. 4, p. 1441–1454, 2016. 47

_____. Impacts of updraft size and dimensionality on the perturbation pressure and vertical velocity in cumulus convection. Part II: comparison of theoretical and numerical solutions and fully dynamical simulations. **Journal of the Atmospheric Sciences**, v. 73, n. 4, p. 1455–1480, 2016. 47

MORRISON, H.; CURRY, J. A.; KHVOROSTYANOV, V. I. A new double-moment microphysics parameterization for application in cloud and climate

models. Part I: description. **Journal of the Atmospheric Sciences**, v. 62, n. 6, p. 1665–1677, 06 2005. 17

MORRISON, H.; GRABOWSKI, W. W. Comparison of bulk and bin warm-rain microphysics models using a kinematic framework. **Journal of the Atmospheric Sciences**, v. 64, n. 8, p. 2839–2861, 2007. 11, 12

_____. Modeling supersaturation and subgrid-scale mixing with two-moment bulk warm microphysics. **Journal of the Atmospheric Sciences**, v. 65, n. 3, p. 792–812, 2008. 42

MORRISON, H.; THOMPSON, G.; TATARSKII, V. Impact of cloud microphysics on the development of trailing stratiform precipitation in a simulated squall line: comparison of one- and two-moment schemes. **Monthly Weather Review**, v. 137, n. 3, p. 991–1007, 2009. xxi, 1, 16, 84, 85

MORRISON, H.; WITTE, M.; BRYAN, G. H.; HARRINGTON, J. Y.; LEBO, Z. J. Broadening of modeled cloud droplet spectra using bin microphysics in an Eulerian spatial domain. **Journal of the Atmospheric Sciences**, v. 75, n. 11, p. 4005–4030, 2018. 2, 4, 39, 69, 72, 107, 110, 111

OVTCHINNIKOV, M.; EASTER, R. C. Nonlinear advection algorithms applied to interrelated tracers: errors and implications for modeling aerosol–cloud interactions. **Monthly Weather Review**, v. 137, n. 2, p. 632–644, 2009. 44, 96

PAINEMAL, D.; ZUIDEMA, P. Microphysical variability in southeast Pacific stratocumulus clouds: synoptic conditions and radiative response. **Atmospheric Chemistry and Physics**, v. 10, n. 13, p. 6255–6269, 2010. 7

PAWLOWSKA, H.; GRABOWSKI, W. W.; BRENGUIER, J.-L. Observations of the width of cloud droplet spectra in stratocumulus. **Geophysical Research Letters**, v. 33, n. 19, 2006. 12

PENG, Y.; LOHMANN, U. Sensitivity study of the spectral dispersion of the cloud droplet size distribution on the indirect aerosol effect. **Geophysical Research Letters**, v. 30, n. 10, 2003. 12

PENNER, J. E.; QUAAS, J.; STORELVMO, T.; TAKEMURA, T.; BOUCHER, O.; GUO, H.; KIRKEVÅG, A.; KRISTJÁNSSON, J. E.; SELAND, Ø. Model intercomparison of indirect aerosol effects. **Atmospheric Chemistry and Physics**, v. 6, n. 11, p. 3391–3405, 2006. 9

PETERS, J. M.; HANNAH, W.; MORRISON, H. The influence of vertical wind shear on moist thermals. **Journal of the Atmospheric Sciences**, v. 76, n. 6, p. 1645–1659, 2019. 16

PETTERS, M. D.; KREIDENWEIS, S. M. A single parameter representation of hygroscopic growth and cloud condensation nucleus activity. **Atmospheric Chemistry and Physics**, v. 7, n. 8, p. 1961–1971, 2007. 17

PETTERS, M. D.; SNIDER, J. R.; STEVENS, B.; VALI, G.; FALOONA, I.; RUSSELL, L. M. Accumulation mode aerosol, pockets of open cells, and particle nucleation in the remote subtropical Pacific marine boundary layer. **Journal of Geophysical Research: Atmospheres**, v. 111, n. D2, 2006. 7

PHILLIPS, V. T. J.; DONNER, L. J. Cloud microphysics, radiation and vertical velocities in two- and three-dimensional simulations of deep convection. **Quarterly Journal of the Royal Meteorological Society**, v. 132, n. 621C, p. 3011–3033, 2006. 47

PINSKY, M.; KHAIN, A. Theoretical analysis of mixing in liquid clouds – Part IV: DSD evolution and mixing diagrams. **Atmospheric Chemistry and Physics**, v. 18, n. 5, p. 3659–3676, 2018. 31

PINSKY, M.; KHAIN, A.; KOROLEV, A. Theoretical analysis of mixing in liquid clouds – Part 3: inhomogeneous mixing. **Atmospheric Chemistry and Physics**, v. 16, n. 14, p. 9273–9297, 2016. Available from: <https://www.atmos-chem-phys.net/16/9273/2016/>. 10, 31

PINSKY, M. B.; KHAIN, A. P. Effects of in-cloud nucleation and turbulence on droplet spectrum formation in cumulus clouds. **Quarterly Journal of the Royal Meteorological Society**, v. 128, n. 580, p. 501–533, 2002. 11, 70

PINSKY, M. B.; KHAIN, A. P.; GRITS, B.; SHAPIRO, M. Collisions of small drops in a turbulent flow. Part III: relative droplet fluxes and swept volumes. **Journal of the Atmospheric Sciences**, v. 63, n. 8, p. 2123–2139, 2006. 10

PINSKY, M. B.; KHAIN, A. P.; SHAPIRO, M. Collisions of cloud droplets in a turbulent flow. Part IV: droplet hydrodynamic interaction. **Journal of the Atmospheric Sciences**, v. 64, n. 7, p. 2462–2482, 2007. 10

PÖHLKER, M. L.; DITAS, F.; SATURNO, J.; KLIMACH, T.; ANGELIS, I. Hrabě de; ARAÙJO, A. C.; BRITO, J.; CARBONE, S.; CHENG, Y.; CHI, X.; DITZ, R.; GUNTHE, S. S.; HOLANDA, B. A.; KANDLER, K.; KESSELMEIER,

J.; KÖNEMANN, T.; KRÜGER, O. O.; LAVRIč, J. V.; MARTIN, S. T.; MIKHAILOV, E.; MORAN-ZULOAGA, D.; RIZZO, L. V.; ROSE, D.; SU, H.; THALMAN, R.; WALTER, D.; WANG, J.; WOLFF, S.; BARBOSA, H. M. J.; ARTAXO, P.; ANDREAE, M. O.; PÖSCHL, U.; PÖHLKER, C. Long-term observations of cloud condensation nuclei over the Amazon rain forest – Part 2: variability and characteristics of biomass burning, long-range transport, and pristine rain forest aerosols. **Atmospheric Chemistry and Physics**, v. 18, n. 14, p. 10289–10331, 2018. 3, 24, 99

PÖHLKER, M. L.; PÖHLKER, C.; DITAS, F.; KLIMACH, T.; ANGELIS, I. Hrabě de; ARAÚJO, A.; BRITO, J.; CARBONE, S.; CHENG, Y.; CHI, X.; DITZ, R.; GUNTHE, S. S.; KESSELMEIER, J.; KÖNEMANN, T.; LAVRIč, J. V.; MARTIN, S. T.; MIKHAILOV, E.; MORAN-ZULOAGA, D.; ROSE, D.; SATURNO, J.; SU, H.; THALMAN, R.; WALTER, D.; WANG, J.; WOLFF, S.; BARBOSA, H. M. J.; ARTAXO, P.; ANDREAE, M. O.; PÖSCHL, U. Long-term observations of cloud condensation nuclei in the Amazon rain forest – Part 1: aerosol size distribution, hygroscopicity, and new model parametrizations for CCN prediction. **Atmospheric Chemistry and Physics**, v. 16, n. 24, p. 15709–15740, 2016. 3, 22, 24, 41, 88, 99

PORCù, F.; D'ADDERIO, L. P.; PRODI, F.; CARACCIOLO, C. Effects of altitude on maximum raindrop size and fall velocity as limited by collisional breakup. **Journal of the Atmospheric Sciences**, v. 70, n. 4, p. 1129–1134, 04 2013. 83

PRUPPACHER, H. R.; KLETT, J. D. **Microphysics of clouds and precipitation: reprinted 1980**. [S.l.]: Springer Science & Business Media, 2012. 2, 9, 15, 17

QUINN, P. K.; BATES, T. S.; COFFMAN, D. J.; COVERT, D. S. Influence of particle size and chemistry on the cloud nucleating properties of aerosols. **Atmospheric Chemistry and Physics**, v. 8, n. 4, p. 1029–1042, 2008. 8

REID, J. S.; HOBBS, P. V.; RANGNO, A. L.; HEGG, D. A. Relationships between cloud droplet effective radius, liquid water content, and droplet concentration for warm clouds in Brazil embedded in biomass smoke. **Journal of Geophysical Research: Atmospheres**, v. 104, n. D6, p. 6145–6153, 1999. 3

REISIN, T. G.; YIN, Y.; LEVIN, Z.; TZIVION, S. Development of giant drops and high-reflectivity cores in Hawaiian clouds: numerical simulations using a

kinematic model with detailed microphysics. **Atmospheric Research**, v. 45, n. 4, p. 275 – 297, 1998. ISSN 0169-8095. 16

REUTTER, P.; SU, H.; TRENTMANN, J.; SIMMEL, M.; ROSE, D.; GUNTHE, S. S.; WERNLI, H.; ANDREAE, M. O.; PÖSCHL, U. Aerosol- and updraft-limited regimes of cloud droplet formation: influence of particle number, size and hygroscopicity on the activation of cloud condensation nuclei (CCN). **Atmospheric Chemistry and Physics**, v. 9, n. 18, p. 7067–7080, 2009. 8, 23, 26, 29, 30, 35, 37, 38, 79, 109

RIECHELMANN, T.; NOH, Y.; RAASCH, S. A new method for large-eddy simulations of clouds with Lagrangian droplets including the effects of turbulent collision. **New Journal of Physics**, v. 14, n. 6, p. 065008, jun 2012. 112

RISSMAN, T. A.; NENES, A.; SEINFELD, J. H. Chemical amplification (or dampening) of the Twomey effect: conditions derived from droplet activation theory. **Journal of the Atmospheric Sciences**, v. 61, n. 8, p. 919–930, 2004. 34

ROESLER, E. L.; PENNER, J. E. Can global models ignore the chemical composition of aerosols? **Geophysical Research Letters**, v. 37, n. 24, 2010. 8

ROMPS, D. M. A direct measure of entrainment. **Journal of the Atmospheric Sciences**, v. 67, n. 6, p. 1908–1927, 2010. 45, 46

ROSE, D.; NOWAK, A.; ACHTERT, P.; WIEDENSOHLER, A.; HU, M.; SHAO, M.; ZHANG, Y.; ANDREAE, M. O.; PÖSCHL, U. Cloud condensation nuclei in polluted air and biomass burning smoke near the mega-city Guangzhou, China – Part 1: size-resolved measurements and implications for the modeling of aerosol particle hygroscopicity and CCN activity. **Atmospheric Chemistry and Physics**, v. 10, n. 7, p. 3365–3383, 2010. 8

ROSENFELD, D.; LOHMANN, U.; RAGA, G. B.; O'DOWD, C. D.; KULMALA, M.; FUZZI, S.; REISSELL, A.; ANDREAE, M. O. Flood or drought: how do aerosols affect precipitation? **Science**, v. 321, n. 5894, p. 1309–1313, 2008. 2, 3

ROTACH, M. W.; ZARDI, D. On the boundary-layer structure over highly complex terrain: key findings from MAP. **Quarterly Journal of the Royal Meteorological Society**, v. 133, n. 625, p. 937–948, 2007. 16

ROTSTAYN, L. D.; LIU, Y. Sensitivity of the first indirect aerosol effect to an increase of cloud droplet spectral dispersion with droplet number concentration. **Journal of Climate**, v. 16, n. 21, p. 3476–3481, 11 2003. 12, 84, 85

SEGAL, Y.; PINSKY, M.; KHAIN, A.; ERLICK, C. Thermodynamic factors influencing bimodal spectrum formation in cumulus clouds. **Atmospheric Research**, v. 66, n. 1, p. 43 – 64, 2003. ISSN 0169-8095. 70

SEIFERT, A.; BEHENG, K. D. A two-moment cloud microphysics parameterization for mixed-phase clouds. Part 1: model description. **Meteorology and Atmospheric Physics**, v. 92, p. 45–66, 2006. 87, 104

SEIFERT, A.; LEINONEN, J.; SIEWERT, C.; KNEIFEL, S. The geometry of rimed aggregate snowflakes: a modeling study. **Journal of Advances in Modeling Earth Systems**, v. 11, n. 3, p. 712–731, 2019. 1, 112

SEINFELD, J. H.; BRETHERTON, C.; CARSLAW, K. S.; COE, H.; DEMOTT, P. J.; DUNLEA, E. J.; FEINGOLD, G.; GHAN, S.; GUENTHER, A. B.; KAHN, R.; KRAUCUNAS, I.; KREIDENWEIS, S. M.; MOLINA, M. J.; NENES, A.; PENNER, J. E.; PRATHER, K. A.; RAMANATHAN, V.; RAMASWAMY, V.; RASCH, P. J.; RAVISHANKARA, A. R.; ROSENFELD, D.; STEPHENS, G.; WOOD, R. Improving our fundamental understanding of the role of aerosol-cloud interactions in the climate system. **Proceedings of the National Academy of Sciences**, v. 113, n. 21, p. 5781–5790, 2016. 3

SHAW, R. A.; READE, W. C.; COLLINS, L. R.; VERLINDE, J. Preferential concentration of cloud droplets by turbulence: effects on the early evolution of cumulus cloud droplet spectra. **Journal of the Atmospheric Sciences**, v. 55, n. 11, p. 1965–1976, 1998. 10

SHIMA, S.; KUSANO, K.; KAWANO, A.; SUGIYAMA, T.; KAWAHARA, S. The super-droplet method for the numerical simulation of clouds and precipitation: a particle-based and probabilistic microphysics model coupled with a non-hydrostatic model. **Quarterly Journal of the Royal Meteorological Society**, v. 135, n. 642, p. 1307–1320, 2009. 1, 112

SHIPWAY, B. J.; HILL, A. A. Diagnosis of systematic differences between multiple parametrizations of warm rain microphysics using a kinematic framework. **Quarterly Journal of the Royal Meteorological Society**, v. 138, n. 669, p. 2196–2211, 2012. 15

SKAMAROCK, W. C.; KLEMP, J. B.; DUDHIA, J.; GILL, D. O.; BARKER, D. M.; DUDA, M. G.; HUANG, X.-Y.; WANG, W.; POWERS, J. G. **A description of the Advanced Research WRF version 3 (No. NCAR/TN-475+STR)**. [S.l.], 2008. 16, 40, 87

SLAWINSKA, J.; GRABOWSKI, W. W.; PAWLOWSKA, H.; MORRISON, H. Droplet activation and mixing in large-eddy simulation of a shallow cumulus field. **Journal of the Atmospheric Sciences**, v. 69, n. 2, p. 444–462, 02 2012. 19

STEVENS, B.; FEINGOLD, G. Untangling aerosol effects on clouds and precipitation in a buffered system. **Nature**, v. 461, p. 607–613, 2009. 3, 7, 8

STEVENS, B.; FEINGOLD, G.; COTTON, W. R.; WALKO, R. L. Elements of the microphysical structure of numerically simulated nonprecipitating stratocumulus. **Journal of the Atmospheric Sciences**, v. 53, n. 7, p. 980–1006, 1996. 16, 17

STEVENS, B.; WALKO, R. L.; COTTON, W. R.; FEINGOLD, G. The spurious production of cloud-edge supersaturations by Eulerian models. **Monthly Weather Review**, v. 124, n. 5, p. 1034–1041, 1996. 23, 55

SöLCH, I.; KäRCHER, B. A large-eddy model for cirrus clouds with explicit aerosol and ice microphysics and Lagrangian ice particle tracking. **Quarterly Journal of the Royal Meteorological Society**, v. 136, n. 653, p. 2074–2093, 2010. 112

TANRé, D.; KAUFMAN, Y. J.; HERMAN, M.; MATTOO, S. Remote sensing of aerosol properties over oceans using the MODIS/EOS spectral radiances. **Journal of Geophysical Research: Atmospheres**, v. 102, n. D14, p. 16971–16988, 1997. 7

TAO, W.-k.; SIMPSON, J.; SOONG, S.-T. Statistical properties of a cloud ensemble: a numerical study. **Journal of the Atmospheric Sciences**, v. 44, n. 21, p. 3175–3187, 1987. 47

THOMPSON, G.; EIDHAMMER, T. A study of aerosol impacts on clouds and precipitation development in a large winter cyclone. **Journal of the Atmospheric Sciences**, v. 71, n. 10, p. 3636–3658, 2014. 1

THOMPSON, G.; FIELD, P. R.; RASMUSSEN, R. M.; HALL, W. D. Explicit forecasts of winter precipitation using an improved bulk microphysics scheme. Part II: implementation of a new snow parameterization. **Monthly Weather Review**, v. 136, p. 5095–5115, 2008. 1, 12, 84, 85

TURNER, J. S. Model experiments relating to thermals with increasing buoyancy. **Quarterly Journal of the Royal Meteorological Society**, v. 89, n. 379, p. 62–74, 1963. 44

TWOMEY, S. Pollution and the planetary albedo. **Atmospheric Environment**, v. 8, n. 12, p. 1251 – 1256, 1974. 2, 3

TZIVION, S.; FEINGOLD, G.; LEVIN, Z. An efficient numerical solution to the stochastic collection equation. **Journal of the Atmospheric Sciences**, v. 44, n. 21, p. 3139–3149, 1987. 1, 16, 20

_____. The evolution of raindrop spectra. Part II: collisional collection/breakup and evaporation in a rainshaft. **Journal of the Atmospheric Sciences**, v. 46, n. 21, p. 3312–3328, 1989. 16, 17, 20

UNTERSTRASSER, S.; HOFFMANN, F.; LERCH, M. Collection/aggregation algorithms in Lagrangian cloud microphysical models: rigorous evaluation in box model simulations. **Geoscientific Model Development**, v. 10, n. 4, p. 1521–1548, 2017. 112

VAILLANCOURT, P. A.; YAU, M. K.; BARTELLO, P.; GRABOWSKI, W. W. Microscopic approach to cloud droplet growth by condensation. Part II: turbulence, clustering, and condensational growth. **Journal of the Atmospheric Sciences**, v. 59, n. 24, p. 3421–3435, 2002. 10

WANG, J.; KREJCI, R.; GIANGRANDE, S.; KUANG, C.; BARBOSA, H. M.; BRITO, J.; CARBONE, S.; CHI, X.; COMSTOCK, J.; DITAS, F.; LAVRIC, J.; MANNINEN, H. E.; MEI, F.; MORAN-ZULOAGA, D.; PöHLKER, C.; PöHLKER, M. L.; SATURNO, J.; SCHMID, B.; SOUZA, R. A. F.; SPRINGSTON, S. R.; TOMLINSON, J. M.; TOTO, T.; WALTER, D.; WIMMER, D.; SMITH, J. N.; KULMALA, M.; MACHADO, L. A. T.; ARTAXO, P.; ANDREAE, M. O.; PETäJä, T.; MARTIN, S. T. Amazon boundary layer aerosol concentration sustained by vertical transport during rainfall. **Nature**, v. 539, p. 416–419, 2016. 3

WANG, L.-P.; AYALA, O.; ROSA, B.; GRABOWSKI, W. W. Turbulent collision efficiency of heavy particles relevant to cloud droplets. **New Journal of Physics**, v. 10, n. 7, p. 075013, jul 2008. 10

WANG, S.; SOBEL, A. H. Response of convection to relative sea surface temperature: cloud-resolving simulations in two and three dimensions. **Journal of Geophysical Research: Atmospheres**, v. 116, n. D11, 2011. 49

WARD, D. S.; EIDHAMMER, T.; COTTON, W. R.; KREIDENWEIS, S. M. The role of the particle size distribution in assessing aerosol composition effects on

simulated droplet activation. **Atmospheric Chemistry and Physics**, v. 10, n. 12, p. 5435–5447, 2010. 8, 20, 23, 26, 34, 35, 37, 38, 109

WEI, X.; CHANG, N.-B.; BAI, K.; GAO, W. Satellite remote sensing of aerosol optical depth: advances, challenges, and perspectives. **Critical Reviews in Environmental Science and Technology**, v. 50, n. 16, p. 1640–1725, 2020. 7

WENDISCH, M.; PÖSCHL, U.; ANDREAE, M. O.; MACHADO, L. A. T.; ALBRECHT, R.; SCHLAGER, H.; ROSENFELD, D.; MARTIN, S. T.; ABDELMONEM, A.; AFCHINE, A.; ARAùJO, A. C.; ARTAXO, P.; AUFMHOFF, H.; BARBOSA, H. M. J.; BORRMANN, S.; BRAGA, R.; BUCHHOLZ, B.; CECCHINI, M. A.; COSTA, A.; CURTIUS, J.; DOLLNER, M.; DORF, M.; DREILING, V.; EBERT, V.; EHRLICH, A.; EWALD, F.; FISCH, G.; FIX, A.; FRANK, F.; FüTTERER, D.; HECKL, C.; HEIDELBERG, F.; HüNEKE, T.; JäKEL, E.; JäRVINEN, E.; JURKAT, T.; KANTER, S.; KäSTNER, U.; KENNTNER, M.; KESSELMEIER, J.; KLIMACH, T.; KNECHT, M.; KOHL, R.; KöLLING, T.; KRäMER, M.; KRüGER, M.; KRISNA, T. C.; LAVRIC, J. V.; LONGO, K.; MAHNKE, C.; MANZI, A. O.; MAYER, B.; MERTES, S.; MINIKIN, A.; MOLLEKER, S.; MüNCH, S.; NILLIUS, B.; PFEILSTICKER, K.; PöHLKER, C.; ROIGER, A.; ROSE, D.; ROSENOW, D.; SAUER, D.; SCHNAITER, M.; SCHNEIDER, J.; SCHULZ, C.; SOUZA, R. A. F. de; SPANU, A.; STOCK, P.; VILA, D.; VOIGT, C.; WALSER, A.; WALTER, D.; WEIGEL, R.; WEINZIERL, B.; WERNER, F.; YAMASOE, M. A.; ZIEREIS, H.; ZINNER, T.; ZöGER, M. The ACRIDICON-CHUVA campaign: studying tropical deep convective clouds and precipitation over Amazonia using the new German research aircraft HALO. **Bulletin of the American Meteorological Society**, n. 2016, 2016. 17, 40, 73

WILHELMSON, R. The life cycle of a thunderstorm in three dimensions. **Journal of the Atmospheric Sciences**, v. 31, n. 6, p. 1629–1651, 1974. 47

WITTE, M. K.; CHUANG, P. Y.; AYALA, O.; WANG, L.-P.; FEINGOLD, G. Comparison of observed and simulated drop size distributions from large-eddy simulations with bin microphysics. **Monthly Weather Review**, v. 147, n. 2, p. 477–493, 2019. 39

YANG, F.; KOLLIAS, P.; SHAW, R. A.; VOGELMANN, A. M. Cloud droplet size distribution broadening during diffusional growth: ripening amplified by deactivation and reactivation. **Atmospheric Chemistry and Physics**, v. 18, n. 10, p. 7313–7328, 2018. 9

YANG, F.; SHAW, R.; XUE, H. Conditions for super-adiabatic droplet growth after entrainment mixing. **Atmospheric Chemistry and Physics**, v. 16, n. 14, p. 9421–9433, 2016. Available from: <https://www.atmos-chem-phys.net/16/9421/2016/>. 71

YANG, Q.; EASTER, R. C.; CAMPUZANO-JOST, P.; JIMENEZ, J. L.; FAST, J. D.; GHAN, S. J.; WANG, H.; BERG, L. K.; BARTH, M. C.; LIU, Y.; SHRIVASTAVA, M. B.; SINGH, B.; MORRISON, H.; FAN, J.; ZIEGLER, C. L.; BELA, M.; APEL, E.; DISKIN, G. S.; MIKOVINY, T.; WISTHALER, A. Aerosol transport and wet scavenging in deep convective clouds: a case study and model evaluation using a multiple passive tracer analysis approach. **Journal of Geophysical Research: Atmospheres**, v. 120, n. 16, p. 8448–8468, 2015. 70

YANG, Y.; GIROLAMO, L. D. Impacts of 3-D radiative effects on satellite cloud detection and their consequences on cloud fraction and aerosol optical depth retrievals. **Journal of Geophysical Research: Atmospheres**, v. 113, n. D4, 2008. 7

YEOM, J. M.; YUM, S. S.; MEI, F.; SCHMID, B.; COMSTOCK, J.; MACHADO, L. A.; CECCHINI, M. A. Impact of secondary droplet activation on the contrasting cloud microphysical relationships during the wet and dry seasons in the Amazon. **Atmospheric Research**, v. 230, p. 104648, 2019. 19

YIN, Y.; CARSLAW, K. S.; FEINGOLD, G. Vertical transport and processing of aerosols in a mixed-phase convective cloud and the feedback on cloud development. **Quarterly Journal of the Royal Meteorological Society**, v. 131, n. 605, p. 221–245, 2005. 31

YIN, Y.; LEVIN, Z.; REISIN, T.; TZIVION, S. Seeding convective clouds with hygroscopic flares: numerical simulations using a cloud model with detailed microphysics. **Journal of Applied Meteorology**, v. 39, n. 9, p. 1460–1472, 2000. 16, 31

YIN, Y.; LEVIN, Z.; REISIN, T. G.; TZIVION, S. The effects of giant cloud condensation nuclei on the development of precipitation in convective clouds — a numerical study. **Atmospheric Research**, v. 53, n. 1, p. 91 – 116, 2000. 9, 16, 31

ZENG, X.; TAO, W.-K.; LANG, S.; HOU, A. Y.; ZHANG, M.; SIMPSON, J. On the sensitivity of atmospheric ensembles to cloud microphysics in long-term cloud-resolving model simulations. **Journal of the Meteorological Society of Japan. Ser. II**, v. 86A, p. 45–65, 2008. 47